Direct Laser Writing of Metals and Composite Materials

zur Erlangung des akademischen Grades eines

Doktors der Naturwissenschaften

(Dr. rer. nat.)

von der KIT-Fakultät für Chemie und Biowissenschaften

des Karlsruher Instituts für Technologie (KIT)

genehmigte

Dissertation

von

MSc. Matthias Steurer

Dekan: Prof. Dr. Martin Bastmeyer

Referent: Prof. Dr. Claus Feldmann

Referent: Prof. Dr. Christopher Barner-Kowollik

Korreferent: T.T.-Prof. Dr. Schirin Hanf

Tag der mündlichen Prüfung: 02.02.2026

Direct Laser Writing of Metals and Composite Materials

Matthias Steurer

MSc(Chem)

Submitted in fulfilment of the requirements for the degree of

Doctor of Philosophy

School of Chemistry and Physics

Faculty of Science

Queensland University of Technology

Karlsruhe Institute of Technology

2026

STATEMENT OF ORIGINAL AUTHORSHIP

The presented thesis was developed between December 2022 and December 2025 in a binational PhD agreement (‘cotutelle de these’) between the Queensland University of Technology (QUT, Australia) and the Karlsruhe Institute of Technology (KIT, Germany) under the supervision of Prof. Dr. Christopher Barner-Kowollik (QUT) and Prof. Dr. Claus Feldmann (KIT). Furthermore, Prof. Dr. Martin Wegener (KIT) acted as mentor.

Die vorliegende Arbeit wurde im Zeitraum vom 01.12.2022 bis zum 17.12.2025 am Karlsruher Institut für Technologie (KIT) und an der School of Chemistry and Physics der Queensland University of Technology (QUT) unter der Anleitung von Prof. Dr. Claus Feldmann sowie Prof. Dr. Christopher Barner-Kowollik durchgeführt.

Hiermit versichere ich, dass die vorliegende Arbeit selbstständig verfasst wurde und nur angegebene Quellen und Hilfsmittel verwendet wurden und alle Zitate kenntlich gemacht sind. Zur sprachlichen Korrektur und Gewährleistung von Lesefluss wurde OpenAI GPT-5 genutzt. Ich habe die Satzung des Karlsruher Instituts für Technologie (KIT) zur Sicherung guter wissenschaftlicher Praxis in der jeweils gültigen Fassung beachtet. Des Weiteren erkläre ich, dass ich mich derzeit in keinem weiteren laufenden Promotionsverfahren befinde und auch keine vorausgegangenen Promotionsversuche unternommen habe.

Karlsruhe, den 17.12.2025

KEYWORDS

Photothermal Laser Printing • Semiconductor • Zinc Oxide, Single Crystallinity • 4D Printing • Inorganic-Organic Hybrid Nanoparticles • Photoresin • External Stimuli • Responsiveness • pH Sensor • Color Change • O_2 Sensor • Fluorescence

ABSTRACT

Three-dimensional (3D) printing is a versatile tool to turn digital designs into real-life objects and reduce fabrication costs and waste. The main challenge in light-driven 3D printing is to formulate suitable photoresins – light-sensitive inks – to fabricate a wide variety of 3D printed objects. Mostly, (meth)acrylate-based monomers and oligomers are used for fabrication, thus offering limited property profiles. Approaches to expand the property profile are to fuse organic photoresins with inorganic materials such as nanoparticles (NPs) or the laser-printing of fully inorganic materials. However, several challenges, such as NP aggregation and photodegradation, need to be overcome to fabricate these composite and inorganic materials.

In the present thesis advances are presented to overcome the challenges of fabricating composite and inorganic materials using different ink formulations and printing approaches. The first part of the current thesis explores the fabrication of dynamic composite materials, which change their chemical or physical properties upon exposure to different external stimuli such as pH, light, and small molecules. The responsiveness is enabled by using a simple photoresin formulation consisting of a bifunctional oligomer, photoinitiator and functional NPs. In addition, the influence of various parameters such as the NP concentration and material thickness on the composite-material sensitivity is explored. The second part of the thesis is devoted to photothermal laser printing of metal oxides and metals. This printing approach is used to fabricate single-crystalline sub-micrometer zinc oxide structures with various complex geometries without the need for post-processing.

KURZZUSAMMENFASSUNG

Der 3D Druck ist ein vielseitiges Werkzeug um digitale Designs in reale Objekte umzusetzen und gleichzeitig Herstellungskosten und Abfall zu reduzieren. Die größte Herausforderung beim lichtgesteuerten 3D-Druck besteht in der Entwicklung von Fotolacken zur Herstellung einer breiten Auswahl von 3D-gedruckten Objekten. Meist werden (Meth)acrylat-basierte Monomere und Oligomere als druckbare Matrix verwendet, die jedoch das Spektrum an zugänglichen Eigenschaften stark limitieren. Zur Erweiterung des Eigenschaftsvielfalt werden in der vorliegenden Arbeit die Herstellung von funktionellen Komposit- und anorganischen Materialien mithilfe verschiedener Tintenformulierungen und Druckverfahren untersucht. Der erste Teil befasst sich mit der Herstellung dynamischer Kompositmaterialien, deren chemische oder physikalische Eigenschaften sich unter dem Einfluss verschiedener externer Reize wie pH-Wert, Licht und kleiner Moleküle verändern. Diese reizinduzierte Veränderung wird durch eine einfache Fotolackformulierung ermöglicht, die aus einem bifunktionellen Oligomer, einem Fotoinitiator und funktionalisierten Nanopartikeln besteht. Darüber hinaus wird der Einfluss verschiedener Parameter wie der Nanopartikelkonzentration und der Materialdicke auf die Sensitivität des Kompositmaterials untersucht. Der zweite Teil der Arbeit widmet sich dem photothermischen Laserdruck von Metalloxiden und Metallen. Mit diesem Druckverfahren lassen sich einkristalline Zinkoxidstrukturen im Submikrometerbereich mit verschiedenen komplexen Geometrien ohne einen erforderlichen Nachbearbeitungschritt herstellen.

ACADEMIC OUTPUT

Publications in peer-reviewed journals:

- Photothermal Laser Printing of Sub-Micrometer Crystalline ZnO Structures

  Matthias Steurer,[#] Paul Somers,[#] Kristian Kraft,[#] Lukas Grünewald,[#] Steven Kraus, Florian Feist, Bastian Weinert, Erich Müller, Stefanie Dehnen, Claus Feldmann, Yolita M. Eggeler, Christopher Barner-Kowollik and Martin Wegener

  Adv. Sci. **2025**, 12, 2410771.

- Color and Fluorescence Switchable 2D and 3D Printed Hybrid Materials

  Matthias Steurer,[#] Xingyu Wu,[#] Agnes C. Morrissey, Konstantin Faershteyn, Magdalena Fladung, Paul Somers, Florian Feist, Martin Bastmeyer, Martin Wegener, Claus Feldmann and Christopher Barner-Kowollik

  Mater. Horiz. **2025**, *12*, 9139-9148.

- Electron Microscopic Analysis of Rotating Single Lattice ZnO Crystals Produced by Photothermal Laser Printing

  Lukas Grünewald, Kristian Kraft, **Matthias Steurer**, Paul Somers, Steven Kraus, Florian Feist, Bastian Weinert, Erich Müller, Stefanie Dehnen, Claus Feldmann, Christopher Barner-Kowollik, Martin Wegener, Yolita M. Eggeler

  Microsc. Microanal. **2024**, *30*, 1242-1243.

[#] Contributed Equally

Unpublished work:

- Printable Flavin-Based Composites for Oxygen Sensing

  Matthias Steurer, Kristian Kraft, Kai-Ching Fan, Anton Gotzes, Xingyu Wu, Paul Somers, Florian Feist, Martin Wegener, Christopher Barner-Kowollik and Claus Feldmann, *submitted*

Conference contributions:

- Laser Microprinting of Electronics and Hybrid Materials

  Matthias Steurer, Steven Kraus, Paul Somers, Florian Feist, Martin Wegener, Christopher Barner-Kowollik and Claus Feldmann

  Nanotage, Dresden, September 2023.
- Hybrid Nanoparticles for Smart Composites: From Synthesis to Material Functionality

  Matthias Steurer, Xingyu Wu, Paul Somers, Florian Feist, Martin Wegener, Christopher Barner-Kowollik and Claus Feldmann

  Nanotage, Aachen, October 2025.
- Color and Fluorescence Switchable 2D and 3D Printed Hybrid Materials

  Matthias Steurer, Xingyu Wu, Agnes C. Morrissey, Konstantin Faershteyn, Magdalena Fladung, Paul Somers, Florian Feist, Martin Bastmeyer, Martin Wegener, Claus Feldmann and Christopher Barner-Kowollik

  17th International Conference on Materials Chemistry (MC17), Edinburgh, July 2025.

ACKNOWLEDGEMENT

I would like to thank my principal supervisors, Christopher and Claus, for their guidance, support, advice, and inspiring discussions over the past three years. I am sincerely thankful to them for providing me the opportunity to go overseas and conduct my research in Australia. I deeply appreciate the constant suggestions for exploring further interesting research topics. I am very grateful that I was able to conduct my PhD in both groups.

Furthermore, I am grateful to QUT and KIT making it possible to conduct my research in Australia and Germany and providing financial support and outstanding infrastructure. I am grateful to QUT for providing the HDR Tuition Fee Sponsorship.

I would like to thank QUT's Central Analytical Research Facility (CARF), the School of Chemistry and Physics, and the Faculty of Science for their support and excellent infrastructure.

In addition, I am grateful to Martin, who has acted as a mentor over the past three years, providing advice, guidance and engaging discussions.

I am thankful to my supervisory team consisting of top-class scientists. Above all, I am grateful to Florian for his exceptional guidance and superb support during my research in Germany and Australia. Furthermore, I am thankful to Paul for his support, assistance with operating multiple printing setups, conducting experiments while I was in Australia and helping to prepare the ZnO manuscript. I would like to thank Xingyu for helping me with operating the printing setup in Australia and her guidance during my stay. I want to thank my entire supervisory team for fostering a pleasant working

atmosphere, the productive meetings, engaging discussions, taking time to provide feedback and innovative ideas.

I am grateful for the brilliant chemists and physicists at INT that I can call both my colleagues and friends. I genuinely appreciate the delightful working atmosphere and after-work program. It was a pleasure to share office space and laboratories with you. Above all I am thankful to Jan and Steven for their support, contagious good mood and interesting discussions. Moreover, I am thankful to Jan for his feedback, helping me to improve my presentations. In the end, I even won a prize for the best presentation at the Nanotage. I am grateful to Aidan and Steven for their support and companionship.

I would also like to thank the group of Claus for their support. I would like to thank Christian for his support, the enjoyable working atmosphere, interesting discussions and for proofreading the thesis. I am thankful to Henriette Gröger, Nicole Klaasen, and Esther Bayon for their help performing measurements.

I am thankful to my students Maximilian and Anton for their synthetic support.

I would like to thank Kristian Kraft, Lukas Grünewald, Konstantin Faershteyn, and Agnes Morrissey for their support and fruitful discussions.

I want to thank Petra Bauer and Anette Baust for their support in organizing my stay in Australia and attending conferences.

I am thankful to my friends – Carl, Ralph, Cara, Ali, Dominik, and Paul – for the fun times during my studies. Even though we have all gone in different directions, it is always a pleasure to meet up with you.

I am indescribable grateful to my family – Bernhard, Sonja, Oma Gertrud, and Opa Rudolf – for their support throughout my chemist career and during my moves from Germany to Australia and back to Germany. I deeply appreciate their advice and support in navigating and overcoming various challenges. Thank you sincerely for your trust and love.

Finally, I am grateful to my partner Kai-Ching for her support, for helping me conduct experiments, making me laugh during difficult times, video calls while I was in Australia, and visiting me at the end of my stay in Australia to share one of the most breathtaking holidays I have ever experienced. Thank you sincerely for being there through both the highs and lows of my journey.

Table of Contents

LIST OF FIGURES

LIST OF TABLES

ABBREVIATIONS

%	Percent
2D	Two-dimensional
3D	Three-dimensional
4D	Four-dimensional
A	Ampere
ACQ	Aggregation-caused quenching
AM	Additive manufacturing
ARS	Alizarin Red S
a.u.	Arbitrary units
BS	Beam splitter
°C	Degree Celsius
CAD	Computer aided design
cm	Centimeter
CW	Continuous-wave
DA	Diels-Alder
DEABP	4,4'-bis(diethylamino)benzophenone
DLP	Digital-light processing
DLS	Dynamic light scattering
DMAPAm	N-(3-dimethylaminopropyl)methacrylamide
DMD	Digital micro-mirror device
EA	Elemental analysis
EBSD	Electron backscattering diffraction
EDXS	Energy-dispersive X-ray spectroscopy
e.g.	exempli gratia
ESB	Energy selection backscatter
eq.	Equivalents
FIB	Focused-ion beam
FMN	Flavin mononucleotide
FT	Fourier transformation
FT-IR	Fourier-transform infrared spectroscopy

g	Gramm
h	Hour
HAADF-STEM	High-angle annular dark field scanning transmission electron microscopy
HRTEM	High-resolution transmission electron microscopy
ICG	Indocyanine green
IOH-NPs	Inorganic-organic hybrid nanoparticles
IPF	Inverse pole figures
IR	Infrared light
IR-820	New indocyanine green
ISC	Intersystem crossing
LAP	Lithium phenyl-2,4,6-trimethylbenzoylphosphinate
LED	Light emitting diode
mg	Milligramm
min	Minute
mL	Mililiter
µm	Micrometer
mm	Milimeter
M_n	Number-averaged molar mass
mW	Milliwatt
N_2	Nitrogen
NIR	Near-infrared light
nm	Nanometer
NPs	Nanoparticles
Ns	Nanosecond
O_2	Oxygen
PEGDA700	Poly(ethylenglycol)diacrylate
PETA	Pentaerythritol triacrylate
PTC	Perylene-3,4,9,10-tetracarboxylate
PTCDA	Perylene-3,4,9,10-tetracarboxylic dianhydride
PXRD	X-ray powder diffraction
ROS	Reactive oxygen species
s	Second
SEM	Scanning electron microscopy

SHG	Second harmonic generation
Si	Silicon
SiO_2	Silica
SLA	Stereolithography
STEM	Scanning transmission electron microscopy
STL	Standard tessellation language
t	Time
TEM	Transmission electron microscopy
TGA	Thermogravimetric analysis
UV	Ultraviolet
UV-Vis	Ultraviolet-visible
V	Volt
wt-%	Weight percent
XPS	X-ray photoelectron spectroscopy

CHAPTER 1: INTRODUCTION

Additive manufacturing (AM) has emerged as one of the most disruptive technologies over the past decades due to its ability for rapid prototyping of complex structures, reduction of waste, and compatibility with a wide range of materials.[1,2] Depending on the material, size, and geometry of the envisaged object, several 3D printing techniques can be used to fabricate micromaterials. However, each approach has its own disadvantages and limitations. On the one hand, nanofabrication methods such as electron beam lithography, are time consuming and expensive due to multiple fabrication steps.[3] On the other hand, methods such as 3D inkjet printing are limited in their minimum feature size, which typically does not allow printing smaller features than a few microns, and requires post-processing steps such as sintering.[4]

Among the various AM techniques are photo-induced printing techniques, such as digital-light processing (DLP) and stereolithography (SLA). In contrast to other AM techniques, photoinduced-printing techniques enable the fabrication of well-defined structures due to their high spatiotemporal resolution using photoresin composed of a photoinitiator and a monomer/oligomer.[5] In light-driven 3D printing, light produced from a laser or light emitting diode (LED) is tightly focused, providing the spatiotemporal precision. Subsequently, the photons are typically absorbed by a photoinitiator, which fragments into highly reactive species that induce photopolymerization of monomers or oligomers. During photopolymerization, the monomer/oligomer solidifies only in the illuminated areas, and a 3D object is produced in a layer-by-layer fashion.[4] The unsolidified photoresins can be reused to fabricate new 3D objects. In addition, light-driven printing techniques provide excellent chemical sensitivity, achieved by tuning the wavelength, intensity, exposure time, and photochemistry.[6,7] Thus, photo-induced printing techniques are used to manufacture materials for a wide variety of applications, ranging from medicine and sensing to soft robotics.[8,9] Due to their commercial availability, chemical resistance, and rapid polymerization kinetics, the most utilized photoresins are based on (meth)acrylates.[10] However, this significantly limits the property profile of fabricated materials. Over the past decades, the demand for responsive and adaptive materials has grown.[11–13] A common strategy to enrich the mechanical, chemical, and physical properties of 3D printed objects relates to the incorporation of fillers within the photoresins.[14] The minimal heat generation associated with light-driven printing makes these techniques compatible with the usually thermally-sensitive fillers.[9]

Among these fillers are NPs, which are especially attractive due to their small size, enabling high loads in the 3D printed object.[14] NPs are particles typically smaller than 100 nm, and they have been used since late antiquity, when glass was colored with nanosized colloidal gold.[15] Moreover, NPs provide unique properties compared to their bulk material counterparts, due to their high surface-to-volume ratio, enabling their use in a great variety of applications, for instance, medicine, catalysis and sensing.[15] However, the integration of NPs as fillers in photo-induced printing presents significant challenges, to date.[14,16] Generally, NPs are prone to aggregation in photoresins, which can reduce their functionality and impede the printing process. Moreover, mixing NPs with a photoresin leads to an increase in viscosity, causing poor wetting of the printer's building platform. During the printing process, the NPs within the photoresin can scatter the incident light, which reduces the resolution and penetration depth. Finally, photodegradation of the NPs can occur when exposed to light and upon reaction with the reactive species generated by the photo-induced fragmentation of the photoinitiator. Thus, careful selection of the appropriate components to prepare composite-material inks is essential.

Recently, the working group of Claus Feldmann introduced the novel material concept of inorganic-organic hybrid nanoparticles (IOH-NPs), which comprises a saline composition with an inorganic cation and a functional organic anion, forming insoluble NPs in water.[17] For instance, the aqueous synthesis of IOH-NPs can be carried out using zirconyl chloride and dyes containing phosphate moieties to form a water-insoluble compound. In addition, exchanging the cation can also be used to introduce responsiveness (e.g., Gd^{3+}) to achieve magnetic response.[18] The IOH-NPs exhibit excellent photostability and colloidal stability as well as biocompatibility and high dye loads. Using different luminescent dyes to form IOH-NPs, for instance a pH-indicator, a response to an external stimulus, such as pH, can be achieved.[19] These IOH-NPs are highly attractive for the fabrication of responsive composite materials for various optical sensing applications using light-driven 3D printing.

Due to its high sensitivity and rapid response times, luminescence is an ideal tool for all kinds of sensing and monitoring. The detection of small fluctuations in chemical environment (e.g., pH) by luminescence read-out is easy, selective, and non-invasive. The read-out of the luminescence can be based on luminescence intensity changes, off-on luminescence, and luminescence shift.[20] Whereas luminescence intensity changes and off-on luminescence are strongly concentration-dependent, luminescence shifts exhibit enhanced sensitivity and reduced concentration dependency. Limitations of luminescence-based sensing originate from photobleaching, photodegradation, and luminescence quenching, for instance, in water.[21,22] However, these factors are mitigated by using luminescent IOH-NPs as fillers, due to their aqueous synthesis and excellent photostability.

One aim of the present thesis is the fabrication of composite materials, exhibiting responsiveness to various external stimuli, such as pH and light, by incorporation of IOH-NPs in a polymer matrix using light-based printing techniques. The focus is the preparation of composite-material inks and the investigation of the responsiveness and sensitivity of the fabricated composite materials.

Besides inducing photopolymerization, the incident light of a tightly focused laser is converted into heat using an absorber, such as a dye or a coated substrate. At sufficient temperatures, the threshold for chemical reactions can be surpassed, and several reactions can take place.[4] For instance, thermally unstable metal-salt solutions can be utilized for inorganic printing due to their decomposition.[23] In recent years different approaches to utilize these photothermally-driven reactions to fabricate inorganic materials have been developed.[24,25] The fabricated inorganic microstructures further enrich the property profile of light-based printed materials. However, fabrication of inorganic matter is challenging and requires time-consuming extra steps. For example, the intense temperature can lead to microbubble formation due to boiling of the solvent, disrupting the printing process and increasing the feature size through microbubble-assisted printing.[4,26] As a consequence, the thickness of the absorbing layer and the solvent need to be carefully chosen. Presently, there is a gap in the literature regarding photothermal laser-induced printing of sub-micron inorganic materials directly from solutions.

Thus, another focus of the current thesis is the examination of photothermal laser-induced printing, leading to deposition of sub-micron metal and metal-oxide structures. In addition, by step-by-step printing of different metals and metal oxides, electronic devices can be fabricated, which represents the ultimate aim of the photothermal laser-induced printing.

In chapter 2, the theoretical background for fabrication of responsive composite materials, as well as photothermal laser-induced printing, is reviewed. Chapter 3 is devoted to the analytical methods and carried out fabrication techniques. The aims of the current thesis are summarized in chapter 4, and the materials used are given in chapter 5. The fabrication and characterization of responsive composite materials to pH, O_2, and light are discussed in chapters 6 to 9, respectively. In chapter 10 and 11, the results of the photothermal laser printing of metal oxides and metals are discussed. Finally, a summary of the results is provided in chapter 12 and additional future directions are given in chapter 13.

CHAPTER 2: THEORETICAL BACKGROUND

2.1 Photochemistry Essentials

Sunlight is always available and the source of life. It is mainly composed of ultraviolet (UV) (100 – 400 nm) and visible light (400 – 700 nm).[27,28] Thus, harnessing energy in the form of light as a source to achieve milder reaction conditions and spatiotemporal control over chemical reactions is a highly attractive proposition.[29,30] The fundamentals of photochemistry were initially discussed in the 19th century by the first principle of photochemistry also known as Grotthus-Draper law, which states that light needs to be absorbed to cause chemical change.[31] The measure of how strongly light is absorbed by a certain molecule in solution at a given wavelength is described by Beer-Lambert's law (equation 1.1).[28]

$$A = \varepsilon \cdot l \cdot c \qquad (1.1)$$

A = absorbance; ε = molecular extinction coefficient; l = path length; c = concentration

The interaction of light with molecules and the corresponding electronic transitions can be described by a Jablonski diagram (Figure 1).[32]

Upon light absorption (10^{-18} s), the transition of an electron from the vibronic ground state of the electronic ground state S_0 to a higher vibronic state of the excited state S_1 takes place.[33] According to the Franck-Condon principle, such electronic transition occur vertically.[28] The vertical excitation can be explained by the Born-Oppenheimer approximation,[28] which assumes that electronic transitions are much faster compared to nuclear motion.[28] Next, rapid vibrational relaxation (10^{-12} s) from a higher vibrational state of S_1 to the vibrational ground state of S_1 occurs.[33] The vibrational energy is being released in the form of thermal energy. From here, the electron can either relax non-radiatively to S_0 or emit a photon upon decay to S_0, which is called fluorescence and takes place within 10^{-9} s.[34] The absorption wavelength used for excitation is lower than the emission wavelength, which is referred to as a Stokes shift.[32] Another process is Intersystem Crossing (ISC), a radiation-free transition from the excited singlet state to the triplet state T_1. Furthermore, ISC is quantum mechanically forbidden but enabled by spin-orbit interaction of heavy atoms.[27] The radiative transition from T_1 to S_0 is called phosphorescence and quantum mechanically forbidden with lifetimes up to hours.[34,35]

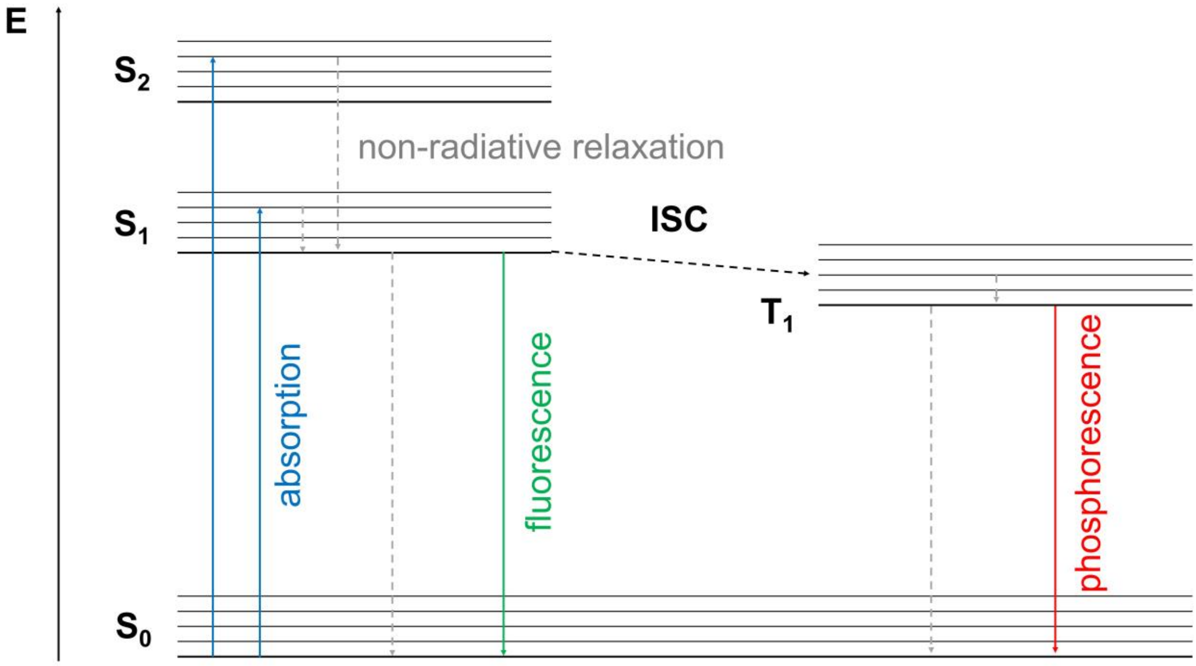

Figure 1. Simplified Jablonski diagram for schematic representation of the interaction of light with molecules. Radiative transitions are shown as straight lines and non-radiative process are highlighted as dashed lines (adapted from ref[34]).

2.2 Free Radical Photopolymerization

Free radical photopolymerization is one of the most used methods to fabricate photopolymers.[36–39] The process involves three parallel occurring main steps: initiation, propagation and termination (Figure 2).[37] In the initiation step, highly reactive radicals are generated upon irradiation of the photoinitiator with UV or visible light.[40] There are two different kinds of photoinitiators. The Norrish Type I absorbs light and undergoes homolytic cleavage resulting in generation of two radicals and the Norrish Type II, which is excited by light and generates a radical upon abstraction of hydrogen or electrons from a co-initiator in its triplet state.[38,39] Subsequently, the reactive radicals react with unsaturated bonds of monomers, typically (meth)acrylate or styrene derivatives.[37,39] During the chain growth further monomers are consumed by the reactive species leading to the propagation of long chains. The final step in the life of a propagating radical is the termination of the chain, which takes place through recombination, disproportionation, chain transfer, physical trapping or quenching with an inhibitor. Nowadays, free radical photopolymerization is used in adhesives, microelectronics and biomedical applications.[37,41]

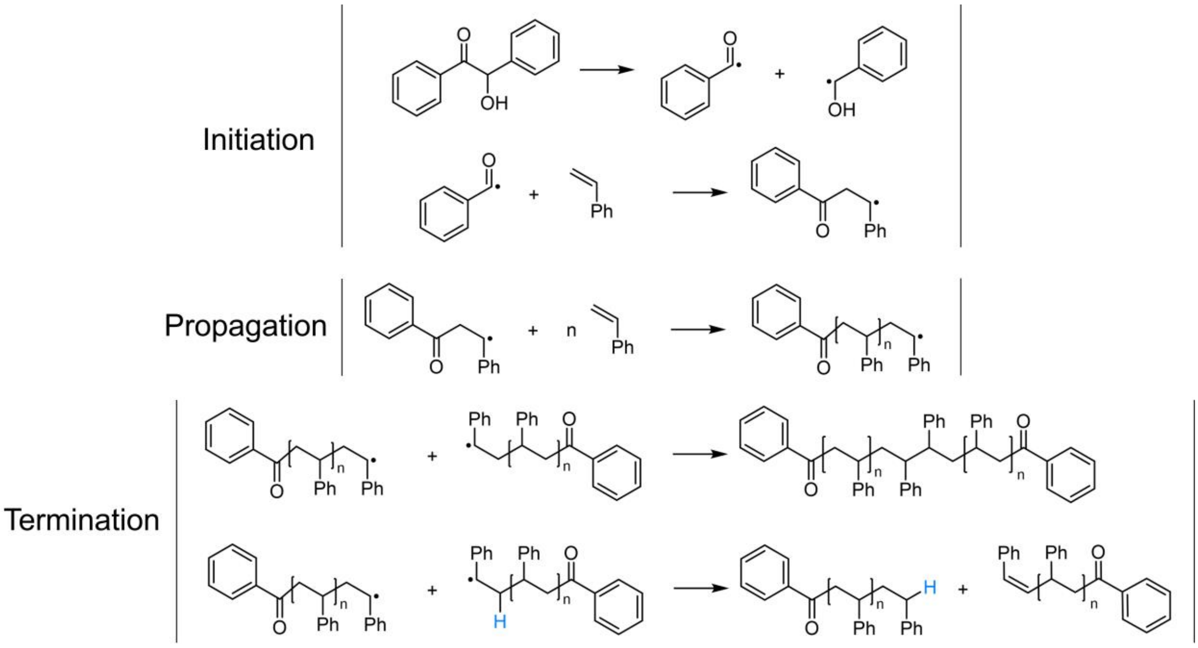

Figure 2. Free radical photopolymerization of styrene using benzoin as the photoinitiator.

Some examples of commonly used UV photoinitiators, monomers and oligomers for AM are shown in Figure 3. Acrylate derivatives such poly(ethylenglycol)diacrylate (PEGDA700) and pentaerythritol triacrylate (PETA) are often used as monomers and oligomers[39] due to their commercial abundance and fast polymerization kinetics. In addition, a wide variety of mono- and multifunctional acrylates exists, enabling tuning of the resin viscosity and functionalities and control over mechanical, thermal and optical properties.[42,43] Small quantities of photoinitiator can be readily dissolved in various acrylates, which simplifies the preparation of resins for AM. The disadvantage of acrylates used in AM are shrinkage of the photopolymer and oxygen (O_2) inhibition.[44,45]

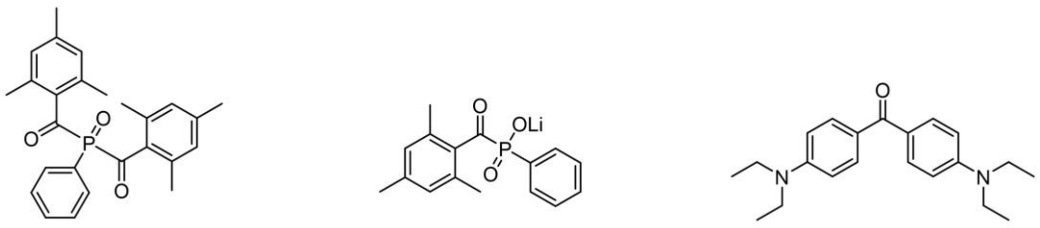

Phenyl-bis(2,4,6-trimethylbenzoyl) phosphinoxid

Lithium-Phenyl-2,4,6-trimethylbenzoylphosphinat

4,4'-bis(N,N-diethylamino)benzophenone

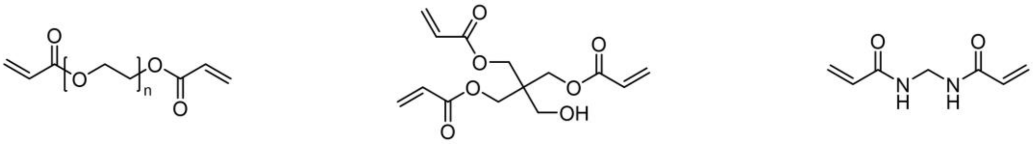

Poly(ethylenglycol)diacrylate

Pentaerythritol triacrylate

N,N'-methylenediacrylamide

Figure 3. Examples of commonly used UV photoinitiators, monomers and oligomers.

2.3 Additive Manufacturing

Recently, AM has gained substantial attention for the fabrication of industrial and medical components due to its cost-effectiveness and potential to reduce waste.[46] AM techniques are based on three key step (i.e., designing, printing and post-processing of the desired 3D structure). The desired 3D object is manufactured using a computer automated design (CAD) program and converted into a format such as standard tessellation language (STL), which can be read out by a printer.[37] Since their emergence in the 1970s, light-driven AM techniques have become disruptive technologies due to the spatiotemporal control of chemical reactions enabling well-defined, high-resolution 3D objects.[47] For the printing process a photo-sensitive resin is polymerized upon irradiation by different light sources depending on the applied AM technique. In the current thesis, DLP and SLA have been used to fabricate 3D objects and are described in more detail below.

2.3.1 Digital-Light Processing

DLP was pioneered in 1987 at Texas Instruments.[48] It is exploited to fabricate complex 3D polymers, ceramics or metal objects due to low cost of the printer and user-friendliness.[37] The printed structures are employed in a wide variety of applications such as biomedicine,[49] electronic and piezoelectric devices,[50,51] healable scaffolds[52] and optical fibers and lenses.[53] The heart of a DLP printer is the digital micro-mirror device (DMD), which generates images composed of light and dark pixels to solidify an entire layer. Thereby, the DMD determines the *XY*-plane resolution commonly about 40 x 40 µm.[54] Ultimately, the 3D object is fabricated in a layer-by-layer fashion. Subsequently, the 3D structure is removed from the building head, and unsolidified starting material is washed off. Sometimes, this development step is followed by post-processing (e.g., sintering or debinding) of the polymer to yield ceramics or metal 3D objects. There are two configurations of a DLP printer (Figure 4). First, the bottom-up configuration with the build head dipped in a transparent resin container. The UV light source is located at the bottom of the transparent resin container. After the first layer was solidified the build head moves upwards to create the 3D structure. Second, in the top-down configuration, the light source is located above the resin container, and the build head is completely immersed in the photoresin. The build head moves downwards after the first layer is cured to generate a 3D object. Both configurations offer different advantages. For the bottom-up configuration less resin is needed for fabrication, whereas for the top-down configuration the adhesion of the solidified polymer is better and even highly viscos photoresins can be used for printing.[37]

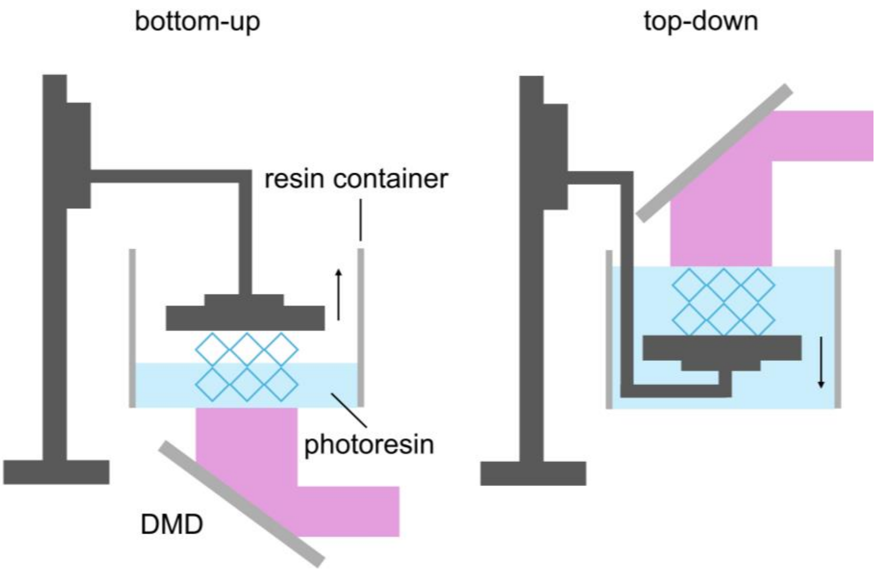

Figure 4. Schematic representation of bottom-up and top-down configuration of DLP printers (adapted from ref[55]).

Commonly, the photoresin is composed of monomer or oligomers and a photoinitiator. The ratio of these precursors influences the mechanical properties of the solidified photopolymer. In addition, the fabrication process can be adjusted by the molecular weight of the monomer or oligomer. On one hand, high-molecular-weight precursors lead to enhanced mechanical strength of the fabricated structure and increased viscosity of the resin, which hinders re-coating of the building head. On the other hand, low-molecular-weight precursors result in a longer exposure time and a decrease in mechanical strength and viscosity.[37] The most often used precursors are (meth)acrylate-based monomer and oligomers.[37] To yield a higher number of reactive species co-initiators, dyes or photosensitizers can be mixed into the photoresin. In addition, micro and nano-sized ceramic or metal fillers can be added to the resin to adjust material properties such as mechanical strength or electrical conductivity giving rise to the fabrication of, for instance, electronic devices. However, fillers can interfere with the light penetration, scatter incident light and increase viscosity, ultimately hindering the printing process. To fabricate ceramics, for instance, the filler content is close to 50 wt-%, and the polymer is burned out at approximately 600°C.[56] Other additives added to photoresins are radical inhibitors, for instance, butylated hydroxy toluene, which prevents premature gelation of the resin when added in small quantities of 50-200 ppm.[57]

2.3.2 Stereolithography

SLA was invented in 1986 by Charles Hull[58] and is known for rapid prototyping. This printing method is employed in applications ranging from tissue engineering to fabrication of electronic devices. The light source is a focused laser that is scanned over the photoresin point-by-point to solidify the starting material. By scanning the laser in *z*-direction, a 3D object is fabricated. Analogous to DLP, an SLA printer can be built in either bottom-up or top-down configuration. The top-down configuration is usually preferred as the laser is confined in the printer, and an easier recoating of the building head is achieved in this configuration (Figure 5). Predominately photoresins composed of (meth)acrylate derivatives or/and epoxides are used for printing.[36] The advantage of SLA is the high resolution of 10 µm,[59] but the fabrication of large structure arrays is more time consuming compared to DLP.

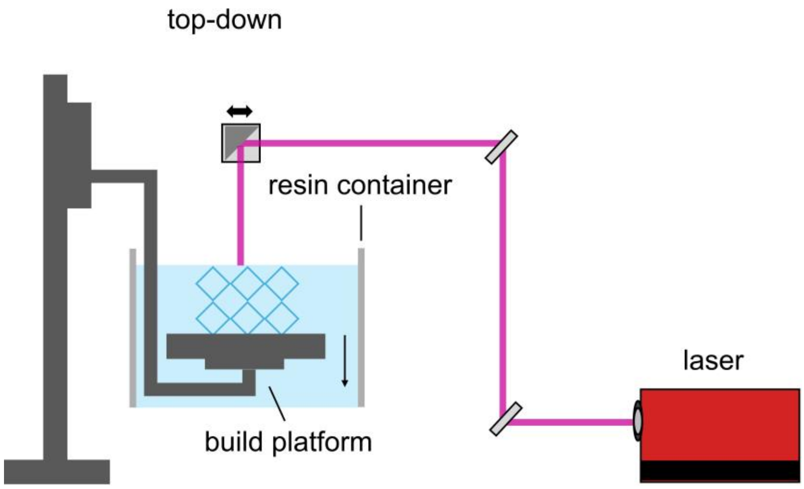

Figure 5. Schematic representation of an SLA printer (adapted from ref[60]).

2.4 Organic Photoresins

An organic photoresin is a light-sensitive organic material, which can be patterned into solid structures due to photoinitiated polymerization when exposed to UV or visible light. Usually, a photoresin is composed of a photoinitiator, a monomer/oligomer and additives. Additives can be used to adjust the viscosity of the photoresin or to improve the mechanical and physical properties of the fabricated material. Photoresins can be categorized into positive-tone or negative-tone resins.[61] After light exposure, for positive-tone resins, the exposed regions become soluble, and the unexposed regions remain. In contrast, for negative-tone resins, the exposed regions are crosslinked and solidified, while the unexposed regions can be washed away. Furthermore, organic photoresins can be classified by the photoinduced reaction that takes place to fabricate a 3D material.

Radical photopolymerization (described in section 2.2) is the most commonly used mechanism in 3D printing utilizing organic photoresins.[61] Multi-functional (meth)acrylates are the most widely used in radical photopolymerization due to rapid polymerization kinetics, high crosslinking density, and good photoinitiator compatibility.[61] Common acrylate derivatives utilized for AM are polyester acrylates, and polyether acrylates, such as polyethylene glycol diacrylate[62,63] or trimethylolpropane triacrylate,[64,65] which exhibit toughness and high Young's modulus. Disadvantages of using (meth)acrylates as monomers/oligomers are brittleness, O_2 inhibition,[44] and shrinkage of the fabricated material.[61]. For instance, a photoresin comprising a blend of polyethylene glycol diacrylate, 2-hydroxyethyl methacrylate, and 2-(2-methoxyethoxy) ethyl methacrylate has been used to fabricate a 3D material using DLP, exhibiting responsiveness to humidity and temperature by undergoing shape deformation.[66]

In addition to radical photopolymerization, cationic photopolymerization has gained significant attention due to low shrinkage[54] and absence of O_2 inhibition.[44] In cationic photopolymerization onium salts (e.g., triarylsulfonium hexafluoroantimonate and bis-(4-dodecylphenyl)iodonium hexafluoroantimonate)[68,69] are used as photoinitiators, which decomposes upon irradiation with UV or visible light, generating a superacid. Subsequently, the superacid initiates ring-opening polymerization by protonating, for instance, an epoxy moiety, forming a carbocation resulting in chain propagation. In addition, cationic photopolymerization proceeds even in the absence of light. The generated superacid remains active in the dark, continuing to protonate monomers, and the polymerization becomes self-sustained.[69] Typically used monomers are cycloaliphatic epoxides, glycidyl ethers and oxetanes.[1,8] The reactivity of epoxy-based monomers highly depends on the ring strain (e.g., cycloaliphatic epoxides) exhibit rapid polymerization due to high double ring strain.[54] Limitations of cationic photopolymerization are moisture inhibition and acid-initiated side reactions.[69]

Recently, thiol-ene and thiol-acrylate-based photoresin have gained attention due to unique step-growth polymerization, offering reduced shrinkage, rapid polymerization kinetics and enhanced biocompatibility compared to (meth)acrylate-based photoresins.[8,10] In addition, step-growth enables simple post-functionalization by tailoring the functional groups within the photoresin.[61] The photoinitiation takes place by common photointiators or the thiol itself, generating a thiyl radical when exposed to UV or visible light. Subsequently, the thiyl radical reacts with C=C double bond to form a carbon-centered radical, which abstracts a hydrogen from another thiol in a chain transfer reaction, regenerating the thiyl radical and repeating the cycle.[61] This leads to near-quantitative functional group conversion. Common ene monomers are multifunctional allyl ethers, norbornene derivatives, and thiol-ene oligomers. The most widely used thiols are pentaerythritol tetrakis(3-mercaptopropionate),[54] and trimethylolpropane tris(3-mercaptopropionate),[70] leading to formation of dense polymeric networks combined with good compatibility with other monomer classes such as acrylates for improved modulus.[71] Disadvantages of using thiol-ene-based photoresins are their odor, poor shelf-life due to oxidative sulfide bond formation. Thus, stabilizers are added to prevent oxidative sulfide bond formation.[71] In addition, they exhibit a low refractive index, limiting their utilization in optics and industrial applications. For instance, degradable thiol-ene polymer 3D structures have been fabricated by DLP of cellulose-derived levoglucosenone dienes and pentaerythritol tetrakis(3-mercaptopropionate).[72]

There are also photoinitiator-free photoresins offering reduced costs and simple handling, while possessing decreased photosensitivity and slower polymerization kinetics compared to above-described photoresins. The polymeric network is formed by [2+2] or [4+4] photocycloaddition of multifunctional pre-synthesized monomers/oligomers introducing a great range of functional groups. Later, these functional groups can be used for post-functionalization to modify the chemical, physical and mechanical properties of the fabricated structure with ease. According to the Woodward-Hoffmann rules, these photocycloadditions are only photochemically permitted, and the photocycloaddition products can be photochemically reversed.[61] For instance, the dimerization of coumarin, a [2+2] photocycloaddition, is photo-reversible using light of 254 nm.[73] This can be used for the fabrication of erasable 3D structures. Common photoresins are comprised of multi-functional maleimides, naphthalene, and cinnamate.[62,74] For example, out-of-equilibrium structures have been fabricated by visible-light-driven cycloaddition of triazolinedione to naphthalene using two-photon polymerization.[75] The 3D structure remained stable upon continuous irradiation with green light, but degradation of the material takes place in the dark due to covalent bond dissociation. Such a photoresin can be used in removable, sacrificial scaffolds during 3D printing. Up to now, its use in 3D printing is limited due to complex precursor synthesis, high exposure doses, and slow printing speeds.

2.5 Recent Advances in Organic Photoresins

The state of the art in radical-chain growth photopolymerization of (meth)acrylates comprises the synthesis of new photoinitiators that enable improved depth cure combined with reduced toxicity,[76] and incorporation of other oligomers (i.e., epoxides and thiols) to reduce shrinkage and brittleness.[72] In addition, a trend towards bio-based acrylates, such as lignin, is emerging, resulting in recyclable photoresins from renewable feedstock.[77,78] These advances not only improve the mechanical and chemical performance of the printed materials but also expand the range of functional applications. Recent advances in cationic photopolymerization focus on the synthesis of photoinitiator-sensitizers to achieve photoactivation in the visible range,[79,80] as well as creating blends of acrylate-epoxy or thiol-epoxy photoresins, which offer low shrinkage and improved mechanical stability.[81,82] Blends of different photoresin exhibit interesting behaviors, such as multi-color printing. For instance, a multicomponent acrylate-epoxide-based photoresin has been utilized, further containing a mixture of the photoinitiators Irgacure 819 and triarylsulfonium salt, which undergoes radical polymerization by irradiation with visible light and cationic polymerization upon UV radiation.[83]

Furthermore, advances for some photoresins were made in the incorporation of NPs (e.g., titanium oxide and silica) to fabricate ceramics with high thermal stability.[37] Efforts have also focused on engineering dynamic responsiveness to external stimuli (e.g., heat, light, and moisture).[84] Photoinitiator-free photoresins are being studied extensively, such as those based on dynamic Diels-Alder (DA) cycloadditions, disulfides and boronic esters due to fast reaction rates and excellent functional group tolerance.[84,85]

2.6 Light-based Printing Mechanisms

As stated above, laser-based printing is used in a wide variety of applications. Laser-based printing can be categorized into two categories: Directed local synthesis, for instance, comprising DLP, SLA, and directed assembly of preformed materials.[4]

2.6.1 Directed Local Synthesis

In directed local synthesis, a liquid resin or dissolved precursors are locally solidified by either single-photon absorption, multi-photon absorption or thermally-driven reactions. Within the scope of the current thesis, only single-photon absorption is highlighted in the following.

Single-photon absorption occurs when one photon with enough energy to excite an electron from the ground state to a higher excited state is absorbed, promoting photopolymerization, as is the case for DLP and SLA. This process enables the fabrication of 3D structures in a point-by-point and/or layer-by-layer fashion.

2.6.2 Directed Assembly of Preformed Materials

Photothermal laser printing, microbubble-assisted printing and optical forces are used in directed assembly of preformed materials. In the present thesis, photothermal printing has been employed to fabricate semiconductor materials.

In photothermal laser printing, a continuous-wave (CW) laser is used to generate a temperature gradient leading to separation of metal complexes or metal salts into ions and liquid motion. The resulting electrical field from the metal-precursor separation and the motion of the liquid lead to a deposition of the metal or metal oxide in the focal spot of the laser.[4,23,24] To generate a temperature gradient, the laser beam needs to be either absorbed by the ink or the substrate (Figure 6). Transparent inks can be tuned by adding a dye. 3D printing is achieved if either the ink or the deposited material absorbs the laser radiation. However, the intense temperature can lead to microbubbles formed due to boiling of the solvent, disrupting the printing process and increasing the feature size.[26] As a consequence, the thickness of the absorbing layer and the solvent need to be chosen carefully. Compared to single-photon polymerization, there are less thermally-driven reactions currently reported for the fabrication of metal microstructures.[25,86–88] For instance, the heat generated by a 639 nm CW laser beam has been used to trigger solid-solid transformation.[89,90] A $16SbI_3$-$84Sb_2S_3$ precursor glass was prepared to photothermally laser print crystalline SbS_3. However, the resolution of this approach is close to 5 µm and restructuring of the substrate occurs due to the high laser powers applied. Liquid-solid photothermal laser-induced printing was demonstrated [91] to thermally deposit amorphous metal oxides from water-based solutions onto platinum, which acts as absorbing layer by irradiation with an 750 and 532 nm CW laser, respectively.[24,25] In addition, non-transparent inorganic precursors like $(NH_4)_2RuCl_6$ have been utilized to fabricate Ru metal wires directly from solution.[91] However, these authors only achieved resolutions between 5-10 µm. In sum, there is currently a gap in the literature regarding photothermal laser-induced printing of sub-micron inorganic materials directly from solution. However, fabricating metal and metal-oxide nanostructures is gaining attention due to the fact that these nanomaterials have unique properties and usually also the same electrical conductivity compared to the bulk material.[25,93–99]

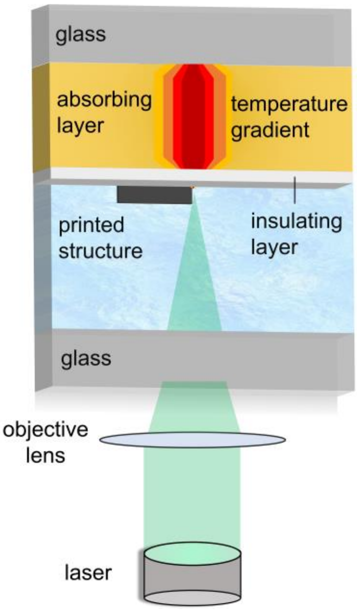

Figure 6. Schematic representation of photothermal laser printing (adapted from ref[23]).

In addition, by step-by-step printing of different metals and metal oxides, electronic devices can be fabricated, which is the final aim for the photothermal laser-induced printing. Therefore, literature addressing the printing of electronic devices is reviewed in the following section.

2.7 Fabricating Electronic Devices via Photothermal Metal Printing

Electronic devices play a critical role in our daily lives. Therefore, fabricating smaller and more compact electronic devices is paramount. To fabricate a large variety of electronic devices such as diodes, capacitors, and transistors, it is necessary that one can print conductive metals, different types of semiconductors (*n*-type/*p*-type), insulators and dielectrics. Moreover, light-emitting inorganic materials, including gallium nitride for photoelectronic devices, are also considered highly desirable. However, printing in an O_2-containing atmosphere would lead to oxide contamination of such materials. Thus, printing of inorganic material is restricted to printing of precious metals and more easily accessible metal oxides. Therefore, new printing approaches such as thermally-driven reactions in which the same ligands or anions can be used to manufacture metal oxides with different properties are of high interest. For instance, targeting the decomposition of metal acetylacetonates could lead to *n*-type zinc oxide, *p*-type copper oxide or insulators such as aluminium oxide. The printing itself can be carried out in different modes, whereby the "sandwich mode" is the simplest option to print several different layers on top of another. Here, the ink is sandwiched between two coverslips. The laser beam comes from beneath and passes through the first glass coverslip as well as the ink. It is subsequently focused on the interface between ink and second glass coverslip, where the printing takes place. Using the sandwich-printing mode, the laser beam avoids being blocked by previous fabricated microstructures and the next metal or metal oxide can be deposited on top of the already deposited structured material.

Recently, our group[25] was able to print the first electronic devices that comprise diodes and memristors by DLW. These electronic devices are composed of platinum and silver metal with zinc oxide printed in between them as a semiconductor. The metals were printed by MPR of metal salts, and the semiconductor was printed onto platinum driven by single-photon absorption of platinum, causing local heating, leading to deposition of zinc oxide. The main advantage of the above-described method is that it does not require any post-treatment at elevated temperatures to enhance the performance of the electronic devices. However, we only printed conductive metals and a single *n*-type semiconductor. Moreover, both metals need to be printed with a femtosecond laser, which makes this process expensive. In addition, the inks employed are not orthogonal due to their pH sensitivity and need to be printed in the order platinum → zinc oxide → silver. Otherwise, the silver would be dissolved by the later printing of zinc oxide due to the presence of ammonia in the zinc oxide ink. Thus, new inks need to be prepared that suit orthogonal thermally-driven printing of metals and metal oxides (Figure 7). To date, no microelectronic or optoelectronic device was fabricated by photothermal laser-induced printing.

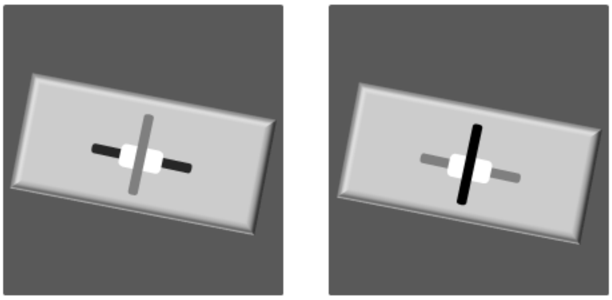

Figure 7. Orthogonal printing of metals and metal oxides: (Left) A metal (black) is deposited on the substrate and on that metal a metal oxide (white) is printed. Finally, another metal (grey) is printed over the metal oxide. (Right) A metal is deposited on the substrate (grey) and on that metal a metal oxide (white) is printed. Finally, another metal (black) was printed over the metal oxide.

Furthermore, there are electronic devices that currently cannot be printed, such as transistors or capacitors due to the lack of orthogonal inks. These components require the printing of an insulator like aluminium oxide, which can be already thermally printed. For instance, field-effect transistors can require that metal and semiconductor are separated by an insulator or for fabricating capacitors two metal sheets need to be separated by an insulator.[99]

2.8 Four-Dimensional Printing

Four-dimensional (4D) printing has been introduced by Skyler Tibbits in 2013[100] and since then 4D printing has gained a lot of attention. The fourth dimension refers to time 3D printed structures need to respond and adapt to external stimuli such as temperature, light, magnetism, and pH.[101–103] As a result, the fabricated object undergoes a controlled change of its physical or/and chemical properties over time due to the exposure with external stimulus. Through 4D printing static 3D printed structures turn into adjustable dynamic structures often called “smart materials”. Smart materials outperform static structures in applications based on advanced material properties such as sensing, shape memory or self-repair while still sharing the same benefits of rapid production and being sustainable by saving energy, costs and time.[101–103] In general, responsiveness and adaptivity to external stimuli, such as light, pH, heat or specific chemical moieties in the face of autonomous and intelligent behavior, are highly desirable properties.[104] However, fabrication of such smart materials still remains challenging.[105] Typical applications of smart materials include drug delivery,[106] tissue engineering,[107] electronics,[108] and soft robotics.[109] The downsides of 4D printing are the complexity of the fabrication process and the structure of smart materials.

In general, 4D materials can be categorized into three classes: The first class relates to hydrogels, which are distinguished by biocompatibility, ionic conductivity and absorbing large amounts of fluids, making 4D printed hydrogels highly desirable for healthcare, drug delivery and tissue engineering. The second class comprises liquid crystals, which offer high flexibility and fast response times making them attractive for soft robotics and optics. Finally, the third class focuses on composites renowned for enhanced mechanical strength, improved electrical and heat conductivity used as actuators and in drug delivery.[102]

Compared to the other two classes, the fabrication of composites allows a wider range of materials by embedding functional NPs in the polymer matrix, resulting in a broader range of material properties. Therefore, it is critical that the NPs are small. Their overall size distribution should be monodisperse, as large NPs (< 20 nm) can disrupt the printing process or lead to a smaller number of NPs in the ink. In addition, the NPs should not react with the photoinitiator. Fusing of inorganic and organic matter allows for a wide range of materials, resulting in a broad range of material properties. For instance, magnetism-driven soft actuators have been fabricated by addition of Fe_3O_4 NPs to acrylates using DLP.[110] However, an extra step is needed to provide the desired NPs, which makes the fabrication of composites more time-consuming.

In addition, 4D materials can be differentiated by the triggering external stimuli. For instance, the most often applied stimulus is temperature to perform mechanical manipulations due to easy exposure of the 4D structure. Applications for temperature-responsive smart materials are healthcare and drug delivery.[111] However, response times are often longer than for other external stimuli such as light enabling rapid and precise focused response utilized in drug delivery and optical devices.[103] The degradability of 3D structures due to irradiation can be achieved by introducing photolabile moieties in the photoresin.[112,113] Drug delivery can also be facilitated by the fabrication of magnetic- or pH-responsive smart materials.

2.9 Synthesis of Nanoparticles

By definition, NPs are particles with a size ranging from 1-100 nm.[15] The goal of NP synthesis is to yield small ,monodisperse, non-agglomerated particles, which can either be achieved via a “top-down” or “bottom-up” approach.[114] The “top-down” strategy is usually based on physical grinding of the bulk material, which often leads to polydisperse particles.[115] The latter is based on the liquid-phase synthesis of NPs from atomic or molecular units.[15] The processes occurring during NP synthesis under controlled reaction conditions can be divided into three different phases according to the LaMer-Dinegar model (Figure 8).[116]

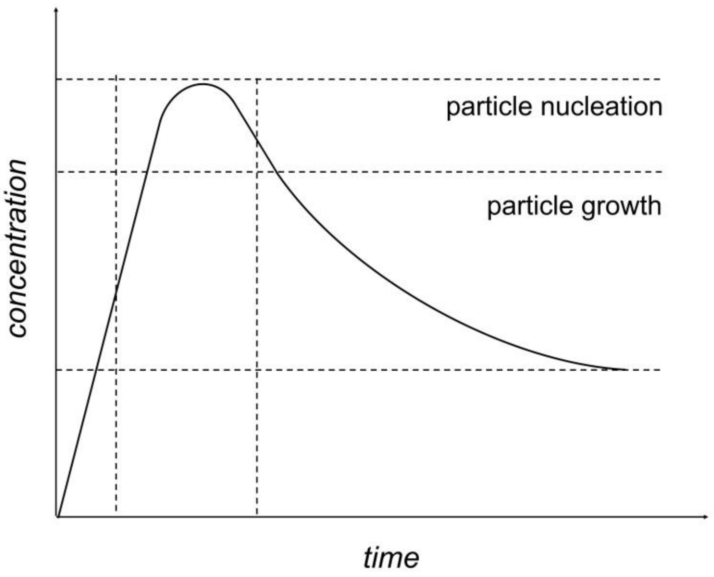

Figure 8. Schematic representation of the concentration-time-curve during NP synthesis according to LaMer-Dinegar.[116]

In the first phase, the addition of starting materials results in a fast increase in the concentration, leading to attainment of the solubility limit. The second phase (particle nucleation) takes place once the critical supersaturation is reached, causing lowering of the starting material concentration. After the concentration has decreased below the critical supersaturation, the third phase (particle growth) takes place.[116] To yield monodisperse NPs, endothermic nucleation and exothermic growth need to be separated. Therefore, often the “hot-injection method” is used where one of the starting materials is injected at high temperatures into a solvent containing a second starting material. Another effect leading to particle growth is the so-called Ostwald Ripening,[117] which becomes more pronounced the longer the suspension alters. In principle, Ostwald Ripening is a thermodynamically-driven phenomenon, which describes the particle growth of larger particles account of smaller particles. The driving force of the Ostwald Ripening is the minimization of the surface energy, which is lower for larger particles. Therefore, Ostwald Ripening needs to be considered critically for samples with a high polydispersity. The final process resulting in particle growth is particle agglomeration due to interaction between the particles, for instance, the strength of the repulsive force between two equally charged particle surfaces or the attractive Van-der-Waals interactions.

In summary, multiple parameters need to be considered to control NP synthesis. This includes the amount and ratio of the starting materials and progressing to external reaction conditions such as reaction time and temperature. Furthermore, mixing speed and pH have an essential influence on the resulting particle size. For instance, the latter plays a role for the electrostatic stability of the NPs. IOH-NPs are a specific kind of NPs with unique properties and therefore, the concept and synthesis of IOH-NPs is described in the following Chapter.

2.9.1 Concept and Synthesis of Inorganic-Organic Hybrid Nanoparticles

In 2015, the Feldmann group[118] introduced the concept of IOH-NPs. IOH-NPs have a saline composition that consists of an inorganic cation and a functional organic anion, which can either be a drug or a fluorescent dye. The common inorganic cations used for preparation of these NPs are La^{3+}, $[ZrO]^{2+}$, Gd^{3+}, Cu^{2+}, or Ag^{+}.[66,67] Furthermore, the concept requires functional anions with a phosphate, sulfonate or carboxylate group. IOH-NPs stand out through their low material complexity and high drug or dye load of up to 90 wt-%. The applications for these types of NPs range from drug delivery to multimodal imaging[19,118] due to the assembly of cytostatic, antibiotic and fluorescent anions. In addition, magnetic properties can be achieved through a judicious cation choice such as Gd^{3+}.[18] Overall, IOH-NPs can be synthesized through straightforward water-based precipitation synthesis. Therefore, organic anions are provided in a large volume of solvent followed by injection of a concentrated solution of the dissolved inorganic cations under vigorously stirring. In addition, the cation-to-anion ratio is chosen in favor of the negative charge carriers to ensure a negative surface termination, which assists stabilizing the IOH-NPs colloidally. During the synthesis, rigorous stirring is used for equal distribution of the starting materials leading to uniform grow conditions. Subsequently, the particle suspension is purified by repeated centrifugation (15 min, 12000-25000 U/min) and redispersion from/in water (typically two to three times), which was performed to remove remaining starting materials and salts.

CHAPTER 3: ANALYTICAL METHODS

The following section highlights the purpose and description of the analytical methods used to collect data for structures and materials fabricated by photothermal and 4D laser printing as well as, for the synthesized IOH-NPs.

3.1 Electron Microscopy

Electron microscopy is used to study the size, morphology and homogeneity of nanomaterials. Furthermore, this technique provides evidence about the agglomeration of particles, especially in the nanometer range. In contrast to light, used as source for light microscopes, electron waves have a smaller wavelength thereby enabling a higher resolution. A typical resolution using visible light is 0.2 µm.[120] Furthermore, the resolution limit (*d*) is expressed by the Abbé equation.[121]

$$d = \frac{1.22 \cdot \lambda}{n \cdot \sin(\vartheta)} \qquad (2.1)$$

d = resolution; λ = wavelength; $n*sin(\vartheta)$ = numerical aperture

Higher resolution can be achieved by using accelerated electrons. The De Broglie relation says that the wavelength (λ) depends on their rest mass (m_0) and on their velocity (v).

$$\lambda = \frac{h}{p} = \frac{h}{m_0 \cdot v} \qquad (2.2)$$

h = Planck constant; p = impulse; m_0 = rest mass; v = velocity

This equation can be modified by accounting for relativistic effects on the electron mass occurring at acceleration voltages of 1-400 kV applied in electron microscopy.

$$\lambda = \frac{h}{p} = \frac{h}{\sqrt{2 \cdot m_0 \cdot e \cdot U \cdot \left(1 + \frac{e \cdot U}{2 \cdot m_0 \cdot c^2}\right)}} \tag{2.3}$$

e = elementary charge; U = acceleration voltage; c = velocity of light

By increasing the acceleration voltage, the wavelength is decreased, which leads to a higher resolution according to equation 2.1. There are two possible electron sources for generating the incident electron beam. A tungsten cathode or a Schottky field emission cathode. The latter electron source is zirconium oxide coated tungsten cathode with a very thin tip. Before interacting with the sample, the incident electron beam passes through the lens system. The function of the electron optic is to bring the electron beam into focus, correcting aberrations and scanning the incident beam in a raster scanning pattern for scanning electron microscopes (SEMs). In addition, the system is evacuated till ultra-high vacuum (10^{-9} mbar) in the electron beam column and high vacuum (10^{-5} mbar) in the sample chamber are reached. This procedure is necessary to ensure that no interactions of the electron beam with air molecules may occur.

In Figure 9, the different interactions of the incident electron beam with the sample are shown. By impinging of the incident beam on the sample, there is a possibility that the primary electrons are merely reflected leading to “backscattered electrons”. Likewise, the electron beam can knock out electrons of an inner electron shell, which are called “secondary electrons”. Due to the loss of these secondary electrons, holes are generated in the shell, which are filled by electrons of a higher shell under emission of X-rays characteristic for the element. In addition, the energy can be transferred to another electron, which is then ejected. Such an electron is called “Auger electron”. Finally, the incident beam can penetrate the sample completely and these transmitted electrons are deflected depending on the interaction with the sample.[122–124]

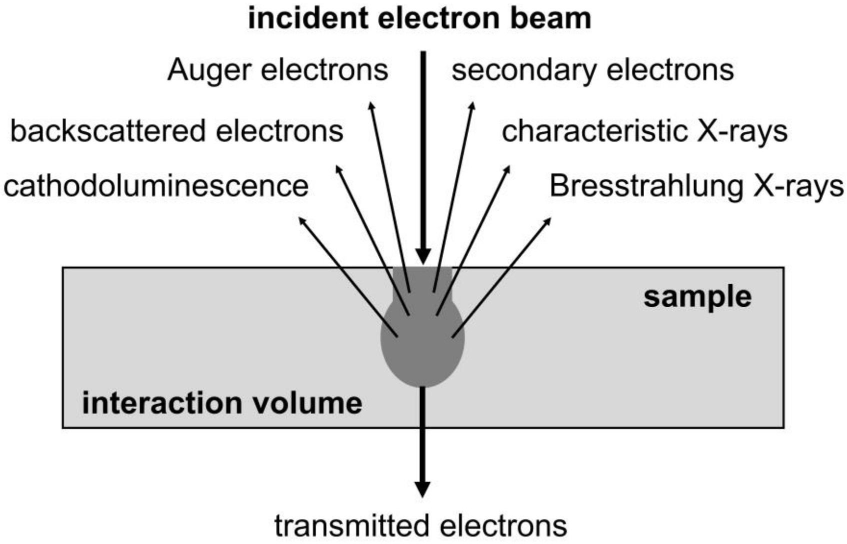

Figure 9. Interactions taking place between the incident electron beam and the sample (adapted from ref[125]).

3.1.1 Scanning Electron Microscopy

In SEM, the surface of the sample is scanned and backscattered electrons and secondary electrons are detected separately. The secondary electrons have a lower energy than the backscattered electrons and originate almost directly from the sample surface. Therefore, secondary electrons are detected by the in-lens detector and depict the topography contrast of the picture. The cause of this is that secondary electrons generated deep in the material are absorbed by the sample leading to surfaces facing the detector to be brighter. While secondary electrons depict the topography of the sample, the material contrast is characterized by the backscattered electrons. The number of backscattered electrons depends on the sample material and increases with the atomic number. Using the energy selection backscatter detector (ESB), a compositional contrast between the different elements of the sample is achieved by detecting the backscattered electrons.[123]

For studying the IOH-NPs, suspensions were finely dispersed on top of a silicon wafer using an ultrasonic nebulizer. The characterization of the inorganic microstructures was performed by sputtering 10 nm of gold, platinum or carbon on top of the glass coverslips with the inorganic microstructures, as well as for the 4D fabricated structures. SEM imaging was conducted with a Zeiss Leo 1530 scanning-electron microscope operated at 10 keV and with a Supra 40 VP (Zeiss, Germany). Moreover, Paul Somer (INT, KIT), Lukas Grünewald and Kristian Kraft (LEM, KIT) performed SEM imaging of photothermal printed semiconductor structures.

3.1.2 Transmission Electron Microscopy

A transmission electron microscope (TEM) is constructed in a similar way to a conventional light microscope. However, it has a resolution that is improved by a factor of 10000. This allows depicting of the lattice planes of crystalline particles by using high-resolution transmission electron microscopy (HRTEM). As an electron source, the same field emissions cathodes that serve as electron source for SEM can be used. The size of the focused area and the image brightness can be changed via condenser lenses to imping the sample as parallel as possible. After the interaction with the sample, the electron beam can be focused and enlarged by objective and projector lenses. Depending on the interaction of the electrons with the sample, they are scattered or penetrate unhindered. For allowing the later process to occur, the sample is required to be thin. In addition, the scattering of the electrons also depends on the proton number of element present. On the one hand, non-scattered electrons are detected in the bright field and displayed as a shadow image of the sample. On the other hand, scattered electrons are detected in the dark field providing a dark background. In HRTEM, the interference of transmitted and scattered electrons is combined to visualize atomic arrangements in the specimen. This information can be used to determine the sample composition. In scanning transmission electron microscopy (STEM), the electron beam is scanned across the sample and electrons that have been deflected strongly are captured by the High Angle Annular Dark Field (HAADF) detectors. Distinct phases within the sample can be differentiated based on their atomic number (*Z*); heavier elements, for instance, scatter electrons more strongly, leading to characteristic *Z*-contrast.[122,123]

HRTEM imaging was performed on an FEI Titan3 80–300 operated at 300 keV on a TVIPS TemCamXF-416 (R) camera by Lukas Grünewald and Kristian Kraft (LEM, KIT).

3.1.3 Energy-Dispersive X-Ray Spectroscopy

The energy of the X-rays originated from the interaction of the electron beam with the sample is element specific. Thus, by detecting the resulting X-rays from the filling of an electron hole caused by inelastic scattering in an inner shell with an electron from an outer, higher-energy shell conclusions about the qualitative and quantitative composition of the sample can be made. Therefore, the spatial distribution and the relative frequency of an element can be determined. In principle energy-dispersive X-ray spectroscopy (EDXS) is possible from the element boron. Lighter elements than boron exhibit low energy X-rays, which are easily absorbed by the window in front of the detector or do not leave the sample. The transition of the relaxing electrons (Figure **10**10) is classified by the shell of the hole (K, L, M,...) and the total transition of shells (one shell = α, two shells = β,...). Furthermore, elastic scattering of the electron beam can occur leading to Bremsstrahlung radiation, which creates a background spectrum.[73,75]

EDXS analysis of photothermal printed structures was performed by Lukas Grünewald (LEM, KIT) with a FEI Tecnai Osiris TEM equipped with ChemiSTEM technology operated at 200 keV was used for STEM-EDXS measurements. EDXS analysis of NP suspensions were conducted with the SEM Supra 40VP (Zeiss, Germany) equipped with a Sapphire Si(Li) PV7715/89 detector (EDAX Genesis, Mahwah, USA) at 30 kV.

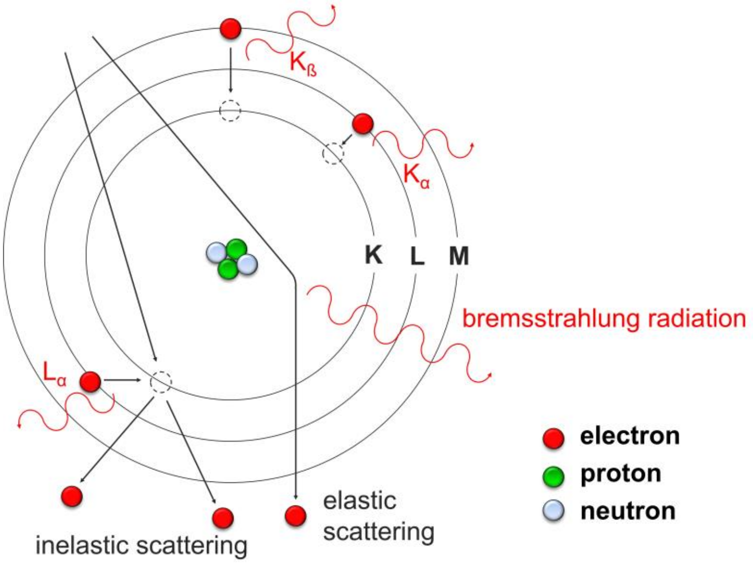

Figure 10. Schematic representation of the formation of X-rays caused by interaction of the incident electron beam with a sample (adapted from ref[126]).

3.2 Dynamic Light Scattering

Dynamic light scattering (DLS) can be utilized to determine the particle distribution in the sub-micron region in various suspensions. Therefore, a NP suspension is irradiated by coherent, monochromatic laser light leading to quasi-elastic scattering (Rayleigh scattering) at each particle. The constructive and destructive interference results in a varying interference pattern at the detector attributed to the Brownian motion of the particles, which continuously change their distance to each other. Measurements of the scattering intensity at time t and after a short time interval $t+\delta t$ results in an autocorrelation, which decreases exponentially over time. The smaller the particles the faster the decrease of the autocorrelation. The diffusion coefficient *D* can be calculated by the decrease of the correlation function and the hydrodynamic radius r_H can be determined with the Stokes-Einstein equation. A prerequisite for the Stokes-Einstein equation are uniform spherical particles and the hydrodynamic radius includes the solvate shell.[127] Thus, the recorded particle distribution can differ from REM results.

$$r_H = \frac{k_B \cdot T}{6 \cdot \pi \cdot \eta \cdot D} \qquad (2.3)$$

r_H = hydrodynamic radius; k_B = Boltzmann constant; T = temperature; η = viscosity; D = diffusion coefficient

The particle size distributions were recorded using a Zetasizer Nano ZS (Malvern Instruments, UK) equipped with a He-Ne laser (λ = 633 nm). The scattering intensity was detected at an angle of 173° in backscattering geometry. For sample preparation, a NP suspension diluted in 2 mL was transferred into a polystyrene cuvette from Sarstedt (Germany) and measured at 20 °C. The Zetasizer software (version 7.10) was used for data evaluation.

3.3 Zeta Potential Measurement

In addition, DLS can be used for determining the zeta potential of a NP suspension, which is an electrical potential for the electrostatic stability of the NPs in their suspension. The colloidal stability of the NPs strongly depends on the surface charge of the NPs. On the one hand, a high surface charge leads to repulsion of particles from each other. This results in an electrostatically stabilized NP suspension. At low surface charge, the NPs exhibit low repulsion for each other; on the other hand, this leads to agglomeration and sedimentation of the NPs. If one of these processes takes place the NPs lose their typical properties related to their extremely high surface area. Thus, this technique was used here to ensure that non-agglomerated, electrostatic stabilized NPs were added to resins for fabricating 4D structures.

In principle, particles in suspension consist of two different layers (Figure 11). There is the inner layer referred to as Stern layer, where the molecules or ions are tightly bonded. The outer layer is diffuse and, thus, the molecules or ions are only weakly bounded and shearable due to friction.[128,129] A zeta potential higher than 30 mV or lower than -30 mV indicates high electrostatic stability.[83]

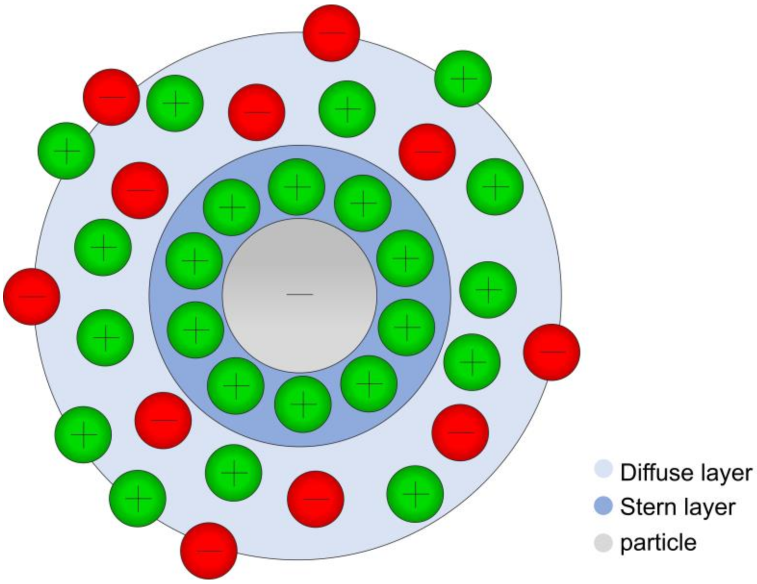

Figure 11. Schematic representation of the different layer of a particle in suspension (adapted from ref[129]).

The zeta-potential can be described using the Smulochowski equation.

$$\zeta = \frac{v \cdot \eta}{\epsilon_0 \cdot \epsilon \cdot \vec{E}} \qquad (2.4)$$

ζ = zeta potential; v = velocity; η = viscosity; ϵ_0 = dielectric constant of vacuum;

ϵ = dielectric constant of sample; $\vec{E}$ = field strength

To measure the zeta potential an outer electrical field is used to enhance the particle motion. Afterwards, a monochromatic laser beam gets split in two and one laser beam gets directed onto the sample where it gets scattered. Followed by interference with the second laser beam, which is used as reference. Due to changes in the interference pattern caused by the particle motion, conclusions about the migration velocity of the particles in the electrical field can be determined and associated with the zeta potential.[80]

The zeta potential was measured using a Zetasizer Nano ZS (Malvern Instruments, UK). The measurements were performed in electrophoresis cuvettes (Malvern Instruments, UK). Furthermore, an MPT-2 autotitrator (Malvern Instruments, UK) was used to perform pH-dependent zeta-potential measurements. For adjusting the pH solutions of 0.1 M HCl, 0.01 M HCl, 0.1 M NaOH, and 0.01 M NaOH were used.

3.4 Photoluminescence Spectroscopy

Luminescence is the emission of a photon after electron transition from a higher state to the ground state. Based on the source for excitation, different types of luminescence can be distinguished such as photoluminescence, bioluminescence or cathodoluminescence. The excitation in photoluminescence occurs due to absorption of a photon. Taking the electronic and vibronic states into account, the entire process can be depicted by inspection of the Jablonski diagram (Figure 1). The possible electron transitions shown in the Jablonski diagram are explained in chapter 2.1 Photochemistry Essentials in more detail. For photoluminescence spectroscopy, the essential process is the emission of light by relaxation of an electron from a higher electronic, vibronic ground state S_1 to the electronic ground state of S_0. This kind of emission is called fluorescence and takes place within 10 ns.[34] In addition, the excitation wavelength is shorter than the emission wavelength, which is known as Stokes shift.[34,35] The setting of a photoluminescence spectrometer consists of a polychromatic light source, excitation- and emission monochromators, sample chamber and detector. The monochromators enable incremental sampling of the wavelength. The detector measures the fluorescence intensity in a 90° angle to the light source to avoid measuring scattered or reflected light. To record an excitation spectrum the emission monochromator is set to one wavelength and the excitation wavelength is scanned. The opposite procedure is applied for the acquisition of an emission spectrum.

Photoluminescence studies were performed with a Flurolog-3 (Horiba Jobin Yvon, France), equipped with a 450 W xenon lamp and two double-grating monochromators (Czerny-Turner monochromators). The detector is a photomultiplier, suitable for measurements in the range between 260 and 850 nm. The program FluorEsscence version 3.5 (Horiba Jobin Yvon, France) was used for evaluation of the recorded data. Fluorescence spectroscopy of 4D structures on glass coverslips were conducted using a Cary Eclipse Fluorescence Spectrophotometer from Agilent Technologies (QUT, Australia).

3.4.1 Fluorescence Microscopy

Fluorescence Microscopy is a type of light microscopy, which enables imaging of structures and cells due to excitation and detection of fluorescence of the present sample. Thus, the sample needs to be either fluorescent by itself, or fluorescence labelled. Furthermore, another basic requirement is the separation of excitation and emission light. Such a setup is composed of a polychromatic light source that emits a light over a broad spectrum onto an excitation filter, which only allows a narrow band of wavelengths to pass through (Figure 12). Subsequently, the beam gets reflected on a dichroic mirror, mounted in a 45° angle to the light source and the sample. The light emitted by the sample is transmitted by the dichroic mirror and before detection it passes an emission filter.[34,35]

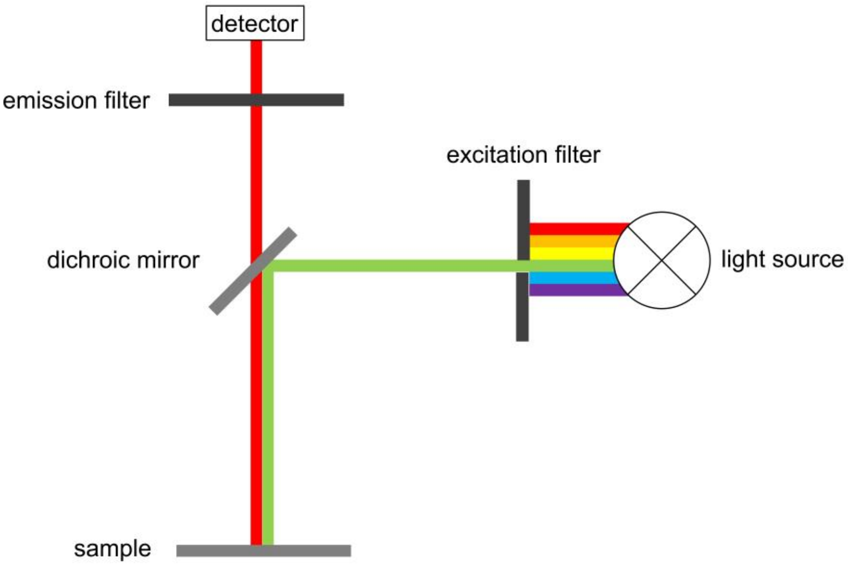

Figure 12. Schematic representation of a fluorescence microscope consisting of a light source, beam splitter, filters and detector (adapted from ref[130]).

3.4.2 Confocal Microscopy

First introduced in the 1950s,[131] confocal microscopy is a type of scanning microscopy such as SEM, which allows collecting fluorescence 3D representations of the sample with high-spatial resolution. Confocal microscopy is often used for making quantitative analysis of cells and tissues or to quantify luminescence intensities of fluorophores.[130] The main difference is that a confocal microscope has a small pinhole in front of the detector to smear out fluorescence occurring outside of the focal point.[131] Thus, fluorescence images collected by confocal microscopy possess reduced background noise compared with widefield fluorescence microscopy. The pinhole is set in a CONjugated FOCAL plane with the sample in the light path of microscope, thus lending this technique its name.[130] Besides that, the setup is composed of a light source, dichroic mirrors and objectives. A simplified confocal microscope setup (Figure 13). In general, various monochromatic lasers operating at wavelengths of 405, 488, 561 and 640 nm are used as light source. The laser beam is focused on an objective and transmitted on a small spot on the sample. The dichroic mirror directs the excitation and emission light. The fluorescence of the sample in this spot returns to the objective and another lens brings it into focus at the pinhole generating optical section smaller than 1 µm.[130] Afterwards, the light is detected by multiple detectors for different wavelengths depending on the wavelength of the emitted light by the sample. To record a two-dimensional (2D) image the focused spot of illumination is scanned over the sample in *x* and *y*-direction. A 3D image referred to as *z*-stack is generated by changing the focus and collecting a series of 2D images.[132,133]

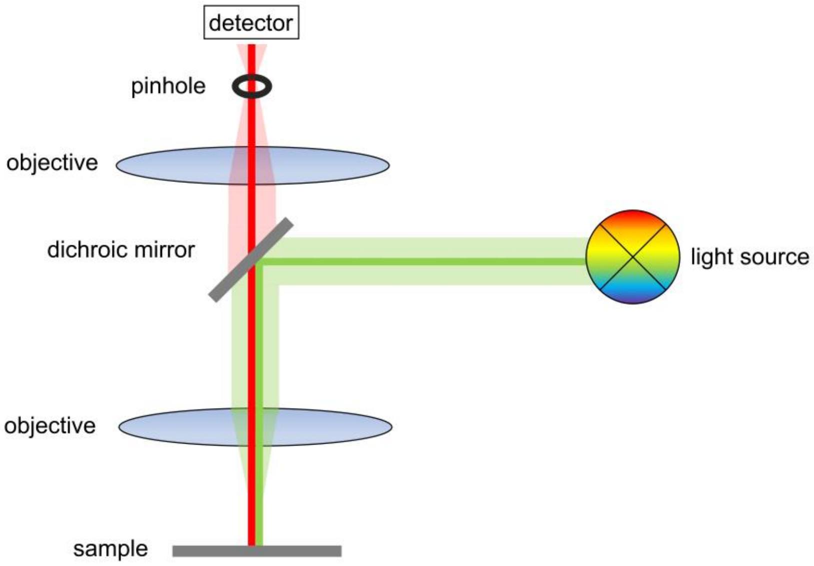

Figure 13. Schematic representation of a simplified confocal microscope consisting of a light source, beam splitter, objectives, pinhole and detector (adapted from ref[130]).

Confocal microscopy was performed using an Evident FluoView4000 Confocal (QUT, Australia). Fluorescence images were recorded for two channels (channel 1 500 – 520 nm and channel 2 600 – 620 nm) with a confocal aperture of 800 µm, an excitation wavelength 488 nm and a laser power of 0.3 %.[16]

3.5 Ultraviolet-Visible Spectroscopy

Ultraviolet-visible (UV-Vis) spectroscopy can be used for identification of chromophores and concentration determination. Furthermore, kinetic studies can be performed by monitoring absorbance changes over time. UV or visible light are used to excite an electron from the ground state to a higher excited state. The energy required for this process can be determined by the Bohr-Einstein equation.

$$E = h \cdot v = \frac{h \cdot c}{\lambda} \qquad (2.5)$$

E = energy; h = Planck constant; v = frequency; c = velocity of light; λ = wavelength

In UV-Vis spectroscopy the intensity difference of the radiation before and after passing a liquid sample or the reflexion of a solid sample is measured. Beer-Lambert's law, introduced in 2.1 Photochemistry Essentials can be used to describe this behavior for low sample concentration in liquid phase. It states that the light passing through a medium is proportional to concentration of the absorbing species, the path length of the sample and the molar extinction coefficient.[134]

UV-Vis spectra were recorded using a UV-2700 spectrometer (Shimadzu, Japan). NP suspensions samples were measured in UV-transparent polystyrene cuvettes against pure solvent as reference. The fabricated 4D composites were directly measured using the polymer without NPs as reference.

3.6 Infrared Spectroscopy

Infrared (IR) spectroscopy is a part of vibrational spectroscopy and is used to measure the absorption of IR radiation by chemical bonds. Functional groups absorb IR radiation leading to a correlation between molecule structure and frequency of absorbed IR radiation. The absorbed energy of IR radiation is characteristic of functional groups. This correlation can be used to identify molecule structures and provides information about bond strengths. IR radiation is electromagnetic radiation with a wavelength (λ) between 1 mm and 1 µm. A prerequisite for the absorption of IR radiation is that the molecules possess a variable dipole moment, which makes the molecule “IR-active”. The irradiation of the sample with IR excites the molecules to vibrate.

A common model of IR spectroscopy is Fourier-transform infrared spectroscopy (FT-IR spectroscopy) enabling rapid spectrum recording. The heart of this model is the so-called Michelson-Interferometer (Figure 14). The polychromatic IR light from the radiation source first strikes a beam splitter (BS), which reflects the light beams toward a fixed and a movable mirror (M1 and M2). When the two beams are recombined after a total length of $2l$, the movable mirror creates a path difference of $2(l+x)$. This results in a total length difference of $2x$, which enables the interference of the beams. Constructive interference takes place when the total length difference is exactly $2x$. The so interferogram recorded by the detector, which represents the intensity as a function of time, is then converted into a frequency-dependent spectrum by means of Fourier transformation (FT).

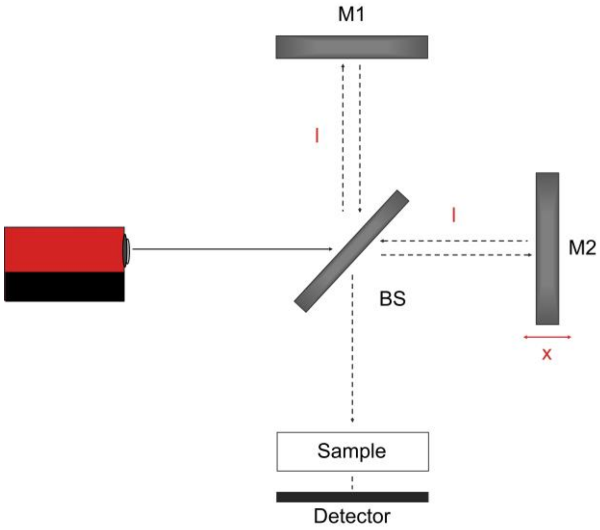

Figure 14. Schematic representation of a Michelson Interferometer (adapted from ref[135]).

The IR spectra were recorded with a Vertex 70 FT-IR spectrometer from Bruker (Germany).

3.7 Additional Analytical Methods

3.7.1 X-Ray Powder Diffraction

X-ray powder diffraction (PXRD) is suitable for material identification of polycrystalline samples. X-rays possess a wavelength of approximately 10^{-10} m, which is comparable to inter lattice distance of atoms. The interaction of monochromatic X-ray radiation with the sample can be described by Bragg's theory. The sample is regarded as a periodically repeating arrangement of lattice points. The incident radiation can be diffracted at each lattice plane, resulting in an interference pattern. If the path difference (δ) of the diffracted X-rays is an integer multiple of the wavelength, constructive interference occurs. This is expressed by Bragg's law:

$$2 \cdot d \cdot sin(\theta) = n \cdot \lambda \qquad (2.6)$$

d = lattice distance; θ = incident angle; $n \cdot \lambda$ = multiple of wavelength

The crystals in a polycrystalline material are statistically oriented and thus, some fulfill Bragg's theory for constructive interference evident as concentric circles at the detector in Debye-Scherrer geometry. The powder diffractogram is recorded by plotting the intensity of the circles against 2Θ.[136]

The powder diffractograms were recorded using a STADI-MP powder diffractometer (STOE & CIE, Germany). The samples were measured in transmission mode on sodium acetate foil (STOE & CIE, Germany). An X-ray tube of the type Long Fine Focus PW2783/00 with a copper anode was employed, producing Cu-K_{α_1} radiation (λ = 154.05 pm). The radiation was monochromatized using a germanium single crystal. The program Win-XPOW (version 3.3) was used for data interpretation.

3.7.2 Elemental Analysis

Elemental analysis (EA) is used to quantify the amount of carbon, hydrogen, nitrogen (N_2) and sulfur contained in the sample. For this purpose, the sample is combusted at 1150°C in an O_2-rich stream and subsequently the obtained gases are passed on to a copper catalyst, which reduces nitrogen oxide to N_2 and sulfur trioxide to sulfur dioxide. The gases get chromatographically separated and quantification of the gases was performed by measurement of the thermal conductivity and IR spectroscopy for SO_2.

EA was performed by Nicole Klaassen (AOC, KIT) using a Vario Micro Cube (Elementar, Germany).

3.7.3 Thermogravimetric Analysis

Thermogravimetric analysis (TGA) is used to determine the composition of sample by measuring the change in weight depending on the temperature. Furthermore, temperature-dependent decomposition and conversion processes can be studied.

TGA was performed using a STA 409C Jupiter (Netzsch, Germany). Approximately 10 mg of dried sample was heated in a corundum crucible from 30-1200°C at a constant heating rate of 5 K min^{-1} in air. The program Proteus Analysis (Netzsch, Germany) was used for evaluation of TGA data.

3.7.4 Time-of-Flight Secondary Ion Mass Spectrometry

Time-of-Flight Secondary Ion Mass Spectrometry (ToF-SIMS) data was acquired by Agnes Morissey (QUT) using an IONTOF M6 instrument (IONTOF GmbH, Münster, Germany) equipped with a reflection time-of-flight analyzer and 30 kV Bi/Mn primary-ion source. A measured target current of 0.6 pA, a primary-ion dose limited to 4×10^{-11} ion cm^{-2}, and a cycle time of 100 µs were selected to provide an accessible mass range up to *m/z* 900. Low energy electron flooding of 21 eV between primary-ion pulses to compensate was used to compensate for the insulating sample. The spectra were recorded in positive polarity at a pressure of 1×10^{-8} mbar, and calibrated using hydrocarbon ion peaks (C^+, CH^+, CH_2^+, $C_2H_2^+$, $C_2H_3^+$, $C_4H_5^+$, $C_5H_5^+$, $C_6H_5^+$, $C_7H_7^+$).[16]

3.7.5 X-Ray Photoelectron Spectroscopy

X-ray photoelectron spectroscopy (XPS) spectra were recorded by Agnes Morissey (QUT) using a Kratos Axis Supra system with a monochromatic Al K_α source (1486.7 eV). A pass energy of 160 and 20 eV with a step size of 0.1 eV were used to record survey spectra and high-resolution core-level spectra, respectively. All XPS data were processed with CasaXPS and calibrated by setting the C *1s* peak to 285.00 eV.[16]

3.7.6 Electron Backscatter Diffraction

Electron backscatter diffraction (EBSD) is a SEM technique used for crystallographic characterization of the sample. Electrons of the incident electron beam are backscattered by the crystal lattice of the sample, leading to Kikuchi diffraction patterns, providing information of the crystal orientation, grain size, texture and phase.

EBSD was carried by Kristian Kraft (LEM, KIT) using a Thermo Scientific Helios G4 FX equipped with a Bruker eFlash HD detector. The pre-cleaned sample is mounted in an effective tilt of 70° and the EBSD patterns were acquired at an electron energy of 20 keV and a nominal electron-beam current of 6.4 nA.[23]

3.8 Composite-Material Fabrication

3.8.1 Stereolithography

SLA was carried out using the Mono LISA printer,[5] which is equipped with an Opotek Opolette 355 OPO laser, producing 7 ns, 20 Hz pulses. Prior to the printing, 0.2 mL of the composite-material ink were deposited on a pre-cleaned 22×22×0.17 mm glass coverslip. For the printing G-code files are imported, which navigate the printing trajectory. The composite-material circles were printed at 390 nm with a laser power of 1.08 mW and laser-writing speed of 0.03 mm s^{-1}. Subsequently, the printed structures were developed with 2-propanol.

The fabrication of multi-materials using SLA was carried out by first using 0.2 mL of the ink without IOH-NPs. The object was developed with 2-propanol and the sample was placed back onto the sample holder. The remaining parts of the multi-material were fabricated using 0.2 mL of the composite-material ink. SLA of the multi-material was conducted at 390 nm with a laser power of 1.08 mW and laser-writing speed of 0.03 mm s^{-1}.[16]

3.8.2 Digital-Light Processing

2D and 3D composite-material fabrication was carried out using a 3D HALOT-ONE CL-60 LCD-Resin printer from Creality equipped with a 405 nm light source.

pH-sensitive composite material

Prior to the printing, 20 mL of composite-material ink were filled into the resin tank. The 3D printing of pH-sensitive composite materials was conducted using the following printing parameters: 0.01 mm, initial exposure 10 s, exposure time 8 s, rising height 5 mm, motor speed 1 mm s^{-1}, light-off delay 10 s and a bottom layer count 7. The 3D objects were developed with 2-propanol.[16]

O_2-sensitive and light-responsive composite materials

12 mL composite-material ink were filled into the resin tank. The printing was carried out using the following printing parameters: layer thickness 0.01 mm, initial exposure 40 s, exposure time 10 s, rising height 5mm, motor speed 1 mm s^{-1}, light-off delay 4 s and a bottom-layer count of 10. Finally, the 2D and 3D printed objects were developed by immersing them in 2-propanol for 10 min to wash off non-solidified material.

3.8.3 Spin-Coating

Pre-cleaned 22×22×0.17 mm glass coverslips were uniformly coated using a spin-coater at a rotation speed of 200 rpm for 5 min. Subsequently, the solidification of the composite-material films was carried out by placed the sample at a distance of 2 cm beneath a λ_{max} = 385 nm LED (SBM-120-UV-F34-L385-22) operated at 12 V and 0.03 A. The LED was cooled to mitigate thermal effects.

3.9 Photothermal Laser Printing

3.9.1 Ink Formulation

500 mg ($Zn(HCO_2)_2$) (3.22 mmol) were dispersed in 10 mL dry DMSO in a crimp cap vial. The suspension was sonicated for 15 min and aged on orbital shaker at 30°C, 400 rpm for 4 h. Subsequently, the suspension was filtered through a 0.20 µm hydrophobic PTFE syringe filter and stored under N_2.[23]

3.9.2 Substrate Preparation

The substrates were fabricated by initially cleaning 22×22×0.17 mm glass coverslips using water and aqueous solutions containing 4 vol-% Deconex OP 146, 2 vol-% Deconex OP 12PA-x, and 2 vol-% Deconex OP 171, respectively. A magnetron sputterer (BOC Edwards, Auto 500) with a power of 200 W and 3.5 SCCM argon inflow was used first deposit Si. Subsequently, the SiO2 layer was sputtered at 100 W and 7.5 SCCM of atmosphere inflow.[23]

3.9.3 Printing Process

The printing was carried out in sandwich mode using Kapton tape (thickness 61 µm) to fix the substrate and glass coverslip. The printing was conducted using a 532 nm

CW laser (Coherent, Verdi-V5) at various laser powers and laser-writing speeds. Subsequently, the samples were developed using dimethyl sulfoxide and 2-isopropanol.[23]

CHAPTER 4: MOTIVATION AND THESIS OUTLINE

The current PhD project focuses on the fabrication of functional composites using a novel concept of fusing responsive IOH-NPs with conventional printing methods, such as SLA and DLP. In addition, the photo-induced fabrication of fully inorganic materials was studied. To date, the most widely used resins have been (meth)acrylate-based organic materials, resulting in a limited property profile.[37,39] On the other hand, there is an critical literature gap concerning adaptive and responsive composite materials and the fabrication of fully inorganic microstructures.

In this thesis, responsive composite materials are prepared by conventional light-driven 3D printing of photopolymer resin in the presence of functional IOH-NPs. This approach opens key avenues for objects offering dynamic responses to external stimuli such as pH, O_2, and light. Furthermore, the precise printing of inorganic matter can be achieved by exploring the potential of photothermally-driven reactions without the need for expensive equipment (e.g., a femtosecond pulsed laser) and post-processing is examined. Finally, the possible fabrication of electronic and optoelectronic devices by printing orthogonal metal- and metal-oxide inks in a step-by-step fashion is explored.

4.1 Research Objectives: Responsive Composite Materials

- Synthesis and characterization of functional IOH-NPs exhibiting adaptivity and responsiveness to external stimuli, for instance, pH, O_2, and light.
- Examination of suitable components for formulation of different composite-material inks.
- Fabrication of responsive composite materials using various light-induced printing techniques.
- Characterization of the prepared composite materials and investigation of their responsiveness and sensitivity to external stimuli.

4.2 Research Objectives: Photothermal Laser-Printing of Inorganic Materials

- Examination of suitable components and preparation of orthogonal inks containing metal salts or complexes.
- Exploration of the potential of photothermal laser-printing to fabricate metal oxides and metal microstructures. Development of a routine to execute the printing process.
- Characterization of the individually fabricated inorganic microstructures.
- Orthogonal fabrication and characterization of electronic devices.

CHAPTER 5: MATERIALS

Compounds	Chemical formula	Purity	Supplier
3,4,9,10-Perylenetetracarboxylic 3,4:9,10-dianhydride	$C_{24}H_8O_6$		abcr
4,4'-Bis(diethylamino) benzophenone	$C_{21}H_{28}N_2O$	99.0 %	Merck
Acetic acid	$C_2H_4O_2$		Merck
Alizarin Red S sodium salt	$NaC_{14}H_7O_7S$		abcr
Ammonia 25 %	H_5NO		Merck
Ammonium chloride	H_4NCl		Merck
Blood serum			Sigma Life Science
Citric acid	$C_6H_8O_7$		Merck
Citric acid, trisodium salt dihydrate	$C_6H_5Na_3O_7 \cdot 2H_2O$	99 %	Acros Organics
Deconex OP 146			Borer Chemie AG
Deconex OP 12PA-x			Borer Chemie AG
Deconex 171			Borer Chemie AG
Dichloro(1,5-cyclooctadiene)platinum(II)	$C_8H_{12}Cl_2Pt$		abcr
Dimethyl sulfoxide (anhydrous)	C_2H_6OS	99.8 %	Acros Organics
Disodium phosphate	HNa_2O_4P		Merck
Ethanol	C_2H_5OH	90 %	Seulberger
Flavin mononucleotide sodium salt	Na(HFMN)	≥ 70 %	Merck
Gadolinium(III) chloride hexahydrate	$GdCl_3 \cdot 6H_2O$	99 %	Merck
Histamine	$C_5H_9N_3$	≥ 97 %	Merck
Hydrochloric acid 32 %	HCl		VWR

Indocyanine green	$C_{43}H_{47}N_2NaO_6S_2$		abcr
Isopropanol	C_3H_8O	≥ 99.9 %	Carl Roth
Lanthanum(III) chloride	$LaCl_3•7H_2O$	99.9 %	Merck
Lithium phenyl-2,4,6-trimethylbenzoylphosphinate	$C_{16}H_{16}LiO_3P$	98 %	TCI
Monosodium phosphate	H_4NaO_5P	98 %	Carl Roth
New indocyanine green	$C_{46}H_{50}ClN_2NaO_6S_2$	Laser grade	SIAL
Nitric acid 65 %	HNO_3		AnalaR NORMAPUR
Silver nitrate	$AgNO_3$	99 %	Merck
Sodium acetate	$C_2H_3NaO_2$	99 %	ACS
Sodium chloride	NaCl		Merck
Sodium dithionite	$Na_2S_2O_4$		VWR
Sodium hydroxide	NaOH		VWR
Sodium thiosulfate	NaS_2O_3	98.5 %	Carl Roth
Thiophene	C_4H_4S	≥ 99 %	Merck
Triphenylphosphine	$(C_6H_5)_3P$	99 %	Merck
Poly(ethylene glycol) diacrylate	$(C_2H_4O)^nC_6H_6O_3$ 700 g mol^{-1}		Merck
Zinc formate	$C_2H_2O_4Zn$	98 %	Thermo Fisher
Zirconyl chloride	$ZrOCl_2•8H_2O$	98 %	Merck

CHAPTER 6: COLOR AND FLUORESCENCE SWITCHABLE 2D AND 3D PRINTED COMPOSITE MATERIALS

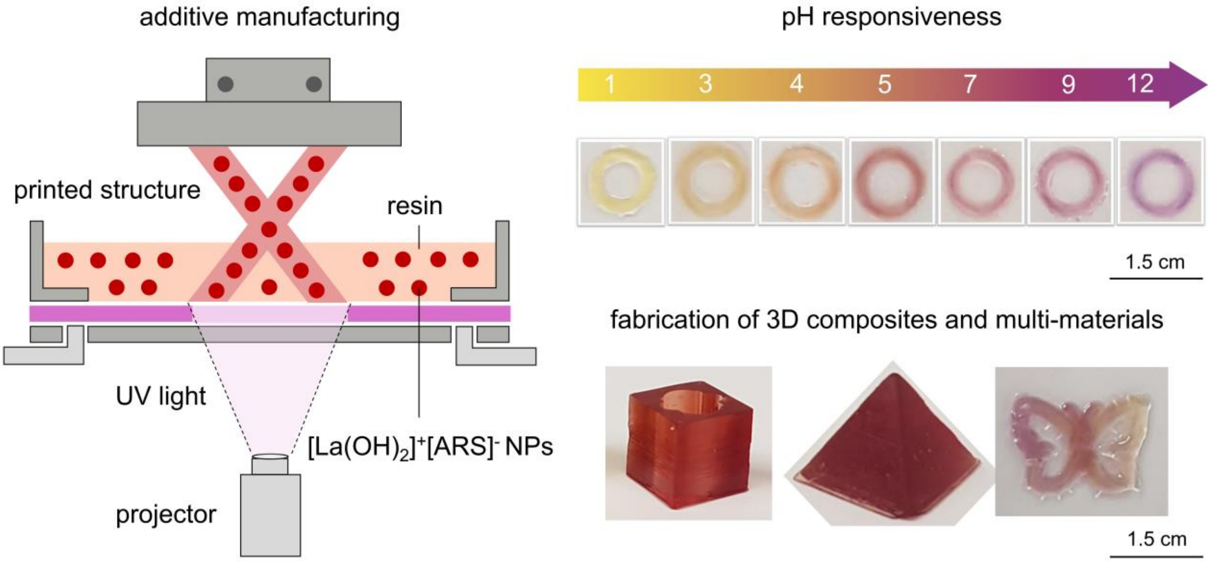

6.1 Introduction

Smart materials with responsiveness and adaptivity to pH changes are used in soft robotics,[137] drug delivery,[138,139] food packaging,[140,141] catalysis,[142] and shape memory applications.[143,144] Furthermore, pH is a fundamental parameter for characterizing biological systems.[145] Some natural polymers, for instance, keratin, and synthetic polymers, such as poly(acrylic acid), show pH-dependent behavior based on reversible protonation and deprotonation of ionizable functional moieties, for example, carboxyl, hydroxyl, and amine groups.[138,146] The molecular transitions lead to physical and chemical changes including swelling,[137–139,142,146] color change[140,141] and shape deformation.[144] Besides using pH-sensitive polymers, pH-insensitive polyacrylamide can be adjusted by introducing small molecules, for example, dansyl moieties, into the polymer chain to achieve pH adaptivity.[143] Dansyl moieties exhibit pH-dependent aggregation and disaggregation.

To enhance the mechanical stability of smart materials, pH-responsive polymers can be copolymerized with other polymers or functional molecules.[147–149] In addition, composite materials are an interesting class for pH-responsive smart materials due to their enhanced mechanical strength. They can be fabricated by embedding pH-sensitive particles into a polymer matrix. For instance, curcumin has been immobilized in sago starch leading to a reversible pH-dependent color change from yellow to red due to the keto-enol tautomerism of curcumin.[141]

Furthermore, composite materials serve as platform for multi-responsive smart materials. For example, the fabrication of multi-responsive composite materials composed of a hydrogel bilayer of pH-sensitive poly(2-hydroxyethyl methacrylate) and magnetic field-responsive iron (II/III) oxide embedded into poly(ethylene glycol) diacrylate.[137] The resulting smart materials are capable of pH-dependent drug release and magnetic field-dependent motion. Recently, smart materials exhibiting pH responsiveness have gained more attention due to their wide variety of applications.[150] Despite the growing interest several challenges such as precise control over pH responsiveness, limited mechanical stability, chemical stability, reproducibility and scalability remain unaddressed. Due to these challenges, the current chapter focuses on the light-driven 3D fabrication of pH-dependent composite materials with various shapes and geometries, which reversibly alter their luminescence and color and enable multi-material printing. The composite material is composed of pH-dependent IOH-NPs embedded into a polymer matrix. Possible applications for pH-monitoring include water quality control, food manufacturing, and various industrial processes. The next section focuses on the synthesis of Alizarin Red S (ARS)-based IOH-NPs, which exhibit dual pH-sensitive colorimetric and fluorometric properties. Subsequently, the IOH-NPs are embedded into a polymer matrix, serving as the pH-responsive component employed in 3D fabrication.

6.2 Inorganic-Organic Hybrid Nanoparticles

ARS is an organic dye with an anthraquinone core. It is commonly used as a staining agent and a histochemical reagent in osteogenesis assays.[151,152] In addition, ARS is a pH indicator, altering its color from yellow at pH 3.5 to red at pH 6.5 and violet at pH 10.[145] This color change is caused by the protonation/deprotonation of the hydroxyl moieties attached to the anthraquinone core (Figure 15).

In addition, ARS exhibits luminescence, which undergoes a pH-dependent wavelength shift. Fluorometric analysis of the pH offers high sensitivity combined with good spatiotemporal resolution.[153]

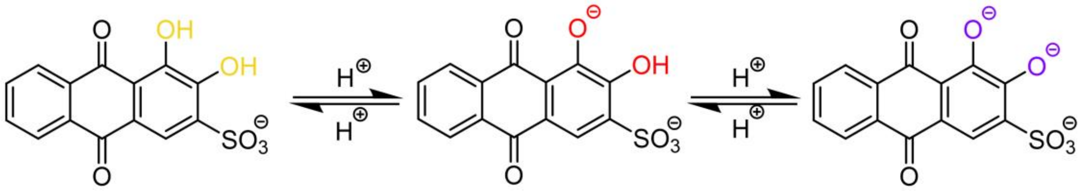

Figure 15. Reversible two proton exchange of ARS.

In combination with, for instance, La^{3+}, ARS can be used to form IOH-NPs due to the poor solubility of lanthanum sulfonate in water.[17,19] IOH-NPs exhibit enhanced photostability compared to the free organic dye.[17] Recently, ARS-based IOH-NPs were utilized for optical imaging in tumor diagnosis offering high sensitivity combined with good spatiotemporal resolution.[19] In addition, the ARS-based IOH-NPs can readily be redispersed in a photoresin and the solidified material exhibits significantly reduced leaching compared to the use of the free organic dye embedded into a polymer network.

The following section focuses on the synthesis and characterization of $[La(OH)_2]^+[ARS]^-$ IOH-NPs to achieve a detailed insights of the functionality of the IOH-NPs.

Synthesis

The $[La(OH)_2]^+[ARS]^-$ IOH-NPs were prepared as previously described in the literature.[19] Initially, 36.0 mg Na(ARS) (0.1 mmol, 1.0 eq., 0.002 mmol mL^{-1}) were dissolved in 50 mL water. Instantaneous formation of IOH-NPs occurred upon injection of 33.0 mg of $LaCl_3 \cdot 7H_2O$ in 0.5 mL water (0.09 mmol, 0.9 eq., 0.18 mmol mL^{-1}) while vigorously stirring. The injection caused the solution to become cloudy, and the color shifted from bright orange to red (Figure 16). Subsequently, the suspension was centrifuged three times (20.000 rpm, 15 min, 4 °C), and the final IOH-NPs were obtained by redispersing the precipitate in water.

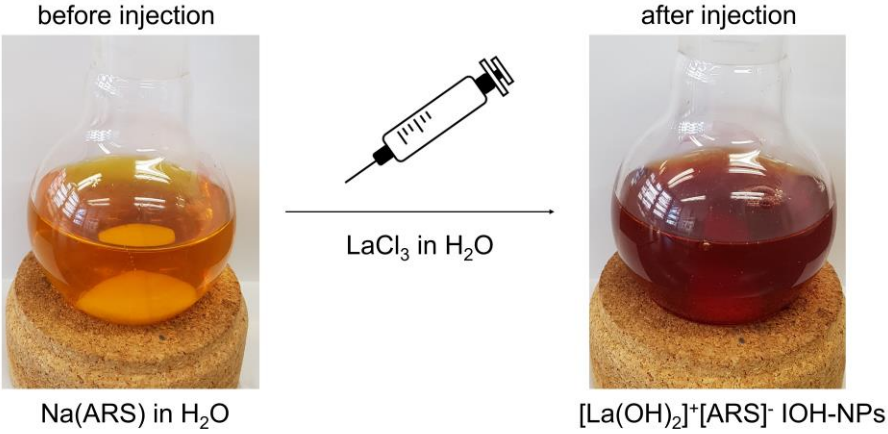

Figure 16. Synthesis of pH-sensitive $[La(OH)_2]^+[ARS]^-$ IOH-NPs starting from Na(ARS) by injection of $LaCl_3$.

After the synthesis of the IOH-NPs their particle size, composition, and optical properties were investigated utilizing various analytical techniques. Studying the pH-dependent colorimetric and fluorometric properties of the IOH-NPs is essential to employ them in pH-responsive composite materials and to later tune the pH sensitivity of the composites.

Characterization

After the synthesis of the $[La(OH)_2]^+[ARS]^-$ IOH-NPs, analysis was conducted utilizing both the IOH-NP suspensions and the air-dried IOH-NPs. Size and morphology of the $[La(OH)_2]^+[ARS]^-$ IOH-NPs were determined by DLS and SEM analysis (Figure 17). Both analytical methods confirm the successful synthesis of nanosized material. DLS measurements (Figure 17a) of the IOH-NPs reveal a broad size distribution in water with a mean hydrodynamic diameter of 47±8 nm. SEM analysis of 100 IOH-NPs confirms the synthesis of spherical IOH-NPs with a size of 42±7 nm. The particle size determined by SEM analysis is in good agreement with the literature.[19] The slight difference in the size of the IOH-NPs originates from the hydration shell surrounding the IOH-NPs during DLS analysis. Thus, a larger diameter for the DLS analysis compared to the SEM analysis is to be expected.

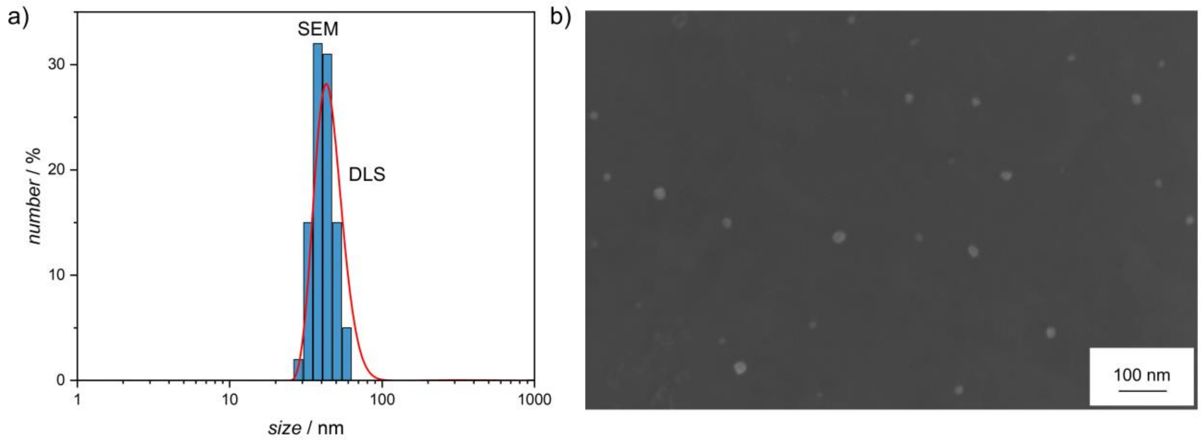

Figure 17. Size and morphology of $[La(OH)_2]^+[ARS]^-$ IOH-NPs. **a)** Size distribution determined by DLS (red) and by counting 100 individual NPs from SEM images (blue). **b)** SEM image of $[La(OH)_2]^+[ARS]^-$ IOH-NPs.

The colloidal stability of the $[La(OH)_2]^+[ARS]^-$ IOH-NPs was investigated by measuring the zeta potential at different pH values. Stabilization of the IOH-NPs originates from their inherent surface charge, which is quantified by the zeta potential. A zeta potential of ≤ -30 mV typically indicates that the IOH-NPs are colloidally stable.[128] According to zeta-potential measurements (Figure 18), the IOH-NPs are stable from pH 4-9 with a zeta potential < -30 mV.

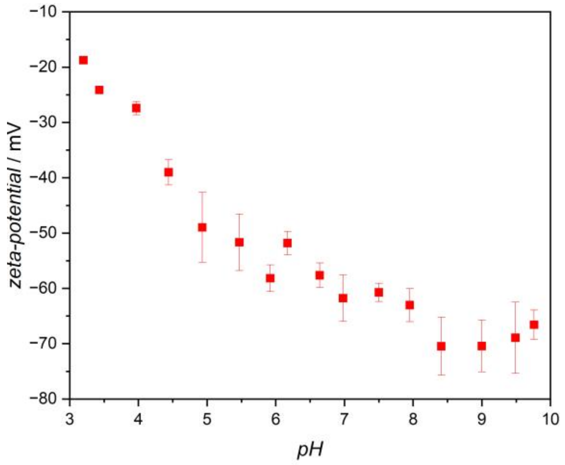

Figure 18. Zeta potential of $[La(OH)_2]^+[ARS]^-$ IOH-NPs at different pH values.

The composition of the $[La(OH)_2]^+[ARS]^-$ IOH-NPs was determined by FT-IR spectroscopy, TGA, PXRD, and EA. A comparison between the FT-IR spectrum of the

IOH-NPs with the free dye reveals close resemblance (Figure 19). In both FT-IR spectra the stretching vibrations of the hydroxyl moieties at $\tilde{\nu}$(O-H): 3600-3000 cm^{-1}, as well as $\tilde{\nu}$(C–H): 2915 and 2850 cm^{-1}, attributed to the aryl-H vibration were observed. In addition, the stretching vibrations at $\tilde{\nu}$(Ar-C=O): 1700-1600 cm^{-1}, $\tilde{\nu}$(Ar-C=C): 1590 cm^{-1}, and $\tilde{\nu}$(Ar-C-O): 1260 cm^{-1} are attributed to the anthraquinone core. The stretching vibration $\tilde{\nu}$(SO_3): 1190-1100 cm^{-1} was observed.[154]

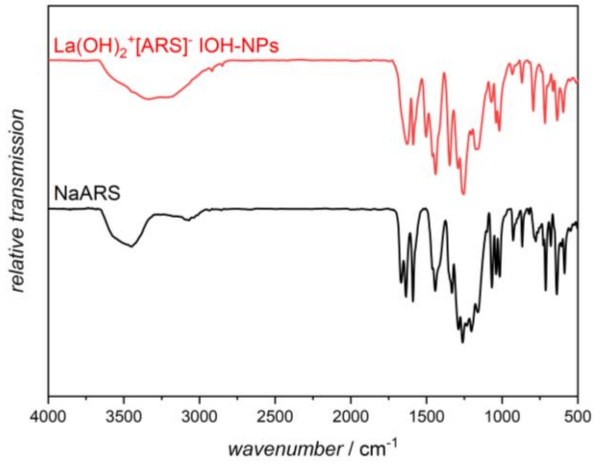

Figure 19. Determination of the composition of $[La(OH)_2]^+[ARS]^-$ IOH-NPs by FT-IR spectroscopy of IOH-NPs (red) and Na(ARS) (black).

TGA of the $[La(OH)_2]^+[ARS]^-$ IOH-NPs (Figure 20a) shows that the decomposition of the IOH-NPs takes place in three steps. The first decomposition step with a mass loss of 14.8 wt-% is completed at approximately 220°C. This mass loss is attributed to the evaporation of residual water, which was adsorbed on the NP surface due to their aqueous synthesis. Subsequently, the decomposition of the organic components between 215°C and 700°C into CO_2, N_2, and H_2O, with a mass loss of 54.2 wt-%, was observed. The last decomposition observed at 700 - 1200 °C, with a mass loss of 11.7 wt-%, can be assigned to loss of sulfate and a possible conversion of lanthanum sulphate $La_2(SO_4)_3$ into lanthanum oxysulfate $(LaO)_2SO_4$. Subsequently, the TGA residue (19.3 wt-%) was examined by PXRD (Figure 20b) to investigate the formation of $(LaO)_2SO_4$. The reflections observed for the sample confirm the presence of $(LaO)_2SO_4$.

The decomposition of the IOH-NPs can be described by the following equation:

$$2\ [La(OH)_2]^+[C_{14}H_7O_7S]^- + 27.5\ O_2 \rightarrow La_2O_2(SO_4) + 28\ CO_2 + 9\ H_2O + SO_2$$

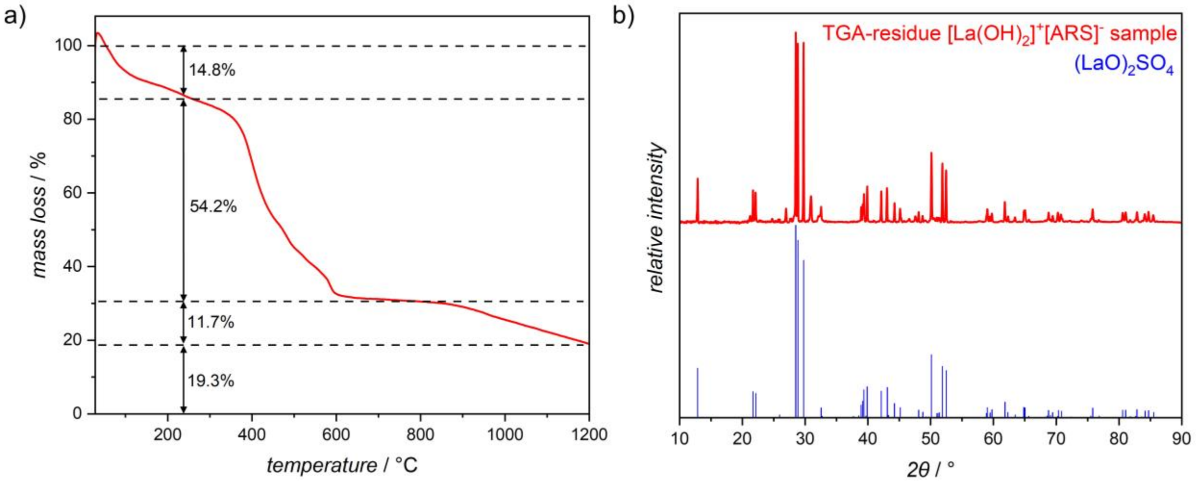

Figure 20. Determination of the composition of $[La(OH)_2]^+[ARS]^-$ IOH-NPs. **a)** TGA spectrum for the IOH-NP combustion. b) PXRD of TGA residue (red) and $(LaO)_2SO_4$ reference (blue).

The organic constituents present in the IOH-NPs were quantified by EA and corrected for the contend of adsorbed water of 14.8 wt-% determined by TGA. The results of the EA analysis are in good agreement with the in theoretically calculated amounts for C, H, and S present in the IOH-NPs (Table 1). Altogether, a ratio of 1:1 for inorganic cation and organic anion in the IOH-NPs, as well as the presence of ARS, were confirmed.

Table 1. EA and TGA of $[La(OH)_2]^+[ARS]^-$ IOH-NPs compared to the expected calculated values.

	C [wt-%]	H [wt-%]	S [wt-%]	Mass loss [wt-%]
Measurement	30.5	2.8	4.6	65.9
Corrected (-14.8 wt-% water)	35.7	1.4	5.4	60.0
Calculated	34.2	1.8	6.5	59.5

The optical properties of the $[La(OH)_2]^+[ARS]^-$ IOH-NPs were investigated by UV-Vis and fluorescence spectroscopy (Figure 21). A color change from yellow-red-violet was observed for the addition of acid or base to the IOH-NP suspension (Figure 21a), which is analogous to the free dye. Furthermore, depending on the pH, the IOH-NPs altered their absorption with maximum at 420 nm for pH < 5 and at 530 nm for pH > 5 (Figure **21**b). Fluorescence spectroscopy revealed that the IOH-NPs exhibit pH-sensitive luminescence upon excitation at 478 nm (Figure 21c). At acidic pH ≤ 4.5, a red shift of about 50 nm takes place, leading to yellow-orange luminescence (560-610 nm) while at pH 5-9 a green emission of 510 nm was observed. The investigation of the optical properties of the IOH-NPs highlights their potential as components for pH-sensitive materials.

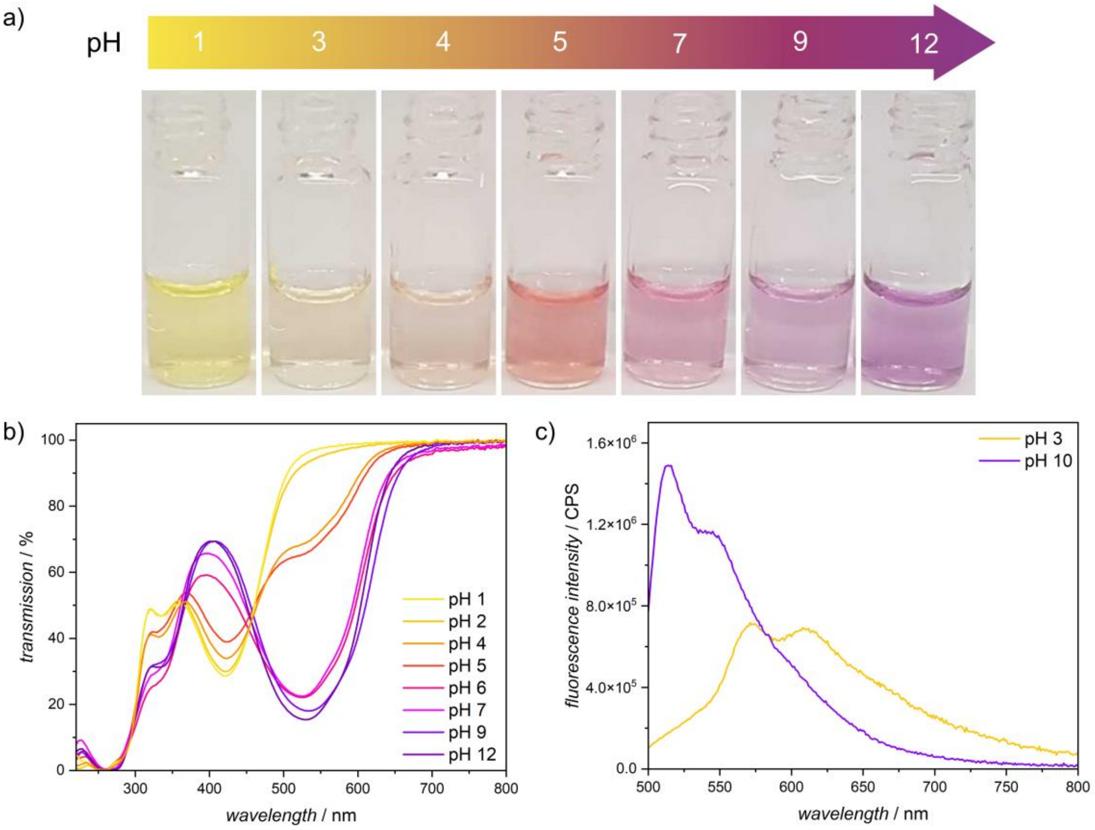

Figure 21. Investigation of the optical properties of the $[La(OH)_2]^+[ARS]^-$ IOH-NPs. **a)** pH-sensitive color change of the IOH-NP suspension. **b)** UV-Vis spectra of the IOH-NP suspension at different pH. values **c)** Fluorescence spectra of the IOH-NP suspension for an excitation at 478 nm at different pH values.

In summary, for the as prepared $[La(OH)_2]^+[ARS]^-$ IOH-NPs, a similar size, morphology and the same composition and pH-dependent optical properties were observed, as described in the literature.[19] Next, to validating the successful synthesis of $[La(OH)_2]^+[ARS]^-$ IOH-NPs and understanding their pH-sensitive optical properties, the incorporation of the IOH-NPs in polymer matrices was explored. Embedding the IOH-NPs in a polymer matrix improves their chemical, physical and photostability.

6.3 Composite-Material Fabrication

Composite-Material Ink Formulation

Commonly used photoresins for 3D printing are (meth)acrylate-based compounds.[37,39] This limited diversity in photoresins restricts the property profiles of the fabricated material. Thus, embedding, for instance, IOH-NPs in a polymer matrix expands the material properties and enables the use of the composite in new applications (e.g., sensing). Composites possess enhanced properties compared to their individual components.[150] For instance, the embedded IOH-NPs exhibit responsiveness to external stimuli such as pH or O_2, whereas the polymer matrix leads to enhanced chemical, physical and photostability.[155,156] Although composites exhibit enhanced properties, the fabrication of composite materials by 3D printing poses noteworthy challenges. First, NPs tend to agglomerate in photoresins and cause light scattering or absorption. These interactions affect the light penetration depth, ultimately hindering the printing process. In addition, the dispersed NPs result in an increase in the ink viscosity, which can impair the printing process. During fabrication the NPs can undergo photodegradation leading to loss of their functionality. To mitigate these challenges and to fabricate a pH-sensitive composite material various photoresins were combined with $[La(OH)_2]^+[ARS]^-$ IOH-NPs. Agglomeration and sedimentation of the IOH-NPs was observed in 1,6 hexanediol diacrylate, poly(ethylene glycol) diacrylate M_n 250 and 575. In particular, sedimentation reduces the content of IOH-NPs in the composite material, lowering its responsiveness. The IOH-NPs exhibit high colloidal stability in water, and thus more polar acrylates were assessed. Stabile suspensions were prepared by redispersing the IOH-NPs in poly(ethylene glycol) diacrylate M_n 700 (PEGDA700) and PETA. The latter resulted in a rigid polymer matrix enabling limited hydrogen diffusion for pH sensing due to high number of crosslinks. Thus, PEGDA700 was used as monomer due to the high compatibility with water and for the preparation of a flexible polymer network, enabling rapid hydrogen diffusion. Next, different photoinitiators were examined based on their autofluorescence. The $[La(OH)_2]^+[ARS]^-$ IOH-NPs exhibit pH-dependent luminescence in the range of 500-700 nm. To ensure high sensitivity and easy read-out of the pH-sensitive composite material, the luminescence of the IOH-NPs should not overlap with the autofluorescence of the photoinitiator. Furthermore, the photoinitiator must have a distinct absorption from that of the IOH-NPs (absorption maximum: $pH \leq 5$ at 420 nm, $pH > 5$ at 530 nm) to avoid an internal filter effect and photodegradation during fabrication. These criteria are met by 4,4'-bis(diethylamino)benzophenone (DEABP), a UV-active photoinitiator with an absorption maximum at 365 nm and an emission maximum 400 nm.[157]

The fully organic resin was prepared by dissolving 20.0 mg of DEABP (0.06 mmol) in 1.0 g PEGDA700. The composite-material ink was synthesized by first dispersing different amounts of IOH-NPs in 200 µL water upon sonification for 10 min. Subsequently, the obtained IOH-NP suspensions were mixed with the organic resin and vigorously stirred overnight. SLA was carried out using an ink with a 4:1 monomer-to-water ratio. For DLP-based 3D printing, 20 mL of composite-material ink were prepared, and the water was removed under vacuum (60 °C, 10 mbar) to ensure better adhesion to the printing platform.

Subsequently, the optimized composite-material inks were used to fabricate functional 2D and 3D composite-material structures using SLA and DLP, described in the next section.

SLA of Composite Materials

In advance of the laser lithography, the photochemical interactions between the individual components were examined. Initially, the photostability of the IOH-NPs was examined to rule out IOH-NPs photodegradation without the presence of the monomer or photoinitiator. The IOH-NPs were constantly irradiated at 260 nm for 12 h while recording UV-Vis spectra (Figure 22a), monitoring the IOH-NPs absorbance at 528 nm. After 12 h, no photobleaching was observed. Next, the interaction of the IOH-NPs with photogenerated radicals was studied by irradiating a $[La(OH)_2]^+[ARS]^-$ suspension containing 1.0 wt% DEABP with a 385 nm LED (SBM-120-UV-F34-L385-22) for 10 min (Figure 22b). For reaction between IOH-NPs and radicals photodegradation and photobleaching of IOH-NPs can occur. These processes result in a loss of the dye content, decreasing the pH responsiveness and sensitivity. No photobleaching was observed after 10 min of irradiation, indicating no reactivity between IOH-NPs and the photogenerated radicals occurred.

Subsequently, the IOH-NPs were mixed with PEGDA700 and irradiated at 385 nm to examine if the IOH-NPs degrade or initiate polymerization under printing conditions. These interactions reduce the dye content and decrease pH responsiveness and sensitivity. The viscosity before and after 10 min light irradiation remained unchanged, suggesting no polymerization took place. A control experiment with a sample containing 1.0 wt-% DEABP in PEGDA700 solidified completely within 2 min. Overall, the IOH-NPs exhibited no reactivity toward either the photoinitiator or the monomer, indicating their chemical stability and compatibility for 3D printing. In addition, the photoinitiator enables rapid solidification of PEGDA700 in the range of 365-405 nm.

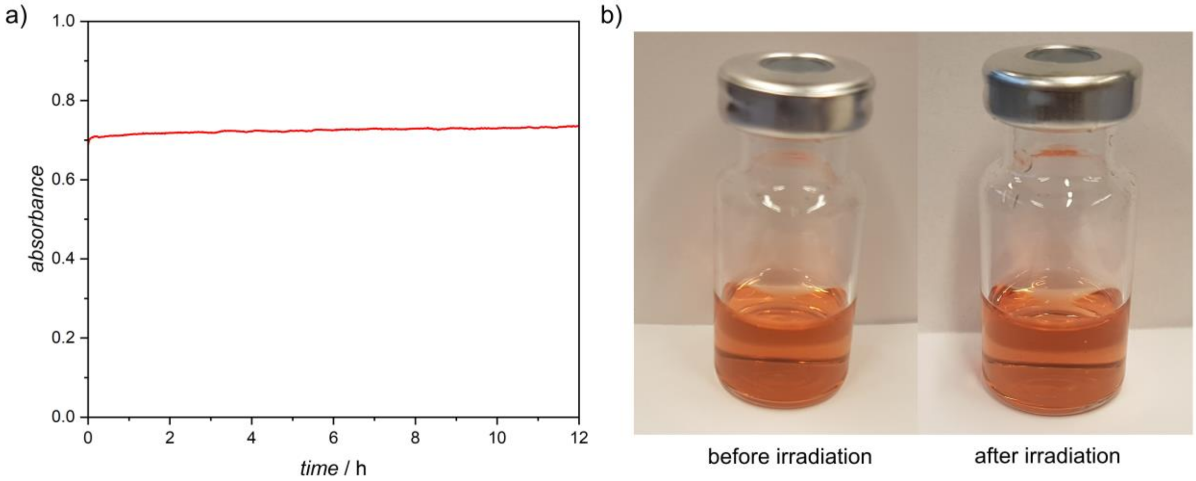

Figure 22. Assessment of the IOH-NP photostability: **a)** Photostability examination of the IOH-NPs at an absorption wavelength of 528 nm upon constant irradiation of the IOH-NPs at their absorption maximum (260 nm wavelength) for 12 h. **b)** Irradiation of the IOH-NPs in the presence of the photoinitiator using a 385 nm-emitting LED (SBM-120-UV-F34-L385-22) for 10 min.

3D fabrication of the pH-responsive composite material was carried out with a custom-designed SLA printer operating at 390 nm (1.08 mW, 0.03 mm s^{-1}).[5] Prior to fabrication, 0.2 mL of composite-material ink was drop-cast on a pre-cleaned glass coverslip. By moving the stage relatively in *x* and *y* directions, composite-material circles were fabricated. Initially, the effect of the IOH-NP concentration on the pH responsiveness (Figure 23) was studied using four different concentrations (i.e., 0.52, 1.08, 1.83, 2.74 g L^{-1}). The fabricated composite-material circles were immersed in hydrochloric acid and sodium hydroxide at pH 1 and 12 for 1 min and their pH-sensitive colorimetric response, compared with the color subsequent to fabrication, was examined after drying using a tissue. The pH responsiveness and sensitivity depend on the IOH-NP concentration. At too low NP concentration no pH responsiveness is expected, while at too high concentration the IOH-NPs are prone to agglomeration. The following color transition are expected: after printing red → pH 1 yellow → pH 12 violet. For the IOH-NP concentration of 0.52 g L^{-1} no color change was observed.

Furthermore, at a NP concentration of 1.08 g L^{-1} a pH-dependent color change started to become visible. However, at pH 12 the color of the composite material was red instead of violet, indicating low pH responsiveness and sensitivity. The expected color change was observed for the NP concentrations of 1.83 and 2.74 g L^{-1} with the later exhibiting deeper colors and thus, a more pronounced responsiveness. The rapid color transitions after 1 min of immersing the composites in solutions at pH 1 and 12 are related to the lose polymer network composed of solidified PEGDA700. Subsequently, the limit of IOH-NPs possible in the composite-material ink was assessed. At concentrations exceeding 3.7 g L^{-1}, agglomeration of the IOH-NPs was observed. All further studies were conducted using composite materials containing 3.7 g L^{-1} IOH-NPs due to increased sensitivity and responsiveness.

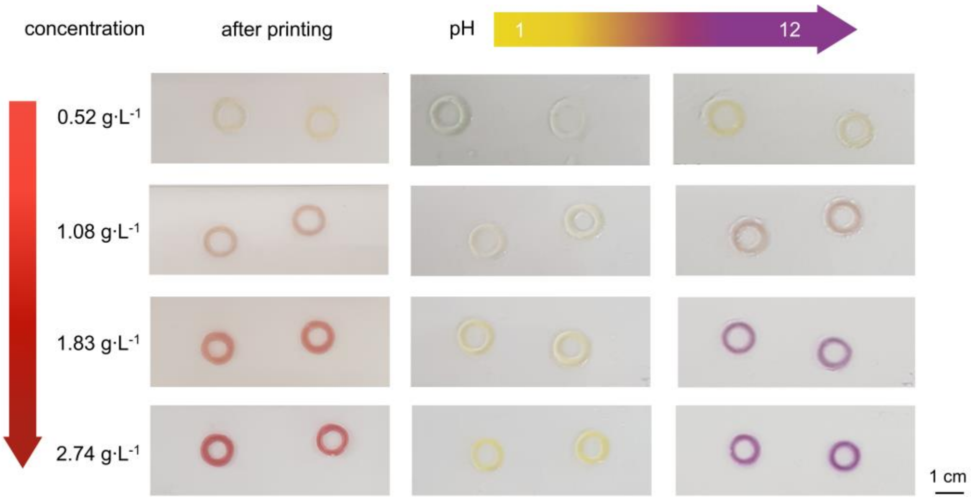

Figure 23. Influence of the $[La(OH)_2]^+[ARS]^-$ IOH-NP concentration on the pH-sensitive colorimetric properties. Composite materials containing IOH-NP concentrations of 0.52, 1.08, 1.83, 2.74 g L^{-1} were assessed after fabrication, and at pH 1 and 12.

Next, the pH-dependent optical properties of the composite material were studied in more detail using finer pH increments, analogous to those used in the evaluation of the colorimetric properties of the IOH-NP suspension. The colorimetric changes of the IOH-NP suspension and the composite materials are illustrated in Figure 24 for pH values ranging from 1 to 12. The buffer solutions are listed in Table 2. To investigate the color changes of the composite material, an SLA-printed composite circle was immersed in different buffer solutions for a duration of 1 min and images were taken. The pH-dependent color changes observed for the composite materials exhibit a close resemblance to those of the IOH-NP suspension. This further indicates that the incorporation of IOH-NPs into the polymer matrix induces pH responsiveness. Subsequently, the pH-dependent luminescence of the composite material was investigated by fluorescence spectroscopy. The composite material was immersed in a pH buffer solution, dried with a lint-free laboratory wipes and afterwards an emission spectrum at an excitation wavelength of 478 nm was collected. The results (Figure **24**b) show that the composite material shows green emission at 520 nm for pH 8-12. In addition, a luminescence red shift of 30 nm was observed at pH 5, and orange emission at 575 – 610 nm is detected at pH 1-3. This results in a total red shift of about 55 nm, which is in excellent agreement with the 50 nm-luminescence shift of the IOH-NP suspension.

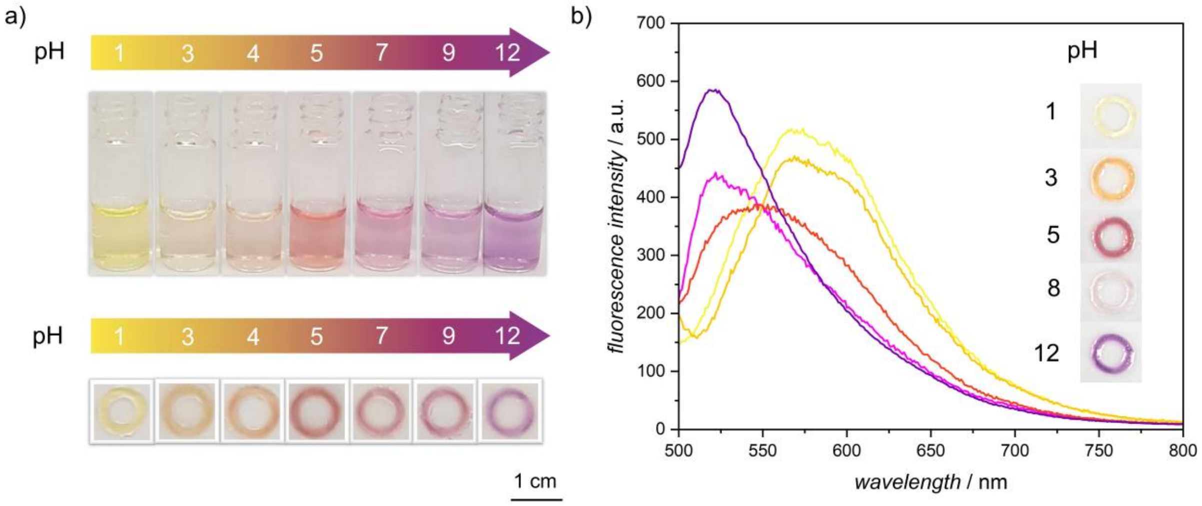

Figure 24. Evaluation of the pH-dependent optical properties of the composite material: **a)** pH-dependent color change of $[La(OH)_2]^+[ARS]^-$ IOH-NP suspension and SLA-printed composite

material. **b)** pH-dependent fluorescence changes of SLA-printed composite material recorded for an excitation wavelength of 478 nm.

Table 2. List of pH buffer solutions employed to change the pH of the composite material.

pH	solution
1	1M hydrochloric acid
3	citric acid/ citrate
4	citric acid/ citrate
5	acetic acid/ acetate
7	monosodium phosphate/ disodium phosphate
8	ammonium/ ammonia
9	ammonium/ ammonia
12	0.1M sodium hydroxide

As a next step, the repeatability of the switching (Figure 25) between pH 1 and 10 was investigated using fluorescence spectroscopy, taking images of the tissue-dried composite material after immersing for 1 min in the relevant pH solution. For the fluorescence spectra recorded with an excitation wavelength of 478 nm, the same red shift of the luminescence was observed as described above. After three cycles of alternating between pH 1 and 10, the luminescence shift remained constant. In addition, a decline of the luminescence intensity over the three cycles can occur due to a leaching of the IOH-NPs. A small decrease in the luminescence intensity for the third cycle at pH 1 was observed, which thereafter, showed full recovery of the luminescence intensity at pH 10. This suggests that an error during the measurement may have occurred, for instance, composite-material misplacement. Thus, this indicates that the IOH-NPs are firmly embedded into the polymer matrix. The pH-dependent color change of the composite for three cycles between pH 1 and 10 was examined. The composite material shows rapid switching between pH 1 yellow and pH 10 violet for the three cycles, indicating fast pH-response and high sensitivity. No coloring of the pH solutions was evident, which further validates the absence of IOH-NP leaching.

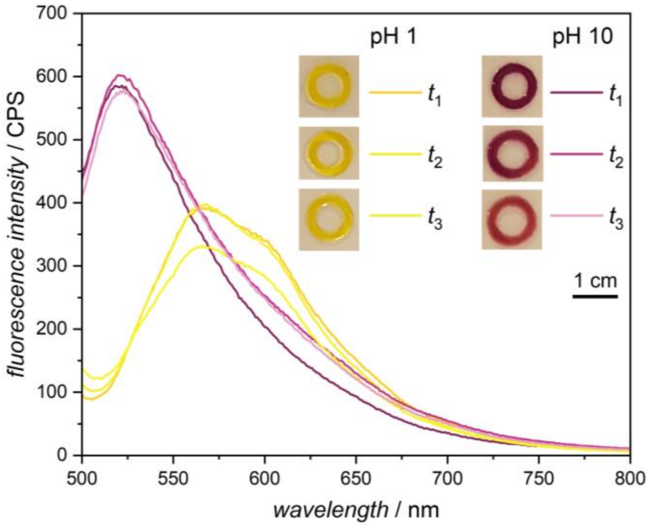

Figure 25. Fluorescence spectra acquired to test the repeatability of switching between pH 1 and 10 in three cycles and collected for an excitation wavelength of 487 nm. Images for pH-dependent color change are added for better visualization.

The pH-dependent luminescence was further studied by alternating the pH between 9 → 3 → 9 using confocal microscopy. Fluorescence images were recorded for two distinct channels. Channel 1 500-520 nm (blue) and channel 2 600-620 nm (red) use a laser operating at 488 nm. Under basic conditions, a luminescence maximum in channel 1 was expected, whereas under acidic conditions, the luminescence maximum should be shifted towards channel 2. Thus, especially under acidic conditions, channel 1 should not exhibit an intense luminescence signal. The fluorescence images (Figure **26**) show that in the beginning of the experiment intense luminescence was observed at pH 9 for channel 1. By lowering the pH to 3, the luminescence intensity decreased. By switching back to pH 9, the intense luminescence was restored. A contrary behavior was observed for the luminescence acquired in channel 2. Here, the highest fluorescence intensity in channel 2 was observed at pH 3. These observations are consistent with the expected behavior. In addition, channels 1 and 2 were merged for better visualization of the luminescence shift. Under basic conditions, a violet color was expected for the combination of channel 1 blue and channel 2 red. However, at pH 3 the color of the merged channels should appear red due to reduced fluorescence intensity in the range of 500-520 nm. In fact, the combination of channel 1 and 2 appears violet and red under basic and acidic conditions, respectively.

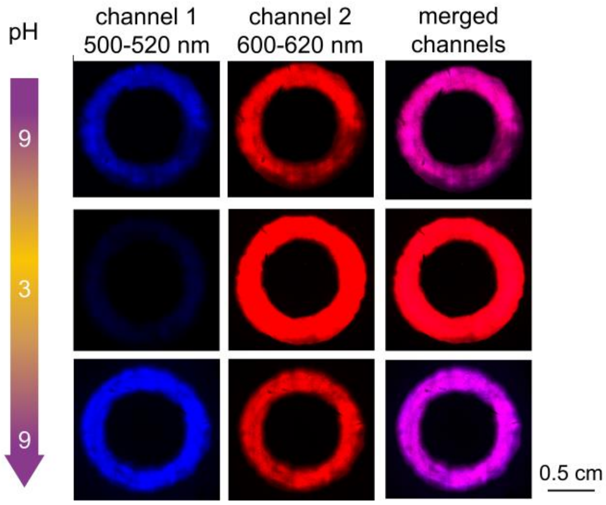

Figure 26. Fluorescence images acquired for two separate channels by confocal microscopy for 488 nm excitation. Channel 1 500-520 nm and channel 2 were selected to detect the maximum fluorescence under basic and acidic conditions, respectively. The merged channels are shown to highlight the red shift of the luminescence.

Subsequent to the investigations of the pH-dependent optical properties, the presence of IOH-NPs embedded within the composite materials was validated. The pH-dependent color change as well as the luminescence shift indicate the presence of the IOH-NPs. For further validation of the composite-material composition focused-ion beam (FIB) cutting was performed and the cross-section was studied by SEM and EDXS analysis. The experiment was carried out at QUT by Konstantin Faershteyn. SEM and EDXS analysis (Figure 27) exhibit the presence of statistically distributed agglomerated IOH-NPs in the polymer matrix. The agglomeration of the IOH-NPs is either attributed to the optical forces or the locally generated heat during SLA.

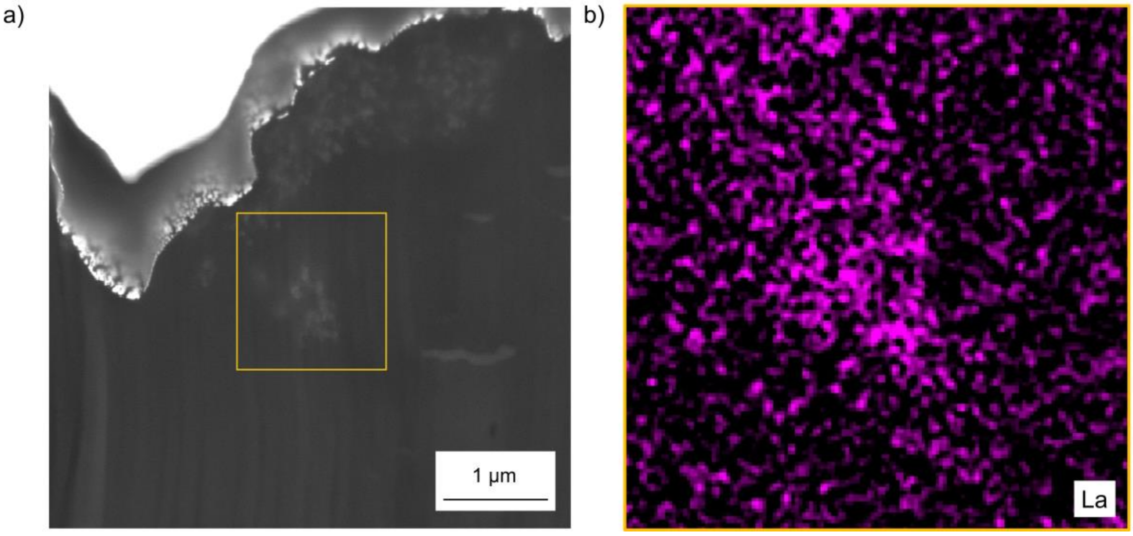

Figure 27. Characterization of the IOH-NPs within the composite material: **a)** SEM image of composite-material cross-section created by FIB cutting. **b)** EDXS map of lanthanum performed on the orange inset shown in a).

Likewise, XPS and ToF-SIMS were carried out by Dr. Agnes Morrissey (QUT) to evaluate the composite-material composition (Figure 28). XPS analysis showed a strong peak for La *3d* at a binding energy of 834 eV. Peaks for La *4p*, *4d* and *5p* were not detected due to the high carbon content of the polymer matrix surrounding the IOH-NPs. Finally, the ToF-SIMS measurements exhibit a peak at 172.93 m z^{-1} corresponding to the calculated mass of 172.93 g $mol^{-1}$of the [$La(OH)_2^+$] cation. All analytical methods employed confirm the presence of IOH-NPs firmly incorporated in the polymer matrix.

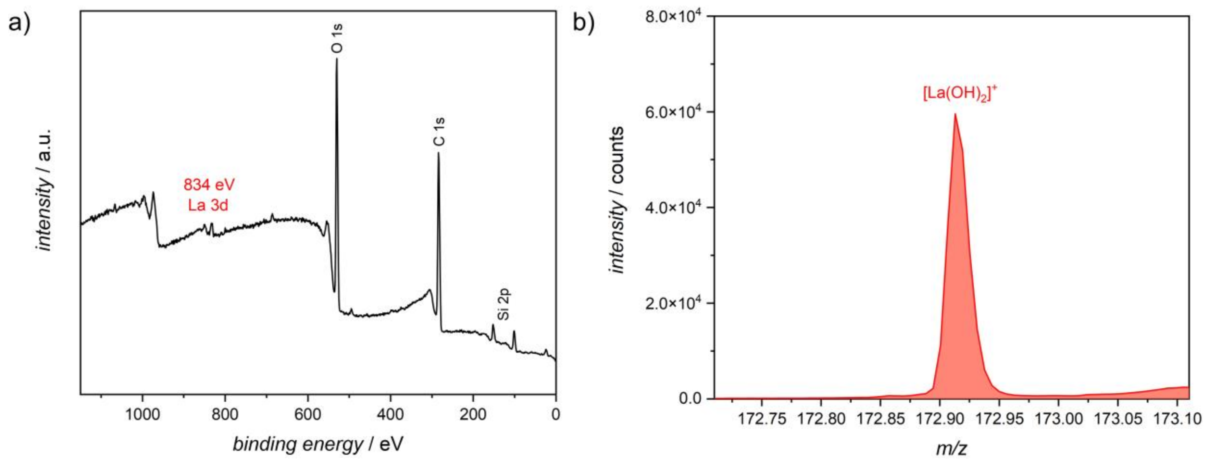

Figure 28. Characterization of the IOH-NPs within the composite material: **a)** XPS spectrum of the 2D composite-material circles. **b)** Mass spectrum recorded by ToF-SIMS on the 2D composite-material circles.

In summary, the composite materials exhibit dual pH-dependent colorimetric and fluorometric changes. The pH responsiveness is analogous to the pH sensitivity of the IOH-NP suspension, indicating successful incorporation of the IOH-NPs in the polymer matrix. The presence of IOH-NPs in the composite material was validated using SEM, EDXS, XPS, and ToF-SIMS. Furthermore, the composite material shows high pH sensitivity, changing its color completely in less than a minute. However, pH sensitivity and responsiveness depend on the IOH-NP concentration. The composite material exhibits a 55 nm red shift of the luminescence based on the pH, which can be used for real-time monitoring of the pH in medicine and biotechnology applications.

6.4 Multi-Material and 3D Composite Fabrication

Multi-materials were fabricated by SLA of a combination between composite-material ink and photoresin without IOH-NPs. Initially, the photoresin without IOH-NPs was used for printing and subsequently, unsolidified material was washed off with 2-propanol. Then the composite-material ink was used for printing. The multi-material demonstrates the possibility to fabricate materials with responsiveness to more than one external stimulus. In addition, the pH-dependent colorimetric properties of a multi-material flower were investigated under neutral and acidic conditions (Figure 29). The outline of the flower was printed using the composite-material ink, whereas the inside of the flower was fabricated without IOH-NPs. For the structure part that contains IOH-NPs, a color change from pH 7 red to pH 1 yellow was observed. The color of the interior of the flower remained unchanged due to the absence of IOH-NPs. Thus, the composite material is suitable for fabrication of multi-responsive materials.

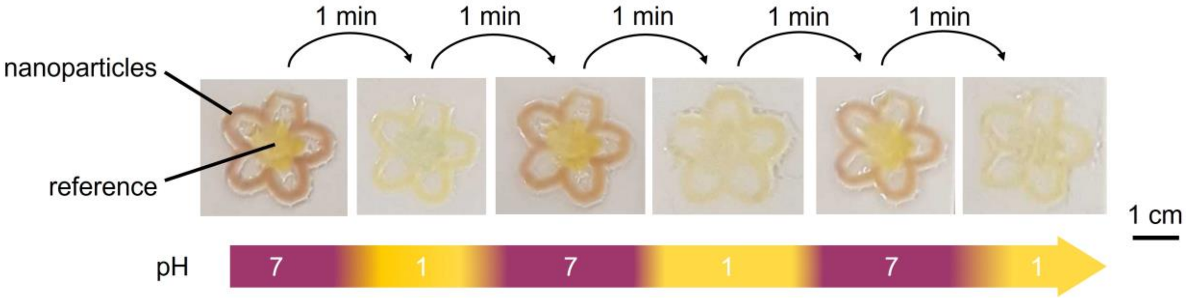

Figure 29. Multi-material flower printed with and without IOH-NPs. pH-dependent color change of the multi-material acquired for pH 7 and 1.

3D fabrication of composite materials was carried out using a DLP. The fabricated 3D composite-material structures exhibit red color, indicating the presence of IOH-NPs. ToF-SIMS was employed to validate the composition of a 3D composite cube. As a result (Figure 30a), a mass peak of 172.93 m z^{-1} was observed corresponding to the calculated mass for $[La(OH)_2]^+$ of 172 g mol^{-1}. Next, the pH-dependent color change of the solid composite structures was examined. However, the response time of the color change was observed to be longer than 12 h. Even after 1 d of immersion in 0.1 M sodium hydrochloride or 0.1 M sodium hydroxide the color change was not completed. The long response time is caused by limited proton diffusion. Thus, the 3D structures were redesigned exhibiting enhanced porosity due to tunnels in the cube, increasing the surface area. By alternating these composite materials between pH 1 and 10 a color change from yellow to dark red and back to yellow was observed in a total time of 6 h (Figure 30b). In addition, the color change was observed to occur throughout the entire composite material, not only on the surface exposed to the pH solution. In contrast, to the printed structures using SLA, the response time appeared longer. This finding suggests that the material thickness, porosity, and IOH-NP concentration have an influence on the response time and sensitivity. Fluorescence spectroscopy (Figure 30c) was used to study the luminescence while alternating the pH between pH 1 and 10. A luminescence shift of around 55 nm wavelength was identified. As a last experiment fluorescence images (Figure 30d) of the 3D composite material were acquired by irradiation of the structures using an LED emitting at 430 (WL-P30EP4545UV140-430) and an optical filter in front of the camera (filtering out light below 500 nm). A green and a yellow fluorescence emission were observed under basic and acidic conditions, respectively. This is in accordance with fluorescence emission spectra recorded for the same structures.

The fluorescence properties of the 3D composite materials were compared with those of the IOH-NPs. The composite materials exhibit a hyperchromic shift in contrast to the IOH-NP suspension (Figure 31). A tenfold higher luminescence intensity of the composite materials was observed. The increase of the fluorescence intensity is attributed to the encapsulation of the IOH-NPs, preventing aggregation-caused fluorescence quenching and suppressing non-radiative decay. Furthermore, neither a hypsochromic nor a bathochromic shift were observed (Figure 31b). Finally, IOH-NP suspensions exhibiting a NP concentration analogous to the concentration in the composite material, complete fluorescence quenching was observed. This highlights that the polymer matrix does not only act as a platform for structuring but also enhances sensitivity to external stimuli by improving chemical and physical properties.

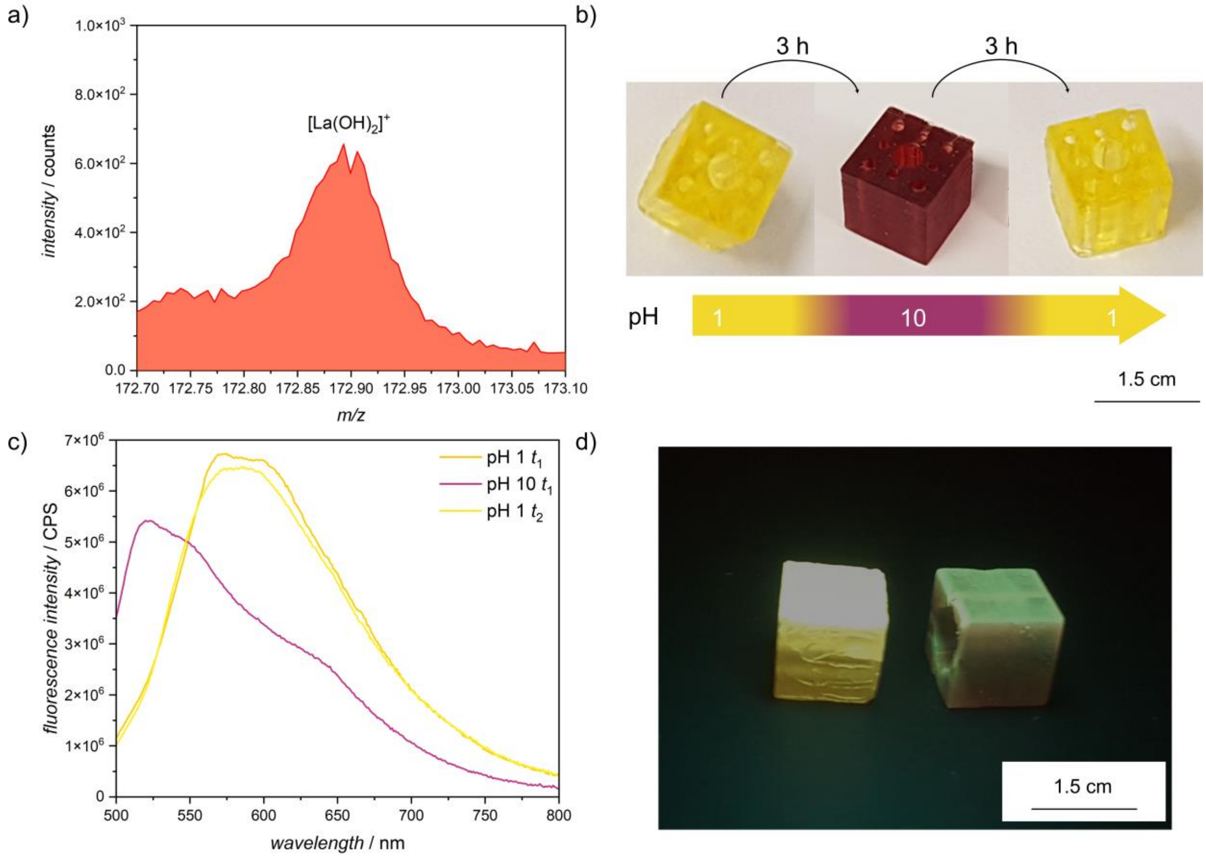

Figure 30. Evaluation of the IOH.NPs within the 3D composite materials and the pH-dependent optical properties of the 3D composite materials: **a)** Mass spectrum recorded by ToF-SIMS on the 3D composite materials. **b)** pH-dependent color change of the composite material for alternating between pH 1 and 10. **c)** Fluorescence spectra recorded of the composite material for alternating between pH 1 and 10 upon excitation at 478 nm. **d)** Fluorescence images acquired for the composite materials using a flat illumination at 430 nm and optical filter, filtering out light below wavelength of 500 nm (composite left: acidic and composite right: basic conditions).

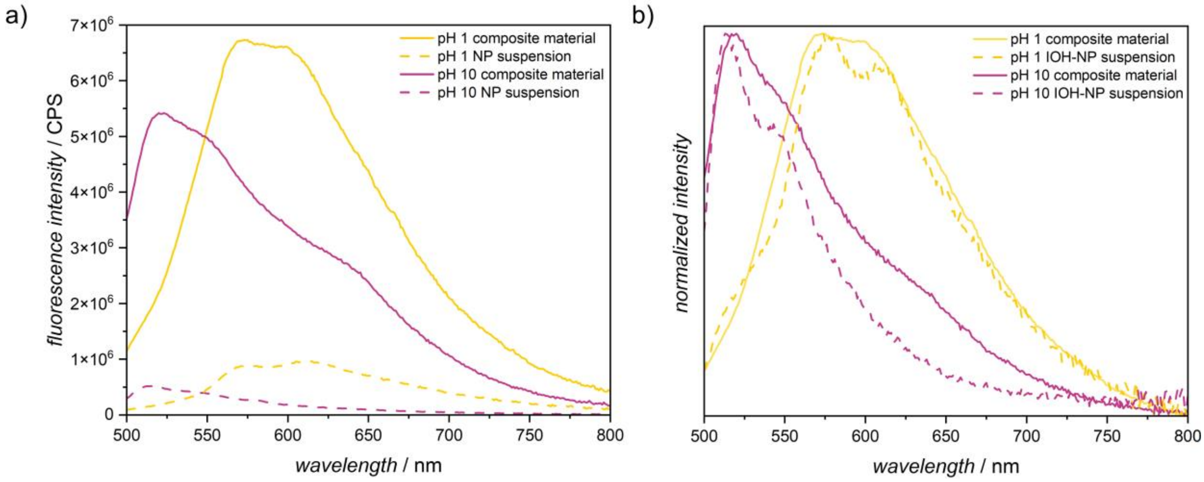

Figure 31. Comparison of 3D composite material with IOH-NP suspension: **a)** Fluorescence spectra of composite material (lines) and IOH-NPs (dashed lines) at pH 1 (yellow) and 10 (violet). **b)** Normalized fluorescence spectra of composite material (lines) and IOH-NP suspension (dashed lines) at pH 1 (yellow) and 10 (violet). The IOH-NP concentration in the composite material is 3.7 g L^{-1} and 0.75 g L^{-1} in the IOH-NP suspension.

The final chapter summarizes the key findings and provides an outlook of possible applications, including the integration of additional stimuli-responsive materials.

6.5 Conclusion

The current chapter focused on the fabrication of pH-responsive composite materials utilizing light-based printing techniques. Initially, the synthesis and complete characterization of $[La(OH)_2]^+[ARS]^-$ IOH-NPs were introduced. pH-dependent color changes combined with fluorometric properties were observed for the IOH-NPs, relevant for their use in pH-responsive composites. In addition, the luminescence emission of the IOH-NPs exhibited a pH-dependent shift from a green (pH > 5) to an orange (pH < 5) emission.

Embedding the IOH-NPs in PEGDA700 was employed to fabricate various 2D and 3D composites, with the resulting composite materials exhibit dual pH responsiveness.

The pH sensitivity of the composites can be tuned by the IOH-NP concentration and the material thickness and porosity. The composites can be used for pH monitoring in applications ranging from medicine to biotechnology due to precise read-out of the pH by visual color change and luminescence shift. In addition, the fabrication of multi-materials was demonstrated, giving rise to multi-responsive materials by integrating other stimuli-responsive materials (e.g., temperature or humidity). Finally, the composites exhibited enhanced luminescence compared to the IOH-NP suspension, highlighting the advantage of composite-material fabrication.

Chapter 7: Printable Flavin-Based Composites for Oxygen Sensing

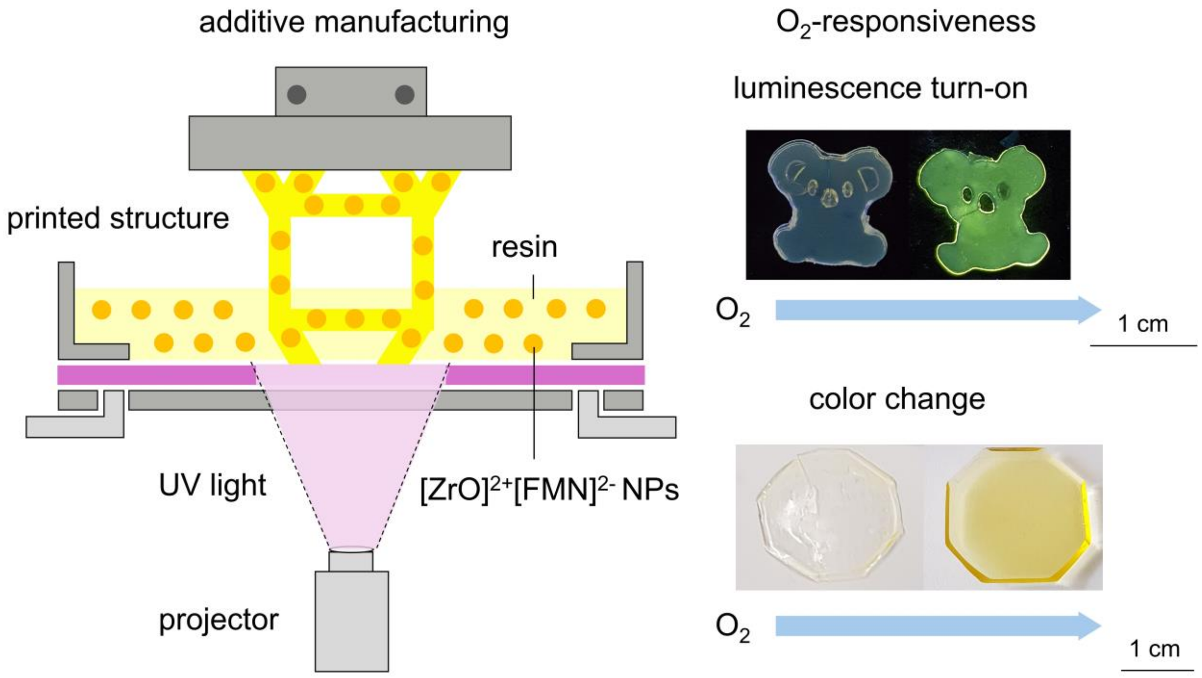

7.1 Introduction

O_2-monitoring is essential for many industries ranging from battery assembly[28-30] and semiconductor manufacturing[161,162] to bioprocessing[163–165] and pharmaceutical production/packaging.[166–168] In the latter, O_2 can reduce drug efficacy and enzyme activity.[166–168] In addition, even trace amounts of O_2 in high-tech assembly lines can lead to material degradation and impair device performance,[162,169] emphasizing the urgent need for precise, scalable and non-invasive O_2-level control. However, O_2-responsive materials are only explored to a limited degree. In 3D printing, O_2 is often undesired because it acts as a radical scavenger, preventing polymer-chain growth and delaying the curing process. In addition, O_2 is known to quench type II initiators in their triplet state forming stable peroxyl radicals, limiting the monomer-to-polymer conversion.[170] However, small amounts of O_2 can be used to create an inhibition layer through a small O_2-permeable membrane at the bottom of the resin vat, leading to faster printing and smoother surfaces.[171] Current state-of-the-art O_2 sensors rely on luminescent precious-metal complexes (e.g., ruthenium(II) polypyridyl or platinum(II) porphyrins), which exhibit high O_2-sensitivity due to dynamic fluorescence quenching.[172–174] The disadvantages of using precious-metal complexes are their costliness and time-consuming, complex synthesis.[175] Furthermore, they are often toxic and photolabile, limiting device integration for potential applications.[176–179] In the current chapter, a low-cost, biocompatible, O_2-sensitive composite material using scalable light-based printing is introduced. The composite consists of IOH-NPs based on flavin mononucleotide (FMN) embedded into a polyethylene-glycol-diacrylate matrix. The O_2 sensor exhibits dual colorimetric and fluorescence-based O_2 monitoring with time and concentration-dependent behavior. Finally, examples for the integration of the sensor into diverse platforms for non-invasive O_2 monitoring in pharmaceutical and food packaging are demonstrated.

The next section focuses on the synthesis and characterization of the FMN-based IOH-NPs. In addition, an insight into the O_2-responsive optical properties of the IOH-NPs is provided.

7.2 Inorganic-Organic Hybrid Nanoparticles

FMN is a riboflavin (vitamin B2) derivative that acts as cofactor in a wide variety of redox reactions.[180–182] The flavin ring system can either accept or donate electrons (Figure 32). Previously, $[ZrO]^{2+}[FMN]^{2-}$ IOH-NPs have been prepared and used them as luminescent biomarkers in living mice and cells.[183] In addition, FMN can be used in small quantities in the co-precipitation with drugs as fluorescent marker.[184] The use of FMN in sensor applications arises from the change in optical properties of the oxidized and reduced form.[185,186] Generally, FMN is reduced in a two-electron transfer from its oxidized quinone form (FMN) to the fully reduced hydroquinone ($FMNH_2/FMNH^-$) with a midpoint redox potential of -0.22 V vs. standard hydrogen electrode (SHE) at pH 7.[187] Sodium dithionate exhibits a standard reduction potential of -0.66 V vs. SHE at neutral pH and is therefore, sufficient to reduce FMN completely.[188] While the oxidized form of FMN exhibits intense fluorescence and yellow color, the reduced form shows no luminescence and is transparent. Therefore, FMN is suitable to detect O_2 based on a combination of colorimetric and fluorometric analysis. The latter exhibits high sensitivity, spatiotemporal resolution, and rapid response times while being non-invasive.

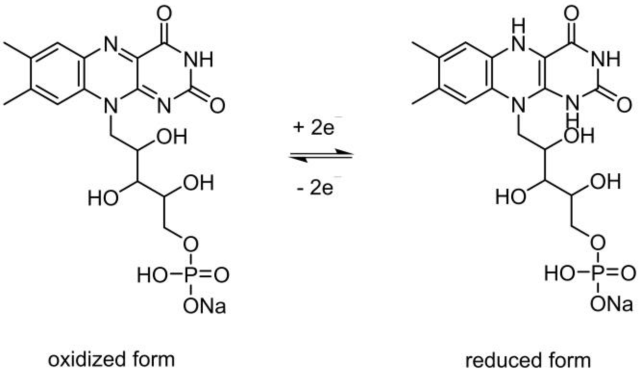

Figure 32. Oxidized and reduced form of FMN.

Synthesis

FMN contains phosphate moieties, which can be coordinated by zirconyl cations to facilitate the formation of water-insoluble IOH-NPs. The synthesis of $[ZrO]^{2+}[FMN]^{2-}$ IOH-NPs was adapted from the literature,[183] by dissolving 30.0 mg Na(HFMN)

(0.063 mmol, 1.0 eq.) in 50 mL water. IOH-NP formation takes place upon injection of 18.0 mg $ZrOCl_2 \cdot 8H_2O$ in 0.5 mL water (0.056 mmol, 0.9 eq.) under vigorously stirring. After the injection, clouding as well as the formation of a Tyndall cone were observed. Subsequently, the IOH-NPs were separated from the starting material and purified by centrifugation (20.000 rpm, 15 min, 4 °C).

Particle size, composition, and O_2-sensitive optical properties were investigated in detail.

Characterization

The particle size of the $[ZrO]^{2+}[FMN]^{2-}$ IOH-NPs was determined by DLS and SEM measurements (Figure 33). Both analytical methods confirmed the successful synthesis of NPs. DLS measurements show a broad size distribution with a mean hydrodynamic diameter d_H of 53±14 nm for the oxidized IOH-NPs. In comparison, the SEM analysis of 100 particles shows spherical NPs with a mean particle size of 41±10 nm. The DLS measurements account for the hydration shell surrounding the IOH-NPs resulting in larger particle sizes. The particle size of the herein prepared IOH-NPs is roughly 10 nm larger compared to the particle size described in the literature.[183]

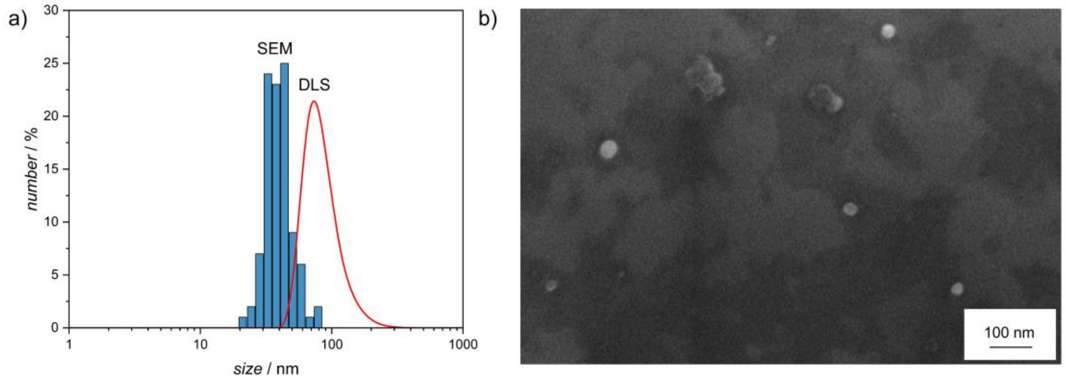

Figure 33. Size and morphology of [ZrO]$^{2+}$[FMN]$^{2-}$ IOH-NPs. **a)** Size distribution determined by DLS (red) and by counting 100 individual NPs from SEM images (blue). **b)** SEM image of [ZrO]$^{2+}$[FMN]$^{2-}$ IOH-NPs.

As mentioned before, the [ZrO]$^{2+}$[FMN]$^{2-}$ IOH-NPs can be reduced by addition of sodium dithionite. The reduction of the IOH-NPs can affect the particle size or result in dissolution. Thus, DLS measurements were conducted on oxidized and reduced IOH-NPs (Figure 34a). The reduced IOH-NPs exhibit a mean hydrodynamic diameter d_H of 54±12 nm respectively, indicating that the redox transitions occur without any significant change in size.

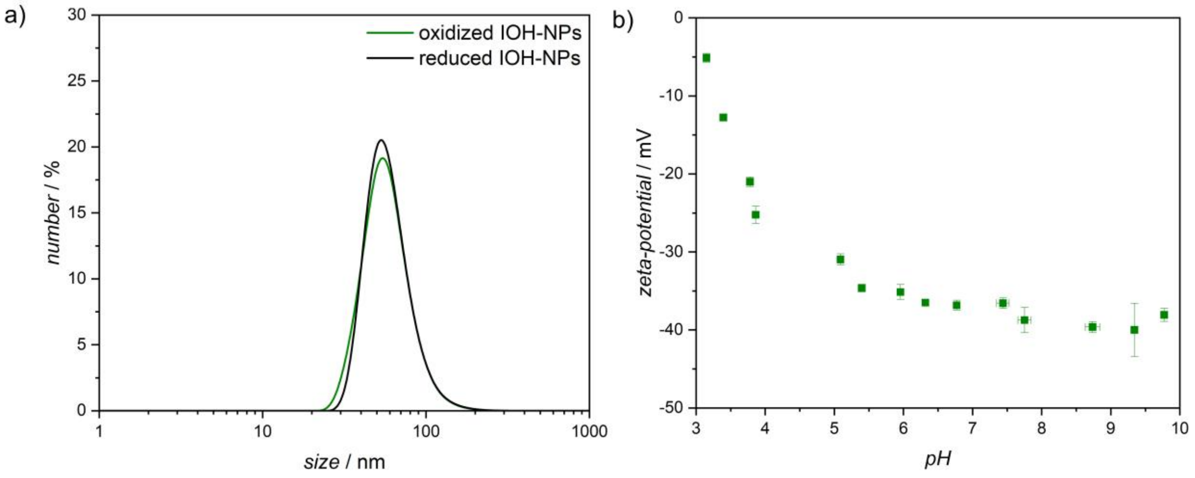

Figure 34. a) Size distribution determined by DLS measurements of oxidized (green) and reduced (grey) [ZrO]$^{2+}$[FMN]$^{2-}$ IOH-NP suspension. **b)** Zeta potential of [ZrO]$^{2+}$[FMN]$^{2-}$ IOH-NPs at different pH values.

Zeta-potential analysis (Figure 34b) was performed at different pH to assess the stability of the $[ZrO]^{2+}[FMN]^{2-}$ IOH-NPs. The zeta potential is used to quantify the surface charge of the IOH-NPs. According to zeta-potential measurements, the IOH-NPs show high colloidal stability at pH 5-10 with a zeta potential ranging from -32 to -38 mV, which is considered colloidally stable.[128]

Subsequently, the chemical composition of the IOH-NPs was investigated by FT-IR spectroscopy, TGA, EDXS, PXRD and EA. The FT-IR spectrum of the IOH-NPs closely resembles the FT-IR spectrum of Na(HFMN) (Figure 35a), indicating the presence of FMN in the IOH-NPs. The IOH-NPs, as well as Na(HFMN) exhibit the stretching vibration $\tilde{\nu}$(O-H) = 3600-2500 cm^{-1} caused by the hydroxyl moieties of FMN. In addition, residual water present after synthesis and drying can still be adsorbed on the NP surface. Vibrations at $\tilde{\nu}$ = 3300 cm^{-1} are assigned to the stretching vibration of secondary amine $\tilde{\nu}$(N-H), at $\tilde{\nu}$ = 3100 – 3000 cm^{-1} and 2930 and 2850 cm^{-1} are attributed aromatic and aliphatic C-H groups $\tilde{\nu}$(C-H), respectively. The vibrations at $\tilde{\nu}$(C=O) = 1715 and 1660 cm^{-1} correspond to the stretching vibrations of the carbonyl moieties. Vibrations characteristic for oxidized flavin are attributed to the vibrations at $\tilde{\nu}$ = 1625, 1577, 1548 and 1501 cm^{-1}. The broad vibration at $\tilde{\nu}$ = 1006 cm^{-1} corresponds to the P=O vibration.[181]

TGA of the $[ZrO]^{2+}[FMN]^{2-}$ IOH NPs (Figure 35b) shows the decomposition of the IOH-NPs in three steps. The first decomposition step with a mass loss of 14.0 wt-% is completed at approximately 215°C. The mass loss is attributed to the evaporation of residual water, which was adsorbed on the IOH-NPs surface due to aqueous synthesis. Subsequently, the decomposition of the organic components between 215°C and 600°C into CO_2, N_2 and H_2O with a mass loss of 50.0% was observed. The last decomposition step observed at 950 - 1200 °C with a mass loss of 4.8 wt-% is assigned to the condensation reaction of the phosphate moieties and the loss of P_4O_{10}. The residue (31.2 wt-% by mass) was assessed by PXRD (Figure 35c), which confirms the presence of $Zr_2O(PO_4)_2$. In addition, EDXS analysis (Figure 35d) of the $[ZrO]^{2+}[FMN]^{2-}$ IOH NPs exhibits the presence of Zr and P in the sample. This leads to the following decomposition equation:

$$2\ [ZrO]^{2+}[C_{17}H_{19}N_4O_9P]^{2-} + 38\ O_2 \rightarrow Zr_2O(PO_4)_2 + 34\ CO_2 + 19\ H_2O + 4\ N_2$$

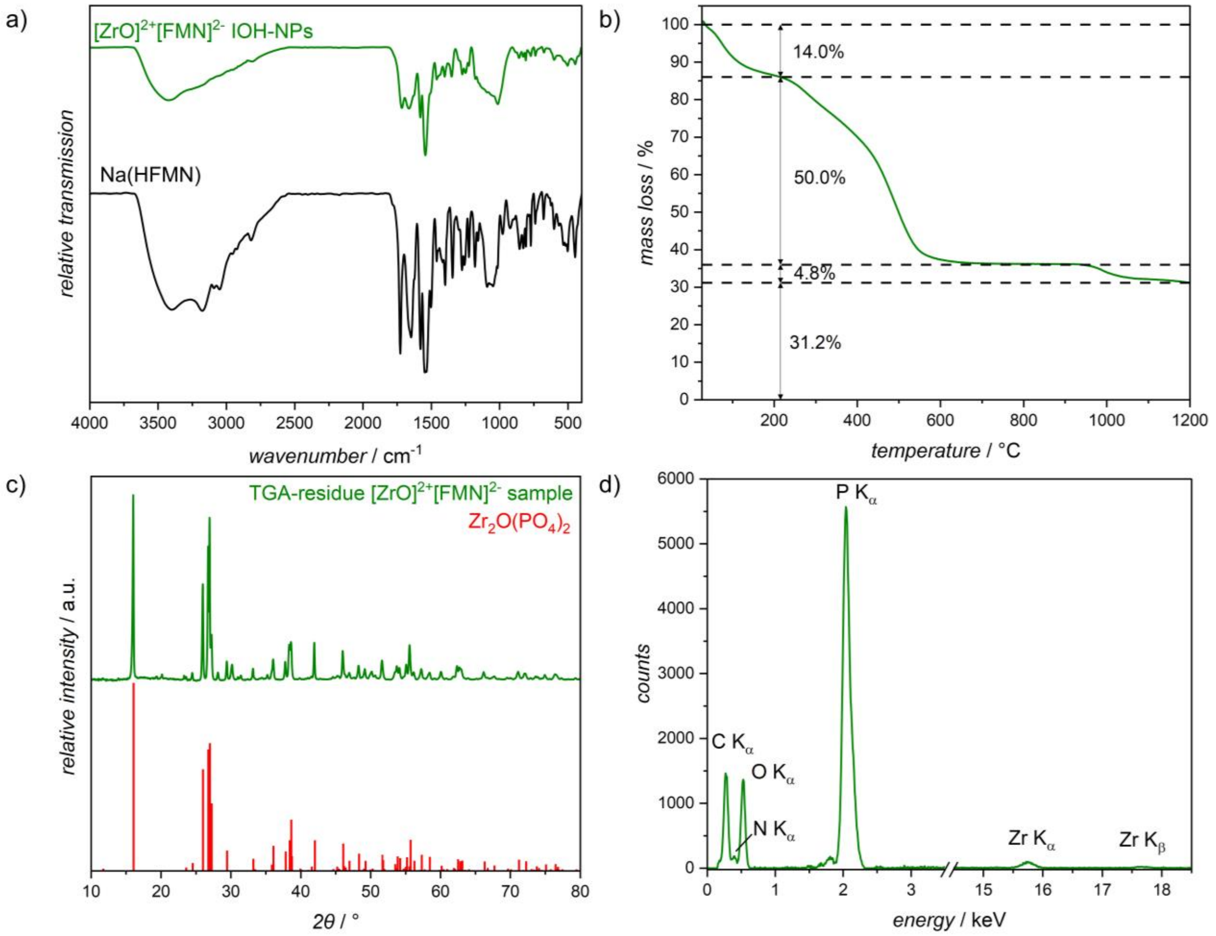

Figure 35. Determination of the composition of $[ZrO]^{2+}[FMN]^{2-}$ IOH-NPs: **a)** FT-IR spectra of IOH-NPs (red) and Na(HFMN) (black). **b)** TGA spectrum for the IOH-NP combustion. **c)** PXRD of the TGA residue (red) and reference (red). **d)** EDXS spectrum of the IOH-NPs.

The obtained amounts of C, H and N by EA of the $[ZrO]^{2+}[FMN]^{2-}$ IOH NPs (Table 3) were corrected for the content of adsorbed water of 14.0 wt-% and match with a composition of $[ZrO]^{2+}$ to $[FMN]^{2-}$ of 1:1. The differences between the corrected and theoretically expected mass loss arise from the presence of phosphate in the sample, which can serve as flame retardant leading to incomplete combustion.[189,190]

Table 3. EA and TGA of $[ZrO]^{2+}[FMN]^{2-}$ IOH-NPs compared to the expected calculated values.

	C [wt-%]	H [wt-%]	N [wt-%]	Mass loss [wt-%]
Measurement	31.8	3.8	8.2	68.8
Corrected (-14.0 wt-% water)	37.0	2.6	9.5	63.4
Calculated	36.4	3.4	9.9	65.4

The optical properties of the $[ZrO]^{2+}[FMN]^{2-}$ IOH-NPs (Figure 36) were investigated using UV-Vis and fluorescence spectroscopy. The O_2 response of the $[ZrO]^{2+}[FMN]^{2-}$ IOH-NPs is based on their optical properties (i.e., color change and fluorescence turn-on). A change in color from transparent (reduced state) with a broad UV absorption around 340 nm to yellow (oxidized state) with two characteristic absorption peaks at 370 and 450 nm was observed.[182] Fluorescence spectroscopy reveals that for an excitation wavelength of 366 nm in the reduced state, the luminescence is completely quenched and, upon oxidation, an intense green fluorescence at 535 nm was observed.

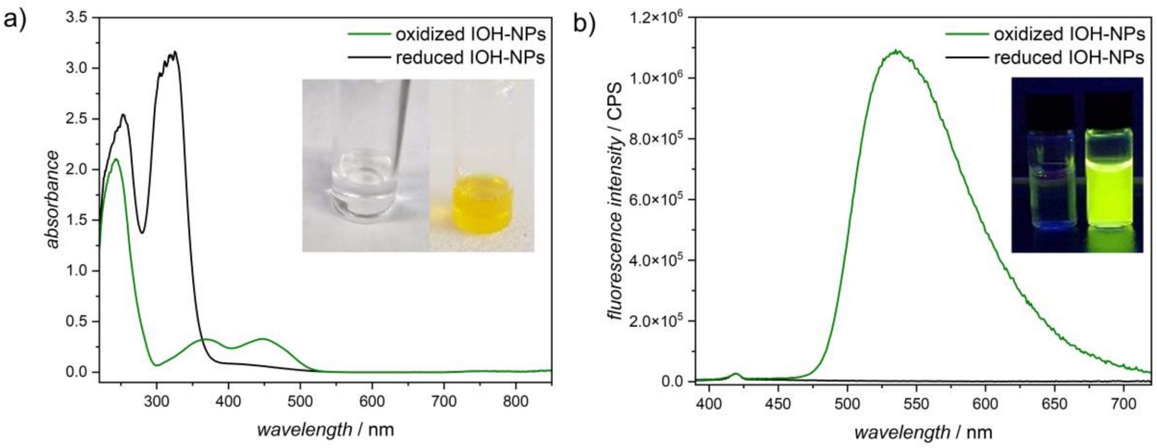

Figure 36. O_2-sensitive optical properties of the IOH-NPs: **a)** UV-Vis spectra and images of oxidized and reduced IOH-NP suspension. **b)** Fluorescence spectra and luminescence images of oxidized and reduced IOH-NP suspension.

A further critical aspect for using $[ZrO]^{2+}[FMN]^{2-}$ IOH-NPs as a key component of an O_2 sensor relates to the reversibility of the O_2 responsiveness. Thus, the reversibility of the luminescence turn-on over 3 cycles of oxidation and reduction was studied by fluorescence spectroscopy. The fluorescence spectra (Figure 37a) recorded using an excitation wavelength of 366 nm, show highly reversible O_2 responsiveness. For all redox cycles, almost identical luminescence turn-on and complete luminescence turn-off upon reduction were observed. In addition, no luminescence loss upon oxidation was noted for the three cycles, which could otherwise be caused by IOH-NP leaching. Moreover, UV-Vis spectra (Figure 37b) for alternating the IOH-NPs between reduced and oxidized states were collected, exhibiting characteristic double peaks for oxidized FMN upon oxidation in all three cycles. No change in absorbance was recorded for the oxidized IOH-NPs. The UV-Vis spectra show that, upon reduction, the characteristic double peaks of oxidized FMN disappear consistently in all cycles. Both fluorescence and UV-Vis spectroscopy demonstrate high reversibility of the IOH-NP suspension. Combined with the O_2-sensitive optical properties, the reversibility of the $[ZrO]^{2+}[FMN]^{2-}$

IOH-NPs makes them highly attractive as a low-cost, biocompatible component for O_2 sensors.

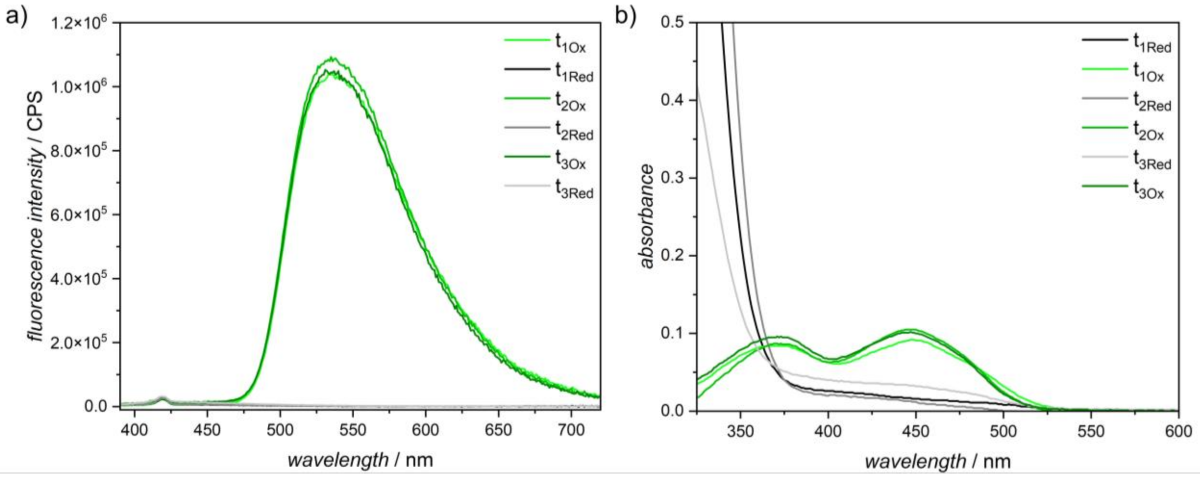

Figure 37. Reversibility of the optical properties assessed for three cycles of alternating the $[ZrO]^{2+}[FMN]^{2-}$ IOH-NPs between the oxidized and reduced states. **a)** Fluorescence spectra of three cycles alternating between oxidized and reduced IOH-NPs, recorded using an excitation wavelength of 366 nm. Fluorescence spectra of the oxidized IOH-NPs exhibit no luminescence loss, and fluorescence spectra for the reduced IOH-NPs show complete luminescence quenching. **b)** UV-Vis spectra collected for switching the IOH-NPs between the oxidized and reduced states for three cycles. The UV-Vis spectra for the oxidized IOH-NPs show characteristic double peaks known for oxidized FMN, whereas the reduced IOH-NPs do not show absorbance in that region.

Furthermore, the time-dependent O_2 responsiveness of the IOH-NPs is critical for their application as functional materials in O_2-sensitive composite-material fabrication. Thus, an IOH-NP concentration of 0.05 g L^{-1} dispersed in H_2O and reduced using 3 mg of sodium dithionite was used to examine the temporal resolution of the luminescence turn-on and the visible color change (Figure 38). The reduced suspension was stirred under air at ambient temperature while performing fluorescence and UV-Vis spectroscopy. Fluorescence spectra were recorded in intervals of 2 min to determine the time-dependent luminescence turn-on after IOH-NP reduction using an excitation wavelength of 366 nm. Complete luminescence turn-on was observed after 10 min. In addition, the color change from transparent to yellow, reduced to oxidized IOH-NPs was completed after 180 min. These findings highlight the high sensitivity of the fluorometric analysis, which is 18-times faster compared to the color change.

After verifying the successful synthesis of $[ZrO]^{2+}[FMN]^{2-}$ IOH-NPs and highlighting their O_2-responsive colorimetric and fluorometric properties their use as functional component in composite materials was explored.

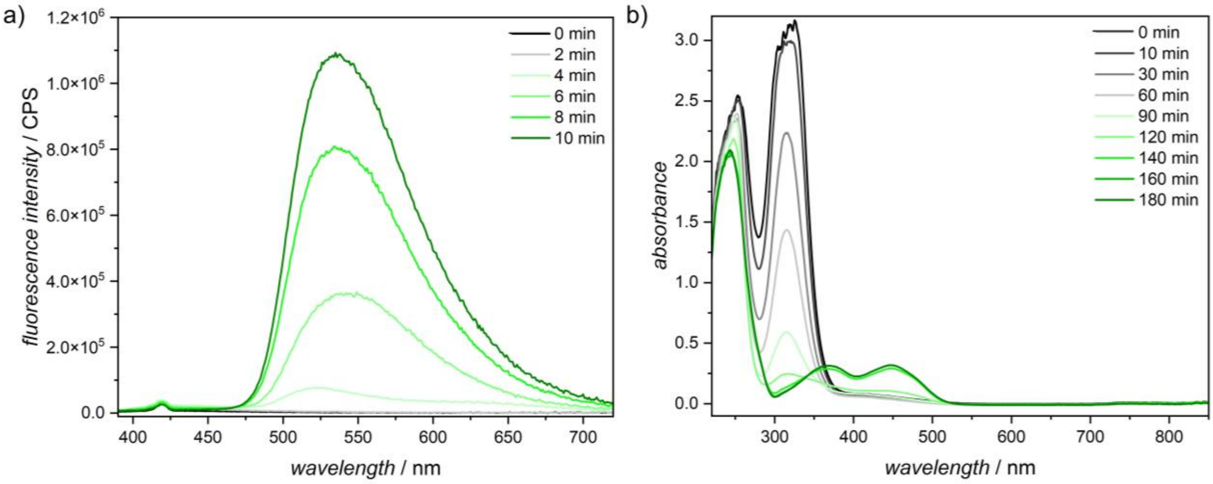

Figure 38. Time-dependent studies: **a)** Time-dependent luminescence turn-on and **b)** time-dependent color change of completely reduced 0.05 g L^{-1} IOH-NP suspension using sodium dithionite in air at ambient conditions.

7.3 Composite-Material Ink Design

Light-based printing techniques were selected for AM of O_2-responsive composite materials due to high scalability combined with excellent spatiotemporal resolution. Additional advantages include reduced waste production and ability to fabricate complex 3D structures.[37] To prepare a bench-stable composite-material ink providing high reproducibility and manufacturing feasibility for light-based printing, an ink composed of three components – a monomer, a photoinitiator and redispersed IOH-NPs was prepared. PEGDA700 was selected as monomer due to commercial availability, ability to dissolve small quantities of photoinitiator and chemical and physical stability. Moreover, PEGDA700 ensures high water compatibility, stabilizing the IOH-NP suspension and preventing agglomeration and sedimentation of the IOH-NPs in the composite-material ink.[191] Agglomeration and sedimentation result in the loss of IOH-NP functionality, ultimately reducing the O_2-adaptability of the fabricated composite. The solidification of PEGDA700 resulted in a biocompatible, transparent polymeric network essential to enable read-out the O_2-dependent color and luminescence intensity change.[192] Likewise, separate luminescence of photoinitiator and the IOH-NPs (500-700 nm) is crucial for fluorescence-based O_2-monitoring. Additional prerequisites for the photoinitiator include water compatibility and biocompatibility to ensure the use of the fabricated composite in medicine applications and bioprocessing. The photoinitiator should exhibit high polymerization efficacy to ensure the solidified polymeric network appears transparent. In addition, a photoinitiator with high polymerization efficacy can help to compensate for light scattering and absorption caused by the IOH-NPs. Thus, lithium phenyl-2,4,6-trimethylbenzoylphosphinate (LAP) at a concentration of 0.1 wt-% was selected. LAP was used as a photoinitiator for the fabrication of various biocompatible materials and exhibits high polymerization efficacy around 405 nm with luminescence below 500 nm.[193]

The composite-material ink was prepared by mixing different concentrations of IOH-NPs dispersed in 2 mL water with 10 mL PEGDA700. Subsequently, 0.1 wt-% LAP were dissolved in water, added to the mixture and vigorously stirred overnight. The final composite-material ink can be stored for several months in the dark.

In addition to the selection of the individual components, the ratio of water-to-monomer is essential to tune the ink viscosity as well as the mechanical properties of the fabricated composite. Thus, in the following section, composite materials composed of different water-to-monomer ratios (1:5, 3:7, 1:2, 7:3 and 1:1) were examined based on their shrinkage, swelling, and IOH-NP leaching when exposed to water (Figure 39). Less pronounced shrinkage and swelling were observed for the composite materials with lower water-to-monomer ratios, for instance, the 1:5 ratio composite exhibited 5 % shrinkage and 20 % swelling, whereas the 1:1 ratio composite showed increased shrinkage and swelling of 25 and 67 %, respectively. Subsequently, leaching of IOH-NPs from the composites was studied by immersing them in water overnight. In the case of leaching, water should turn yellow due to the release of IOH-NPs from the polymer. This was observed for the composites with 7:3 and 1:1 water-to-monomer ratios. Finally, the luminescence properties of the composites with 1:5, 3:7, 1:2 water-to-monomer ratios were investigated using fluorescence spectroscopy. The highest luminescence intensity was observed for the 1:5 ratio composite compared to the water-to-monomer ratios of 3:7, 1:2. In summary, the composite with the water-to-monomer ratio of 1:5 showed good mechanical integrity, excellent IOH-NP retention and intense luminescence. Thus, this ratio was used to prepare the composite-material ink for DLP, described in detail below.

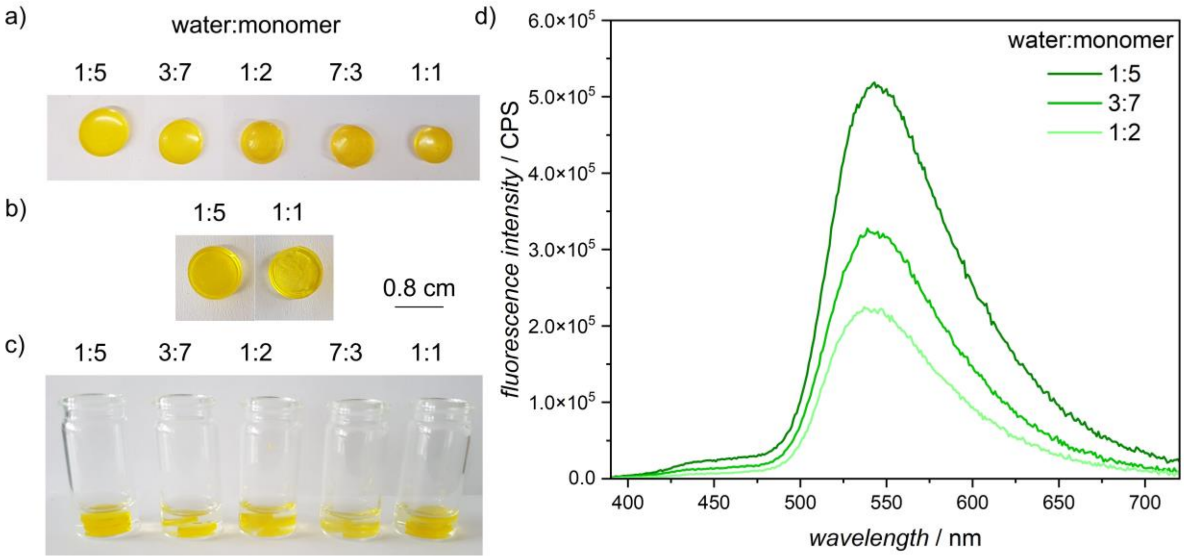

Figure 39. Investigation of the water-to-monomer ratio dependent material properties and sensor performance. **a)** Composite-material shrinkage, **b)** swelling and **c)** leaching for different monomer-to-water contents. **d)** Fluorescence spectra recorded for different monomer-to-water contents using an excitation wavelength of 366 nm.

In a next step, the optimized ink formulation was used to fabricate O_2-responsive composite materials, and studies on how the ink composition translates into practical sensor performance were conducted.

7.4 Composite-Material Fabrication

Utilizing the composite-material ink, O_2-responsive materials can be fabricated using different techniques (i.e., spin-coating and DLP). These fabrication techniques can be used to tailor geometry and material thickness based on the desired application ranging from packaging and industrial applications to their use in O_2-monitoring in GMP lines for pharmaceuticals, batteries, and semiconductors. On the one hand, spin-coating and subsequent solidification using a 385 nm LED (SBM-120-UV-F34-L385-22) was employed to fabricate 100 µm thick composite-material films on glass coverslips. On the other hand, a DLP printer (3D HALOT-ONE CL-60 LCD-Resin printer from Creality) equipped with a 405 nm wavelength LED was used to prepare composite samples with various geometries (e.g., spots and koalas), and thicknesses ranging from 125 to 1500 µm (Figure 40a). The O_2-dependent change of optical properties (Figure 40b and c), was examined for a composite material containing 0.6 g L^{-1} IOH-NPs. After the composite-material fabrication, the sensor performance affected by the IOH-NP concentration and material thickness was studied based on the O_2-dependent luminescence turn-on and colorimetric change.

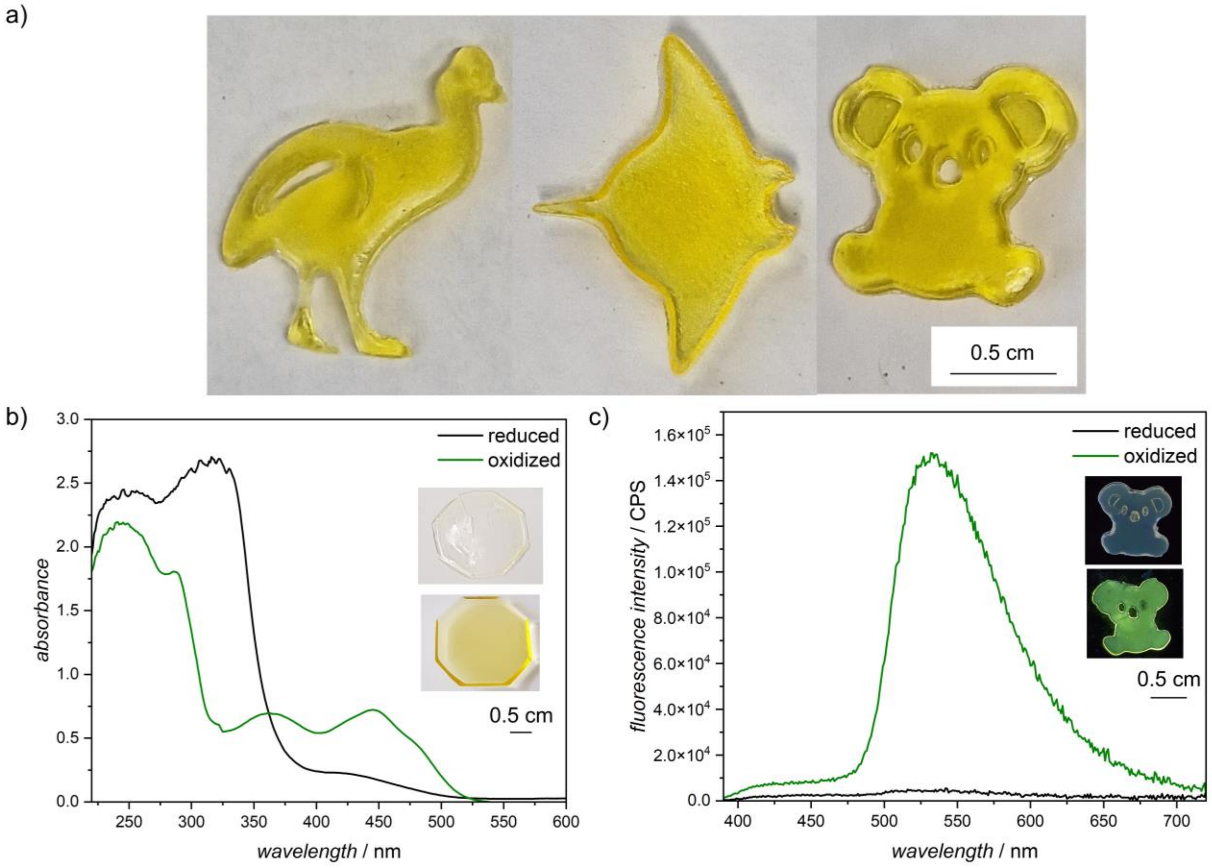

Figure 40. Composite-material fabrication and optical properties: **a)** DLP printed composite material in various shapes. **b)** UV-Vis spectra and inset with visible color change of reduced and oxidized composite material **c)** Fluorescence spectra and inset with fluorescence images of reduced and oxidized composite material.

Initially, the influence of the IOH-NP concentration on sensor performance and sensitivity was examined by fluorescence and UV-Vis spectroscopy. For high IOH-NP loadings improved sensor performance and sensitivity are expected due to increased luminescence and optical contrast. However, the IOH-NPs are prone to agglomeration in the composite-material ink at high NP concentrations, leading to potential shielding from O_2. IOH-NPs agglomeration ultimately causes sensing gradients and results in prolonged response times. Furthermore, an increase in the IOH-NP loading leads to longer times for composite-material reduction using sodium dithionite. Three different IOH-NP loadings (i.e., 0.35, 0.7, 1.4 g L^{-1}) were examined by their O_2-dependent luminescence turn-on at 535 nm and colorimetric change (appearance of absorption peaks at 370 and 450 nm) upon oxidation after complete reduction. The fluorescence spectra (Figure 41a) showed the most intense luminescence for the composite sample with an IOH-NP loading of 1.4 g L^{-1} and the lowest fluorescence intensity was recorded for an IOH-NP loading of 0.35 g L^{-1}. These findings are in good agreement with the expectations. The fluorescence spectra were collected using an excitation wavelength of 366 nm. Furthermore, the composite with an IOH-NP concentration of 1.4 g L^{-1} showed the most noticeable color change (Figure 41b) from transparent to yellow, whereas for the sample containing 0.35 g L^{-1} IOH-NPs a less distinct color change was observed, as expected. Comparing the time used for complete composite-material reduction of each IOH-NP concentration, the fastest reduction time of 30 s was observed for the lowest concentration. The composite with 0.7 and 1.4 g L^{-1} required 5-10 min and 5 h for complete reduction using sodium dithionite, respectively. Thus, IOH-NP loadings of 0.6-0.8 g L^{-1} were selected for further sensor performance and sensitivity studies.

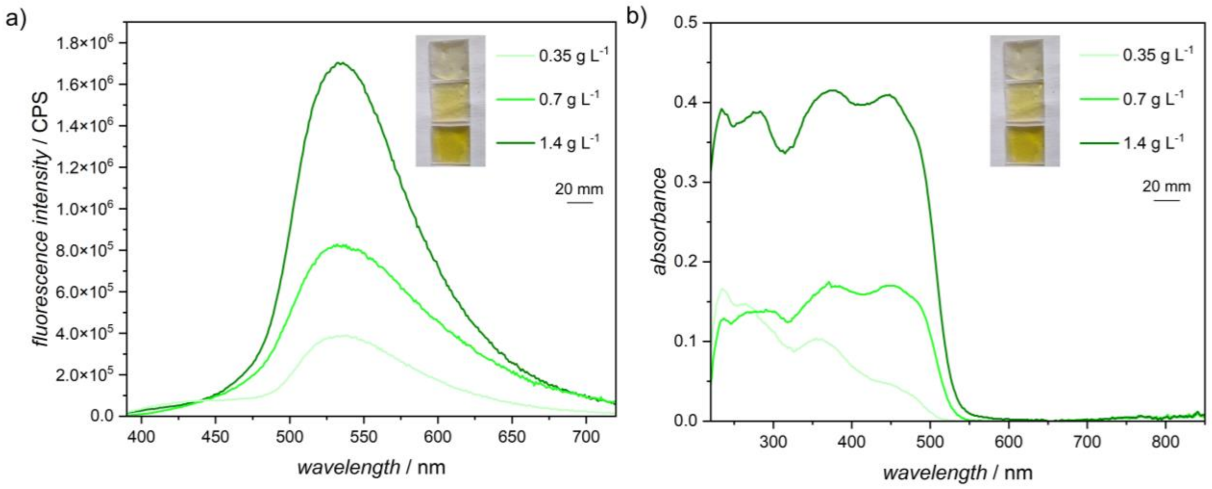

Figure 41. Concentration-dependent studies of optical properties: **a)** luminescence and **b)** color change investigated by fluorescence and UV-Vis spectroscopy, respectively.

As mentioned before, the use of spin-coating and DLP allows the preparation of composites with varying material thickness. The material thickness influences the sensor performance by determining the rate of O_2 diffusion to the functional IOH-NPs incorporated in the polymer matrix. In addition, the material thickness affects the physical properties such as material flexibility and IOH-NP loading capacity. Thus, tailoring the material thickness is essential in terms of sensor performance and long-term stability. On the one hand, thin composite films provide rapid response time due to fast O_2 diffusion. On the other hand, thin films suffer reduced IOH-NP loading and durability, whereas thicker composites contain higher IOH-NP loading and exhibit enhanced long-term stability. However, thicker sensors exhibit longer response times and potential inhomogeneous sensing across the layers can be observed. For instance, in food or pharmaceutical packaging or semiconductor storage, thin films are advantageous due to rapid O_2-ingress sensing, indicating spoilage and altering material properties. In contrast, thicker composites are better adapted for use in GMP-lines and bioreactors, as their enhanced mechanical stability allows them to withstand higher shear forces than thin films. Two different material thicknesses of 500 and 125 µm were investigated based on their time-dependent luminescence turn-on under air (Figure 42). Prior to the experiment, the different composites (8 mm wide) containing 0.6 g L^{-1} IOH-NPs were completely reduced using sodium dithionite to turn-off the FMN luminescence. The thinner composite should exhibit improved O_2 diffusion and thus a faster response time. For the 500 µm thick composite material a response time of 50 min was observed, whereas the 125 µm thin composite showed a faster response time of 5 min for complete luminescence intensity recovery. In total, the thinner sensor exhibits a tenfold faster response time for the luminescence turn-on, which is in good agreement with the described expectations.

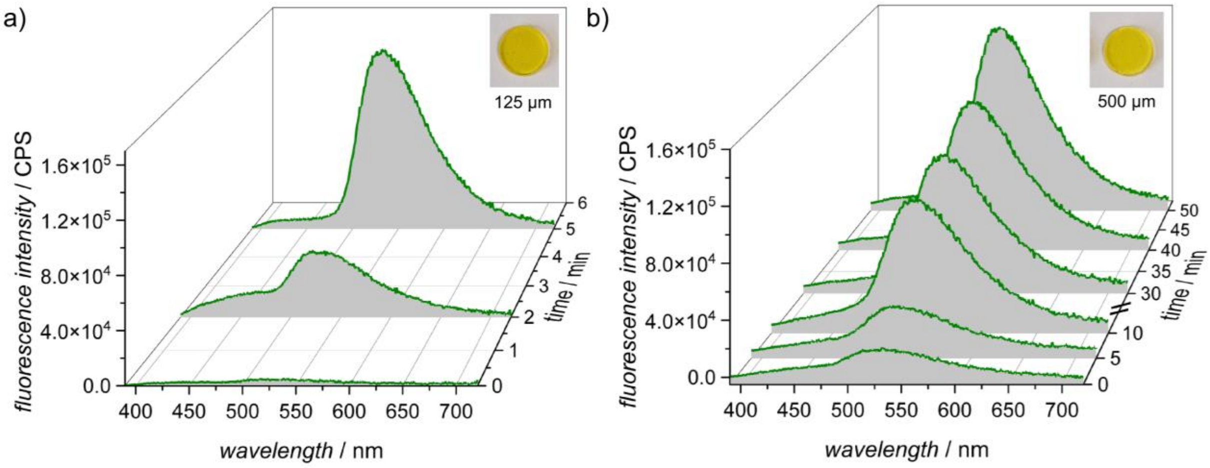

Figure 42. Time-dependent re-oxidation after complete reduction of 8.0 mm-wide sensor with sodium dithionite. The IOH-NP concentration is 0.6 g L^{-1} and composite-material thicknesses are **a)** 500 µm and **b)** 125 µm.

In summary, adjusting the IOH-NP concentration as well as tailoring the material thickness play an essential role in sensor performance, sensitivity, and application. These parameters affect the temporal resolution, which is determined by the desired application. The findings showed that thin films combined with low amounts of IOH-NPs achieve rapid detection of small O_2 amounts but suffer from reduced optical contrast. Slower response times were observed for thicker composites, which showed enhanced luminescence intensity and well-pronounced color changes. The findings suggest that by adjusting the IOH-NP concentration and the material thickness, the fabrication of composites tailored to various applications can be achieved.

The photostability of the composite material was compared to the IOH-NP suspension and Na(HFMN) in water using UV-Vis spectroscopy equipped with a 50 W halogen lamp (Figure 43). Over 12 hours, the samples were continuously irradiated at 250 nm, and the absorption at 445 nm was simultaneously measured. Over time an absorption decrease for Na(HFMN) was discovered, indicating photodegradation. High photostability was observed for the composite materials as well as the IOH-NP suspension. Thus, the luminescence read-out of the O_2 sensor using a UV- or blue-light-emitting flashlight should not interfere with the sensor performance due to photobleaching.

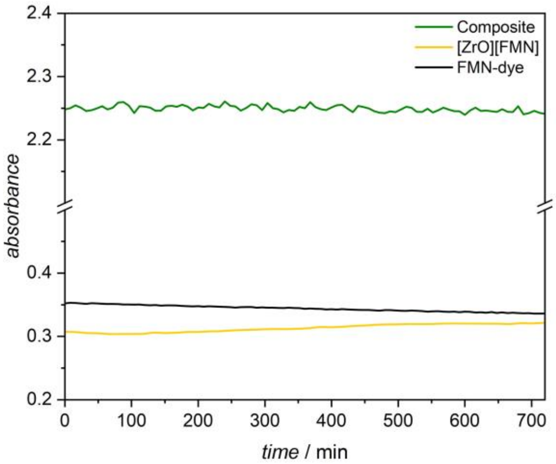

Figure 43. Photostability assessed for composite material (green), IOH-NP suspension (yellow) and Na(HFMN) in water (black).

Subsequently, the photostability of the composite material was investigated in more detail using fluorescence and UV-Vis spectroscopy before and after continuous irradiation with a 385 nm-emitting LED (12 V, 0.03 A, 2 cm distance to sample). This wavelength was selected because the optical read-out of the composite material was performed using UV or blue light. The fluorescence spectra (Figure 44a) exhibit no loss in luminescence intensity and no shift emission wavelength. In addition, the UV-Vis spectra (Figure 44b) show two characteristic peaks known for oxidized FMN, which do not change their absorbance upon continuous irradiation. These results indicate high photostability of the composite material.

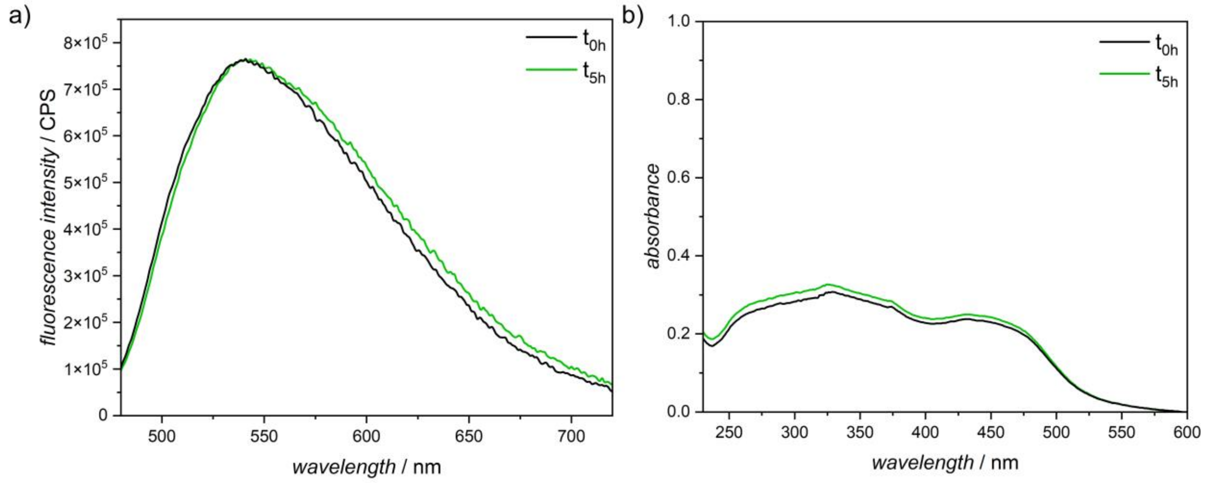

Figure 44. Photostability assessed for composite material after continuous irradiation of 5 h using a 385 nm-emitting LED. **a)** Fluorescence spectra recorded before and after irradiation showing no luminescence loss. **b)** UV-Vis spectra collected before and after irradiation exhibiting no absorbance loss.

Next, the presence of the IOH-NPs within the composite materials (containing 0.8 g L^{-1} IOH-NPs) was investigated by preparing a cross-section using FIB cutting. The cross-section was characterized using SEM and EDXS analysis (Figure 45) conducted by Kristian Kraft (LEM, KIT). The IOH-NPs should appear bright in the SEM analysis due to the Zr content within the particles in contrast to the polymer, which is mainly composed of carbon. SEM analysis revealed the presence of slightly agglomerated IOH-NPs. In addition, EDXS analysis was conducted on the cross-section with the bright particles and a peak at roughly 2.1 keV attributed to the Zr-L_α X-rays was observed. These findings suggest successful immobilization of the $[ZrO]^{2+}[FMN]^{2-}$

IOH-NPs in the PEGDA700 matrix. The peak at 1.15 keV attributed to the Ga-L_{α} X-rays originates from the FIB cutting process.

Subsequently, the O_2-responsive composite material was evaluated in practical applications following sensor performance and composition characterization.

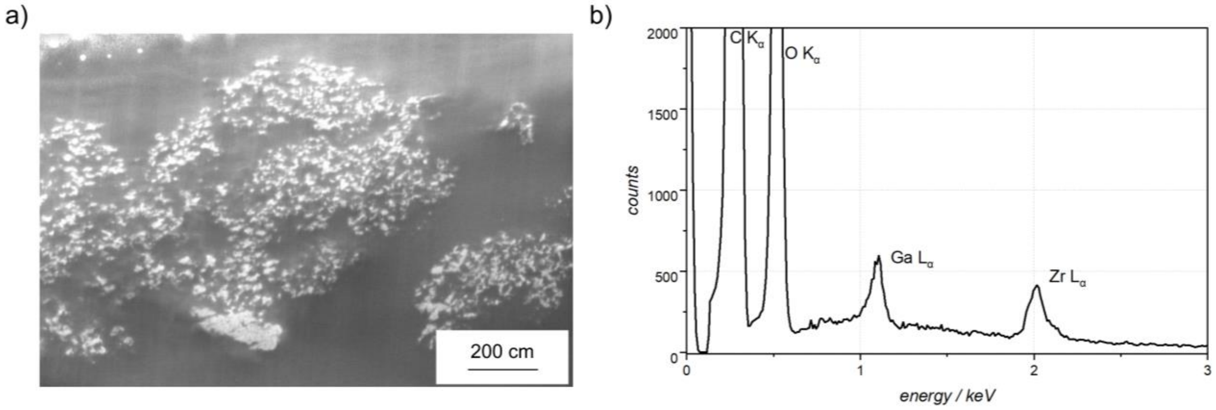

Figure 45. Characterization of the IOH-NPs within the composite material: **a)** SEM image of a composite-material cross-section containing 0.8 g L^{-1} IOH-NPs. **b)** EDXS analysis of the composite-material cross-section containing 0.8 g L^{-1} IOH-NPs.

7.5 Demonstration of O_2 Sensing Applications

Commercially available O_2 sensors are composed of platinum(II) (pentafluorophenyl) porphyrin or platinum(II) tetrabenzoporphyrin luminescence probes embedded into hydrophobic polymers.[194–196] These sensors can be glued on vessel walls and O_2 level can be determined using optical fibers to examine the O_2-dependent luminescence quenching. In general, the O_2 sensors can be used to monitor the O_2 level in packaging, bioreactors, and medical containers. However, these sensors often suffer from toxicity, metal complex leaching, and low photostability.[176–179] In addition, the manufacturing of the sensors is complex[175] and difficult to transfer into large-scale applications. Thus, the use of the FMN-based composite with 0.6 g L^{-1} IOH-NPs was studied for the non-invasive read-out of the O_2 level in two different scenarios. Initially, the reduced, 125 µm thick composite material was glued on the vessel wall of a vial using silicon glue (Figure 46a). By storing the vial under inert atmosphere no luminescence turn-on was observed, whereas under air the sensor showed intense luminescence, demonstrating the non-invasive use of the composite material to determine O_2 content in the headspace of pharmaceuticals or in bioreactors. Next, two reduced 125 µm thick sensors were placed into two different plastic bags and sealed under argon using clips (Figure 46b). The ingress of small amounts of O_2 was introduced by inserting a needle (Sterican®, G 20 × 1 ½, ø 0.90 × 40 mm, Ref. 4657519; B. Braun, Melsungen, Germany) once in one of the argon-filled plastic bags, inducing a leakage. Subsequently, the luminescence of both sensors in the plastic bags was investigated using fluorescence spectroscopy (Figure 46c). After 24 h, intense luminescence was observed for the sensor stored in the plastic bag with the leakage, whereas the sensor stored in the plastic bag without leakage did not exhibit luminescence after the course of 72 h. This highlights the use of the composite material as O_2 sensors in pharmaceutical and food packaging as well as, for instance, semiconductor storage. In comparison to read-out of commercially available O_2 sensors by optical fibers, the read-out of the composite-material luminescence can be visualized using a simple UV- or blue-light-emitting flashlight. This read-out method is advantageous for consumers to detect food spoilage or workers at GMP-lines to ensure high quality production of, for instance, pharmaceuticals or electronic devices.

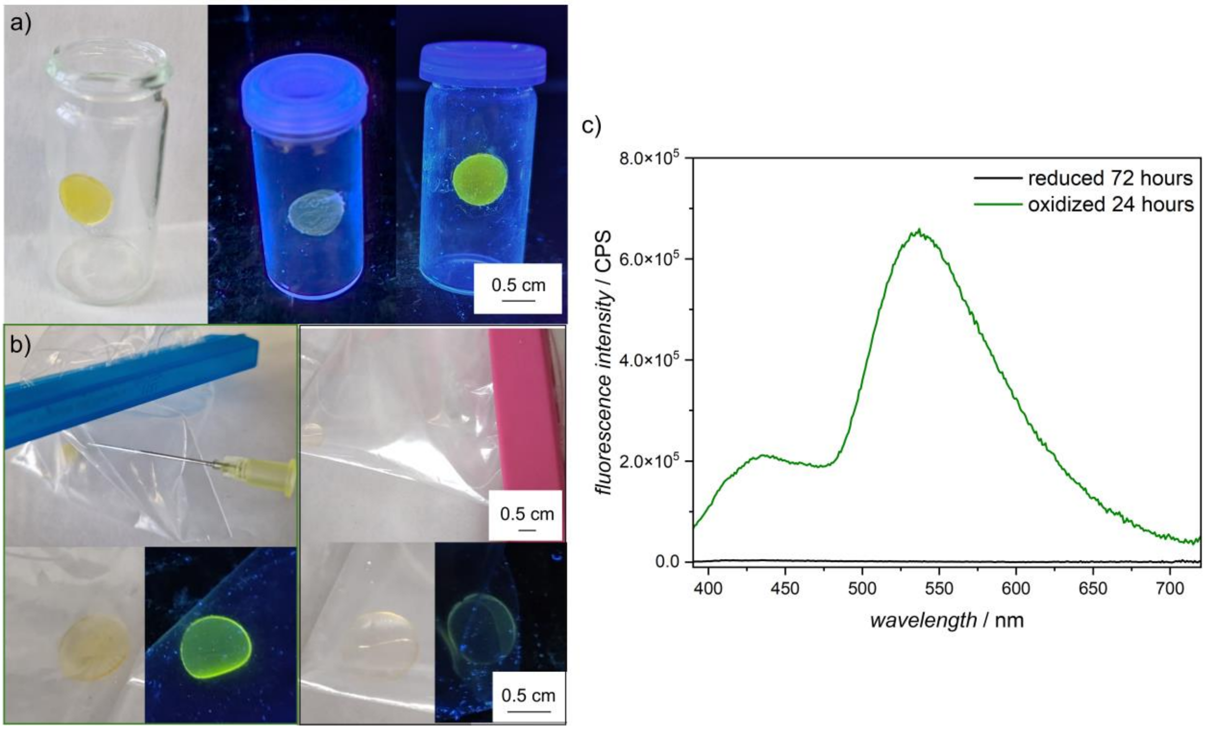

Figure 46. Assessment of the composite material in different applications: **a)** Demonstration of using composite-material-sensor to read-out O_2 levels, for instance, for headspace in pharmaceuticals by non-invasive measurements through the vessel wall. **b)** Two composite-material sensors assessed for 72 hours, one packaged in sealed in inert atmosphere (argon) and the other exposed to ambient atmosphere by punching a 0.9 mm big hole in the bag with a needle. After 72 hours in inert atmosphere, neither luminescence nor color-change were observed. However, after 24 hours with leakage, intense luminescence and color-change from transparent to yellow were observed. **c)** Fluorescence spectra for composite material after 72 hours in an inert atmosphere staying reduced (black) and 24 hours in O_2-rich atmosphere (green) exhibiting intense luminescence.

7.6 Conclusion

In the current chapter the synthesis of O_2-responsive $[ZrO]^{2+}[FMN]^{2-}$ IOH-NPs was introduced and their composition was validated by using FT-IR spectroscopy, TGA, PXRD, and EDXS. Initially, the O_2-dependent optical properties of the IOH-NPs, which are based on the oxidation state of FMN, were studied in detail, revealing an O_2-dependent color change and luminescence turn-on after FMN reduction by sodium dithionite. Next, composite materials of various shapes were fabricated by immobilizing the IOH-NPs in a PEGDA700 polymer matrix. Based on the fabrication method (spin-coating or DLP) composites with different geometries and thicknesses were fabricated. Subsequently, the effects of the IOH-NP concentration and the material thickness on the sensor performance were evaluated. The findings showed that by adjusting the IOH-NP loading and material thickness either rapid response times (thin film and low IOH-NP concentration) or good durability combined with high optical contrast (thick film and high IOH-NP concentration) were achieved. The presence of the IOH-NPs in the composite material was confirmed by SEM and EDXS analysis of the composite cross-section. Finally, the potential of the O_2 sensor was evaluated by demonstration of two different applications. First, the sensor was used to determine the O_2 level in the headspace of a vial, highlighting its relevance for medical and bioprocessing applications. Second, the composite was employed to examine O_2 leakage into plastic pouches, simulating food packaging or IV bags. In both studies the sensor did not exhibit luminescence turn-on or a color change under inert conditions for several days. However, intense luminescence and a color change from transparent to yellow were observed under air at ambient conditions within 24 h. In contrast to commercially available O_2 sensors, the herein introduced composite material is biocompatible, resistant to photodegradation and does not suffer from leaching. In addition, O_2 read-out can be easily performed using a UV- or blue-light-emitting flashlight, making the sensor highly user-friendly. This renders the O_2 sensor attractive both for consumers in supermarkets and pharmacies and for workers on industrial assembly lines.

CHAPTER 8: MULTI-RESPONSIVE COMPOSITE MATERIALS

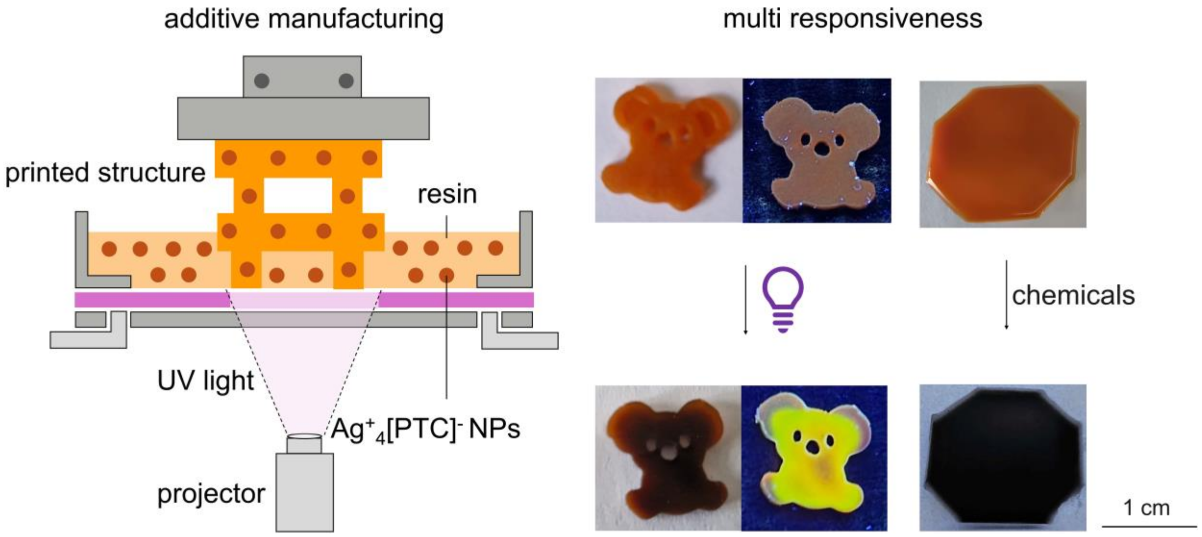

8.1 Inorganic-Organic Hybrid Nanoparticles

Perylene dyes are characterized by intense luminescence and high quantum yields of over 90 %.[197,198] A perylene derivative that can be used in the context of IOH-NPs is perylene-3,4,9,10-tetracarboxylic dianhydride (PTCDA). PTCDA exhibits high thermal and chemical stability[199] combined with high electron affinity of around 3.5 eV.[200,201] Furthermore, PTCDA undergoes π-stacking, which leads to high charge mobility, and thus PTCDA is used as an organic semiconductor in optoelectronics and thin-film devices.[202,203] The acid anhydride moieties of PTCDA are opened by alkaline treatment leading to perylene-3,4,9,10-tetracarboxylate ($[PTC]^{4-}$).[204] $[PTC]^{4-}$ shows outstanding photophysical properties. This includes strong absorption across a broad spectral range, high photostability, and intense luminescence.[205] In addition, strong π-stacking and aggregation-caused quenching (ACQ) were observed for $[PTC]^{4-}$ in the solid state, which result in fluorescence quenching.[204,206] Thus, $[PTC]^{4-}$ is suitable as a component for sensing applications of small molecules or metals with a luminescence off-on behavior. In the literature, $[PTC]^{4-}$ was already used to detect histamine,[119] carbonate,[204] or Sm^{3+}.[205]

The current chapter focuses on the preparation of $Ag^{+}_{4}[PTC]^{4-}$IOH-NPs and their complete characterization. Subsequently, the prepared IOH-NPs are used to fabricate composite materials using DLP, which adapt to various external stimuli (e.g., light). The responsiveness of the composite material is described in detail.

Synthesis

The synthesis (Figure 47) was adapted from the literature.[119] 26.0 mg (0.07 mmol) of PTCDA was dispersed in 100 mL water and heated to 85°C. The insoluble PTCDA was dissolved by converting it into the tetraanion upon addition of 1 mL NaOH (1 M). The alkaline treatment resulted in a bright yellow solution. Next, the pH was adjusted to pH 8 using HNO_3. Subsequently, 30.0 mg (0.18 mmol) of $AgNO_3$ were dissolved in 0.5 mL water and injected into the hot dye solution while vigorously stirring. The injection caused the solution to turn cloudy and orange. The formation of IOH-NPs is based on the insolubility of Ag_2CO_3 in water with a solubility product of $L = 8.5 \cdot 10^{-12}$.[207] The suspension was stirred for additional 10 minutes and then centrifuged three times (25.000 rpm, 15 min, 20 °C) by redispersing the precipitate in 10 mL water. This purification step was performed to remove the starting material and to yield the final $Ag^{+}_{4}[PTC]^{4-}$ IOH-NP suspension.

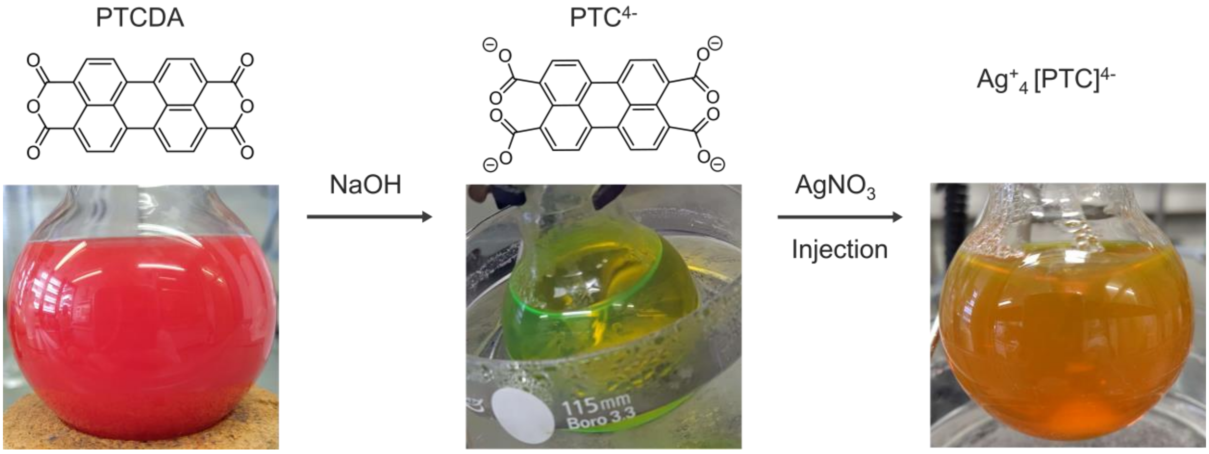

Figure 47. Synthesis of Ag$^+_4$[PTC]$^{4-}$ by using PTCDA as starting material and injection of AgNO$_3$.

Characterization

SEM analysis (Figure 48) of 100 particles reveals that the IOH-NPs have a mean length of 122±22 nm and display a nanorod-like morphology. Nanorod formation is ascribed to the π-stacking induced by the [PTC]$^{4-}$. A width of 20±5 nm was determined for the nanorods by SEM analysis, resulting in an aspect ratio of 6.1, which is typically considered elongated.[208]

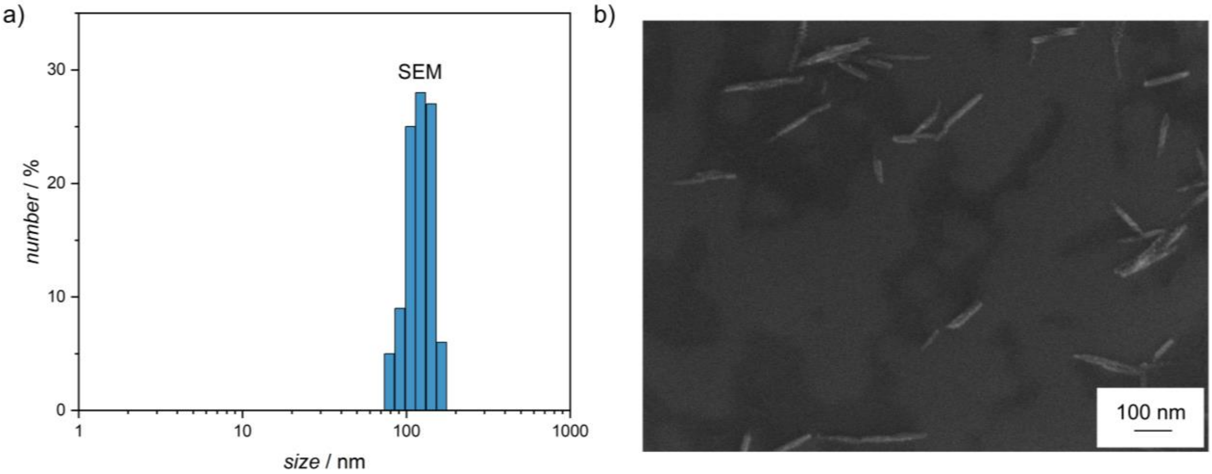

Figure 48. Size and morphology analysis of Ag$^+_4$[PTC]$^{4-}$ IOH-NPs: **a)** Size determined by SEM analysis and **b)** SEM image of Ag$^+_4$[PTC]$^{4-}$ nanorods.

The colloidal stability of the $Ag^+_4[PTC]^{4-}$ IOH-NPs was investigated by measuring the zeta potential at different pH (Figure 49). According to zeta-potential measurements, the IOH-NPs are colloidally stable from pH 4-9 with a zeta potential < -40 mV.

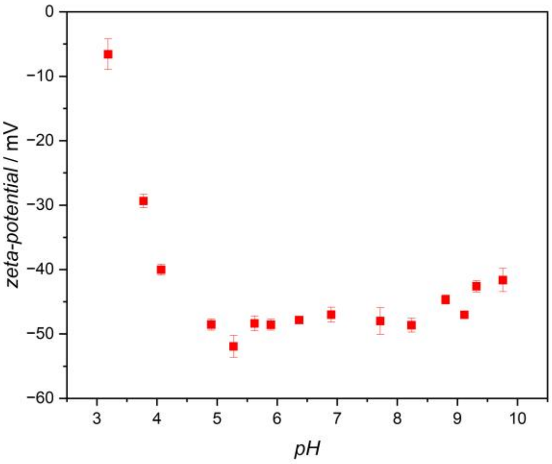

Figure 49. Zeta potential of $Ag^+_4[PTC]^{4-}$ IOH-NPs at different pH values.

The composition of $Ag^+_4[PTC]^{4-}$ IOH-NPs was investigated by a variety of different analytical methods (Figure 50). FT-IR spectra (Figure 50a) show the vibrations at $\tilde{\nu}$(C=O) = 1715 and 1660 cm^{-1}, which were observed for the anhydride moieties in the PTCDA reference, are absent. Instead, the IR spectrum of the IOH-NPs shows the asymmetric and symmetric vibrations at $\tilde{\nu}_{as}(COO^-)$ = 1554 cm^{-1} and $\tilde{\nu}_{sym}(COO^-)$ = 1351 cm^{-1}. The results reveal the presence of $[PTC]^{4-}$ in the IOH-NPs. Subsequently, TGA of the IOH-NPs (Figure 50b) was carried out to investigate the cation-to-anion ratio. First, a mass loss of 2.8 wt-% until 200°C was observed. This mass loss is attributed to residual water adsorbed on the IOH-NPs surface. At temperatures between 200 and 1200°C, the organic compounds are converted into CO_2 and H_2O with a total mass loss of 50.6 wt-%. The expected value for the mass loss of the organics of $Ag^+_4[PTC]^{4-}$ is 49.6 wt-% for a ratio of 1:1 to the cation. Thus, TGA confirms the cation-to-anion ratio of 1:1. The residue (46.6 wt-%) was analyzed by PXRD (Figure 50c), revealing the presence of metallic silver.

The decomposition of the IOH-NPs can be described with the following equation:

$$Ag^{+}_{4}[C_{24}H_{8}O_{8}]^{4-} + 22\ O_{2} \rightarrow 4\ Ag + 24\ CO_{2} + 4\ H_{2}O$$

The presence of silver, carbon and O_2 in the IOH-NPs is further confirmed by EDXS analysis of the IOH-NPs (Figure 50d).

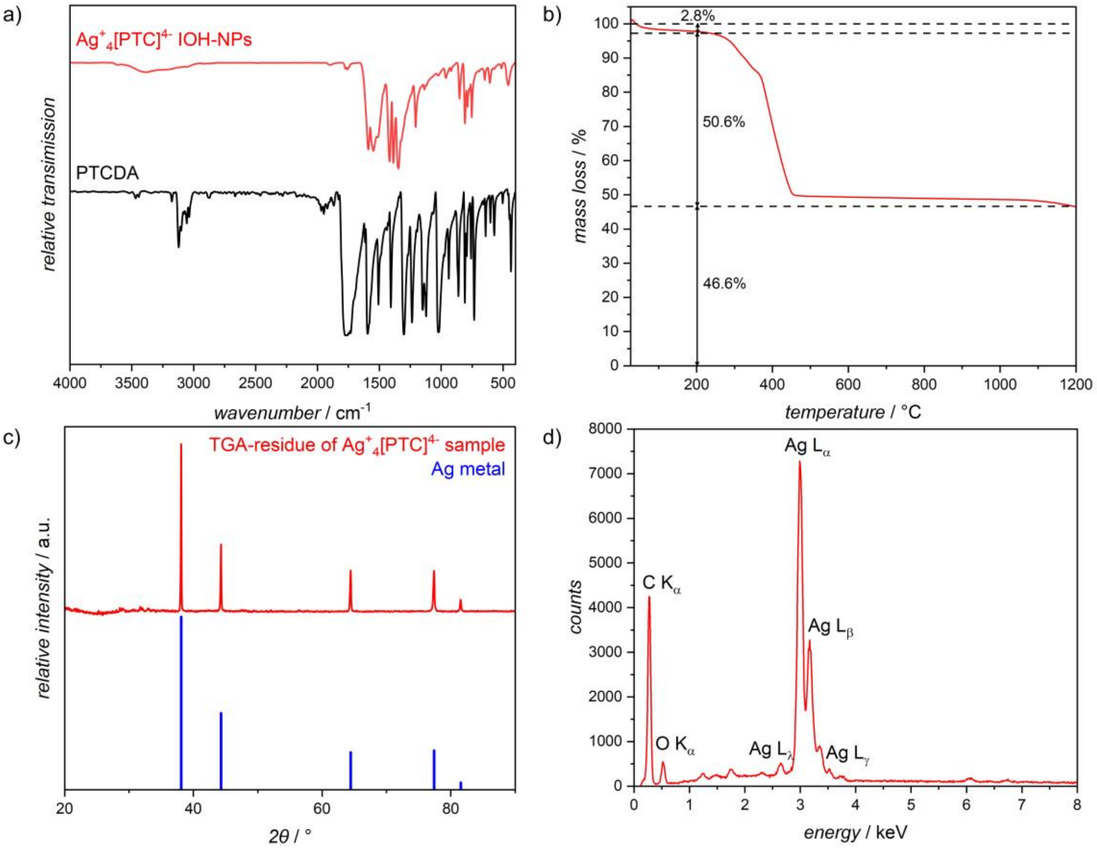

Figure 50. Determination of the composition of Ag$^{+}_{4}$[PTC]$^{4-}$ IOH-NPs. **a)** FT-IR spectra of IOH-NPs (red) and PTCDA dye (black). **b)** TGA spectrum for the IOH-NP combustion. **c)** PXRD of the TGA residue (red) and reference (blue). **d)** EDXS spectrum of the IOH-NPs.

EA of the IOH-NPs was carried out to confirm the composition of the IOH-NPs. The obtained amounts of C and H by EA of the Ag$^{+}_{4}$[PTC]$^{4-}$ IOH NPs (Table 4) are corrected for the content of adsorbed water of 2.8 wt-% (corrected: C 34.5 wt-%, H 0.9 wt-%) and match with a composition 4 Ag^{+} to [PTC]$^{4-}$ of 1:1 (theoretical: C 33.7 wt-%, H 0.9 wt-%).

Table 4. EA of $Ag^{+}_{4}[PTC]^{4-}$ IOH-NPs compared to the expected calculated values.

	C [wt-%]	**H [wt-%]**	**Mass loss [wt-%]**
Measurement	33.5	1.2	53.4
Corrected (-2.8 wt-% water)	34.5	0.9	52.1
Calculated	33.7	0.9	49.6

After confirming the successful synthesis and composition of the IOH-NPs by FT-IR spectroscopy, TGA, PXRD, and EDXS, their optical properties were studied. This characterization is essential to determine the read-out and responsiveness of the intended composite material.

The optical properties of the $Ag^{+}_{4}[PTC]^{4-}$ IOH-NPs (Figure 51) were investigated by fluorescence and UV-Vis spectroscopy. The π-stacking caused by the planar perylene anion is reflected by the nanorod-like morphology of the IOH-NPs. After synthesis, the luminescence of the IOH-NPs should be completely quenched due to the π-stacking and ACQ. As expected, luminescence quenching is confirmed by fluorescence spectroscopy of the IOH-NPs (Figure 51a) after synthesis upon excitation at 366 nm. Furthermore, the addition of sodium hydroxide until pH 12 results in the release of free $[PTC]^{4-}$ from the IOH-NPs. The release of $[PTC]^{4-}$ shows intense green emission at a wavelength of 485 and 516 nm upon excitation at 366 nm. This luminescence is characteristic of the $[PTC]^{4-}$. A color change from orange to bright green was observed for the decomposition of the IOH-NPs and studied by UV-Vis spectroscopy (Figure 51b). Upon decomposition, the peaks of the quenched IOH-NPs at 518 and 482 nm shift to 465 and 437 nm, corresponding to $[PTC]^{4-}$. The studies of the optical properties highlight the potential of the $Ag^{+}_{4}[PTC]^{4-}$ IOH-NPs for sensor applications based on luminescence off-on behavior.

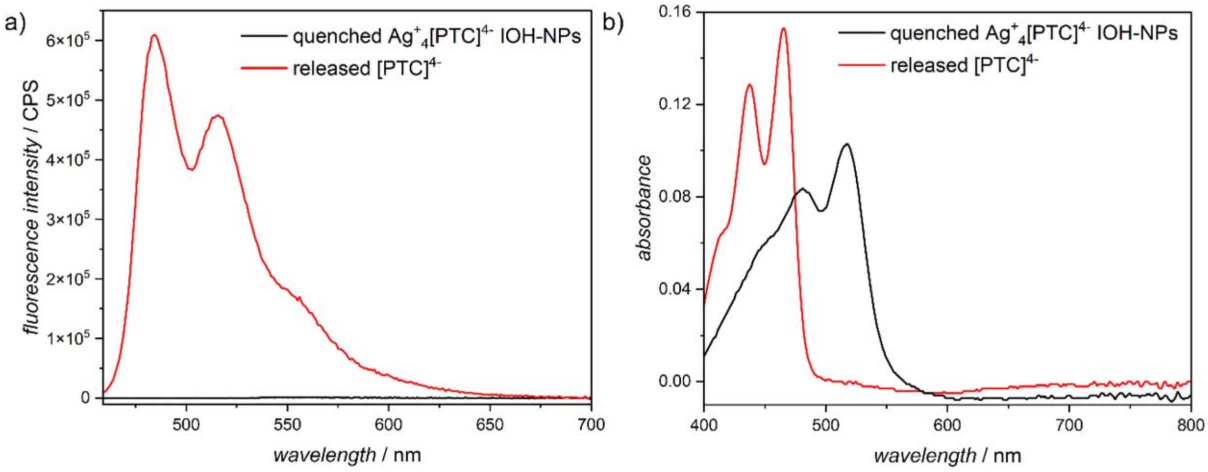

Figure 51. Characterization of the optical properties of the IOH-NPs: **a)** Fluorescence spectra of quenched $Ag^{+}_{4}[PTC]^{4-}$ IOH-NP suspension and released $[PTC]^{4-}$. **b)** UV-Vis spectra of quenched and $Ag^{+}_{4}[PTC]^{4-}$ IOH-NP suspension released $[PTC]^{4-}$.

After successful synthesis and characterization, the $Ag^{+}_{4}[PTC]^{4-}$ IOH-NP suspension was employed to prepare a composite-material ink for subsequent DLP.

8.2 Composite-Material Ink Design

The underlying curing mechanism of the composite-material photoresin is radical photopolymerization. Thus, the composite-material ink comprises a polymerizable monomer, a photoinitiator, and the $Ag^{+}_{4}[PTC]^{4-}$ IOH-NPs redispersed in water. PEGDA700 is chosen as a monomer for acrylate-based radical photopolymerization due to rapid polymerization kinetics, commercial availability, and good photoinitiator compatibility. In addition, PEGDA700 is hydrophilic and biocompatible,[192] ensuring stabilization of the IOH-NPs and allowing use of the fabricated composite material in medical applications. Moreover, no dissolution of the IOH-NPs was observed upon mixing the IOH-NP suspension with PEGDA700.

For the fabrication of a composite-material sensor based on luminescence turn-on, it is essential that the emission of the decomposed photoinitiator does not overlap with the green emission of $[PTC]^{4-}$ (450-600 nm), thereby ensuring high optical contrast and a simple read-out of the composite material. Likewise, as with the monomer, the photoinitiator should exhibit good water compatibility and biocompatibility. Targeting these prerequisites, LAP was selected as photoinitiator for the fabrication of the composite materials. LAP shows luminescence below 500 nm and is readily dissolved in water for straightforward composite-material ink preparation.[193] To account for shrinkage commonly observed for acrylate-based photoresins and to improve the stabilization of the IOH-NPs in the ink, 20 wt-% water were added to the ink. Detachment from the DLP-printer platform and incomplete composite fabrication were observed for water-to-monomer contents exceeding 1:5 caused by decreased crosslinking density and enhanced viscosity.

Next, the influence of the IOH-NP concentration was examined using fluorescence spectroscopy (Figure 52). During printing the generated radicals can react with the IOH-NPs, leading to dissolution of the IOH-NPs and causing intense luminescence of the $[PTC]^{4-}$ anion. However, complete luminescence quenching was observed for an IOH-NP loading of 1.5 g L^{-1} due to sufficient ACQ and π-stacking.[204,206] This finding suggests that the IOH-NPs do not react with the decomposed photoinitiator.

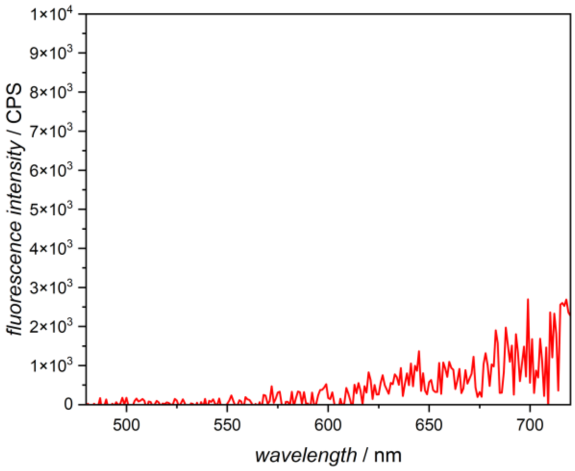

Figure 52. Fluorescence spectra recorded a composite material composed of 1.5 g L^{-1} IOH-NPs with an excitation wavelength of 444 nm.

The composite-material ink for DLP was prepared by mixing 10 mL of PEGDA700 with 1.5 g L^{-1} of IOH-NPs dispersed in 2 mL of water. Subsequently, 0.1 wt-% of LAP was dissolved in water, added to the mixture and vigorously stirred overnight. The final composite-material ink remains stable for several months when stored in the dark.

The following chapter focuses on the fabrication of responsive composite material and investigation of their responsiveness using the optimized composite-material ink.

8.3 Composite-Material Fabrication and Responsiveness

Using the composite-material ink, multi-responsive materials were fabricated by DLP (Figure 53). This AM method was employed to fabricate 3D structures with high resolution and high surface area to achieve improved sensor sensitivity and enhanced response times.

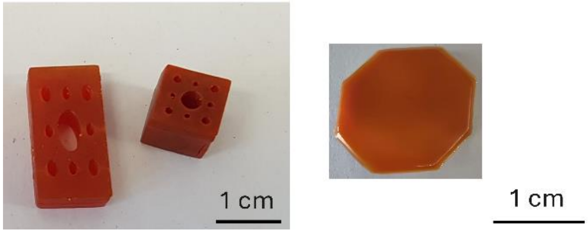

Figure 53. Fabricated composite materials with various shapes using DLP.

The composite materials exhibit intense green emission turn-on in response to external stimuli, which is based on the $Ag^+_4[PTC]^{4-}$ IOH-NPs incorporated into the PEGDA700 matrix. The switching from completely quenched luminescence to intense fluorescence emission was employed in sensor applications. In the past, Ag^+_4 $[PTC]^{4-}$ IOH-NP suspensions were used as fluorescent sensors to determine the histamine content in blood serum.[119] Histamine is released into the blood during an allergic shock and the histamine level rises from 0.01 µmol L^{-1} up to 10 µmol L^{-1}.[209,210]

Initially, the luminescence of the IOH-NPs is quenched in the solid state. In the presence of histamine, complexation of the silver cations occurs, resulting in the dissolution of the IOH-NPs and release of $[PTC]^{4-}$, showing intense luminescence. The fluorescence intensity depends on the amount of released $[PTC]^{4-}$, which correlates with the concentration of histamine. For instance, intense luminescence turn-on was observed at histamine concentration of 100 µmol L^{-1} upon addition of histamine to an $Ag^+_4[PTC]^{4-}$ IOH-NP suspension, and an increase in fluorescence by a factor of 180 was observed.[119] The disadvantage of this method is that the dissolved $[PTC]^{4-}$ is released into the blood serum, which is highly red-stained, and thus the luminescence read-out is challenging. This challenge can be overcome by using the prepared composite materials, which can be physically removed from the blood serum, and residual blood serum can be rinsed off with water. Subsequently, the optical properties of the composite material can be checked for green fluorescence emission using a blue-light-emitting LED. Initially, histamine sensing using the composite materials (Figure 53) was studied by immersing the objects in a 10 µM histamine solution for 5 min. However, after the 5 min, no fluorescence of the washed composite material was observed. Instead, the histamine solution showed intense green emission. This is caused by the uncharged surface of the composite, which cannot bind the $[PTC]^{4-}$. These findings revealed that a positive surface charge of the composite material is required to enable effective fluorescence-based sensing of histamine. As a result, the surface charge of the composite materials was adjusted by the addition of 1 wt-% N-(3-dimethylaminopropyl)methacrylamide (DMAPAm) into the composite-material ink, leading to a positive surface charge. The positive surface charge originates from the basic tertiary amine, which is protonated at a pH below 9.0. In addition, the composite-material matrix is a hydrogel that enables protonation of the tertiary amine.[211] Repeating the same histamine-sensing test with the modified composite materials, intense luminescence from the composite-material surface was detected (Figure 54a). Furthermore, no reaction between IOH-NPs and small quantities of DMAPAm was observed, highlighting the use of DMAPAm to improve adhesion of negatively charged molecules. Subsequently, the use of the composite material in histamine sensing was assessed again by immersing composite materials in different amounts of histamine (10 and 100 µmol L^{-1}) for 10 min. A 100 µmol L^{-1} concentration of histamine corresponds to a severe allergic shock. For the histamine concentration of 100 µmol L^{-1} an intense luminescence turn-on was recorded using fluorescence spectroscopy (Figure 54b). In addition, the histamine sensing using the composite material is compared to the responsiveness of the IOH-NPs. The fluorescence spectra (Figure 54c) were recorded for the $Ag^{+}_{4}[PTC]^{4-}$ IOH-NP suspension after 2 min using an excitation wavelength of 444 nm for histamine concentrations ranging from

0.1-100 µmol L^{-1}. Intense luminescence turn-on was observed at histamine concentrations of 10 and 100 µmol L^{-1}. At histamine concentrations lower than 0.1 µmol L^{-1}, the emission remained quenched. Comparing the results for the histamine sensing using the composite materials and the IOH-NP suspension, a sensitivity loss and longer response times were observed by incorporating the IOH-NPs in the PEGDA700 matrix. This is supported by the reduced emission intensity of the composite material after 10 min in histamine, compared with the IOH-NP suspension. For instance, the composite material in 10 µmol L^{-1} histamine showed a fluorescence intensity loss of around 60 % compared to the IOH-NP suspension.

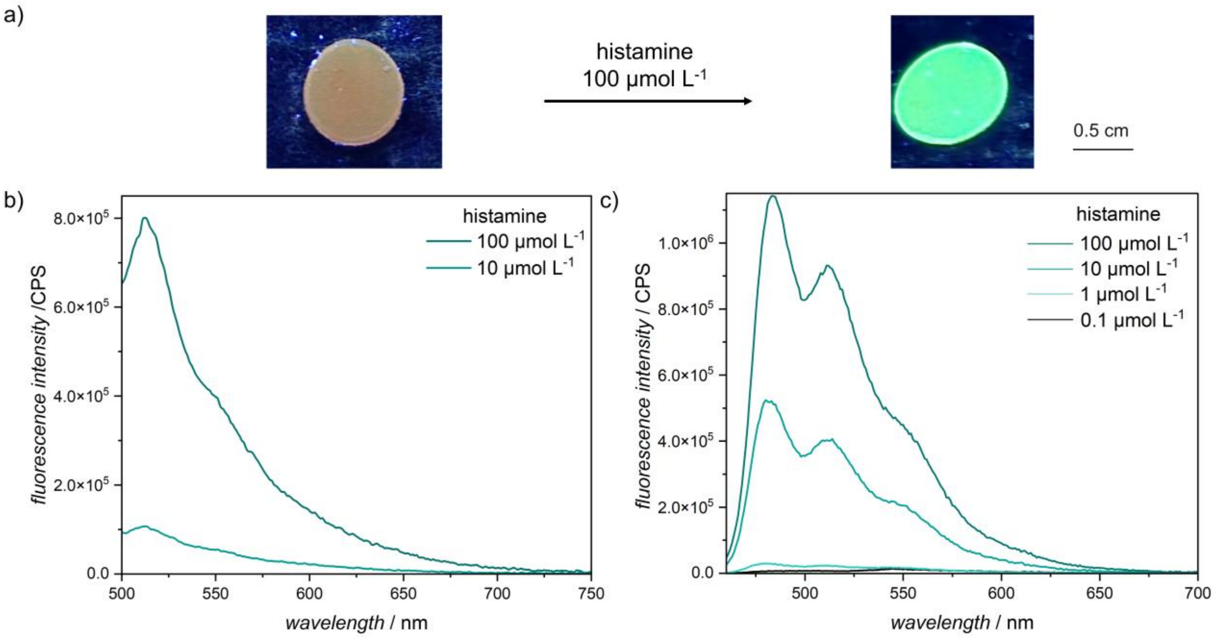

Figure 54. Histamine sensing using different concentrations of histamine in water to achieve the release of [PTC]$^{4-}$: **a)** Fluorescence images of composite material before and after immersion in 100 µmol L^{-1} histamine, **b)** release of [PTC]$^{4-}$ from composite material and **c)** release of [PTC]$^{4-}$ from IOH-NP suspension.

Subsequently, the histamine sensing in blood serum was examined using the composite materials. When the composite material was immersed in a solution containing histamine and blood serum, intense luminescence was observed. However, the composite material also showed intense luminescence when immersed in blood serum in the absence of histamine. The luminescence turn-on can be caused by the chloride anions contained in the blood serum,[212] which form insoluble silver chloride, leading to the release of $[PTC]^{4-}$.[207] Therefore, the composite material was immersed in a 10 μmol L^{-1} sodium chloride solution, and the luminescence of the composite material was recorded using fluorescence spectroscopy. Intense luminescence was observed for the composite material (Figure 55a). Given this limitation, silver nitrate was added to the blood serum prior to the histamine sensing to remove chloride anions. The composite material also showed intense luminescence in the blood serum in the absence of chloride anions. This suggests that cysteine and other reducing agents[212] in blood serum cause the release of $[PTC]^{4-}$ upon reduction of silver cations to metallic silver. The reduction of the IOH-NPs incorporated in the composite material was examined using sodium thiosulfate, which induces intense luminescence (Figure 55b) and a color change (Figure 55c). These results show the lack of responsiveness and sensitivity of the composite material in histamine sensing. Consequently, the focus of the sensing application was redirected toward responsiveness to other external stimuli.

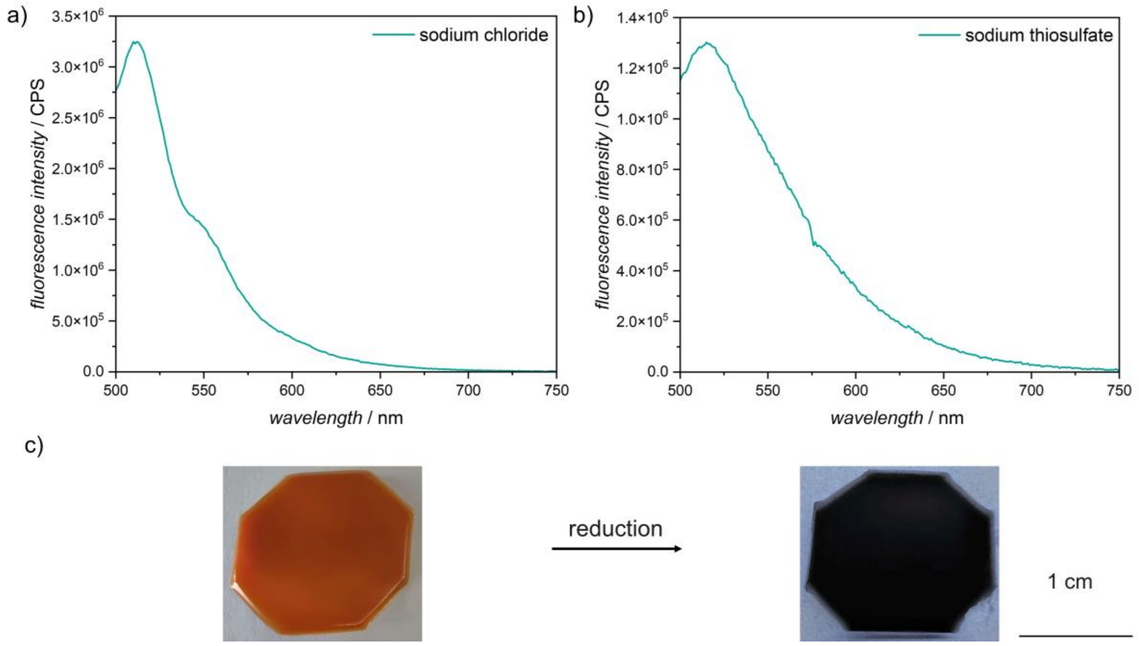

Figure 55. Fluorescence spectra recorded at 466 nm excitation wavelength for the luminescence turn-on of the composite material by addition of: **a)** sodium chloride and **b)** sodium dithionite. **c)** Images of a composite material before and after reduction with sodium dithionite.

Generally, silver cations can also be reduced to metallic silver by irradiation with, for example, UV light.[213,214] Thus, the responsiveness of the composite material to light was studied. In particular, UV light sensing represents an interesting application, as UV light radiation can induce both DNA damage[215] and material deterioration.[216,217] For instance, UV-A light radiation (315-400 nm) can generate reactive oxygen species (ROS), which attack DNA and can lead to mutations.[218,219] In addition, UV light radiation causes dermal photoaging[220] and severe eye damage.[221,222] Moreover, continuous UV irradiation of polymer and composite materials induces material degradation, discoloration or yellowing, and alters mechanical and optical properties.[223] To test the UV responsiveness of the composite material, a sensor was placed in a distance of 1.5 cm to a 385 nm-emitting LED using a voltage of 12 V and a current of 0.03 A. Within 10 s, the composite material turned dark brown/black indicating a successful reduction of Ag^+ (Figure 56a). Subsequently, the composite material was placed under a 366 nm-emitting UV lamp to investigate the luminescence of the sensor. An intense green/yellow emission (Figure 56b) was observed for the composite material. Further UV light irradiation resulted in a black color of the composite material, showing no luminescence. The same test was conducted using a 535 nm-emitting LED (Lumitronix, Cree XP-E2 SMD-LED, 122lm, green) using the same parameters for the irradiation. After 5 min of irradiation, no colorimetric change was observed. Using a 366 nm-emitting UV lamp, the composite material did not exhibit any luminescence (Figure 56a). Finally, the composite material was exposed to sunlight (KIT, Germany) for seven days (Figure 56c). During this period, a colorimetric change from bright orange to brown/black was observed. These findings suggest the use of the composite material as a UV sensor enabling UV light detection by colorimetric change from bright orange to dark brown/black and a fluorometric change based on luminescence off-on behavior.

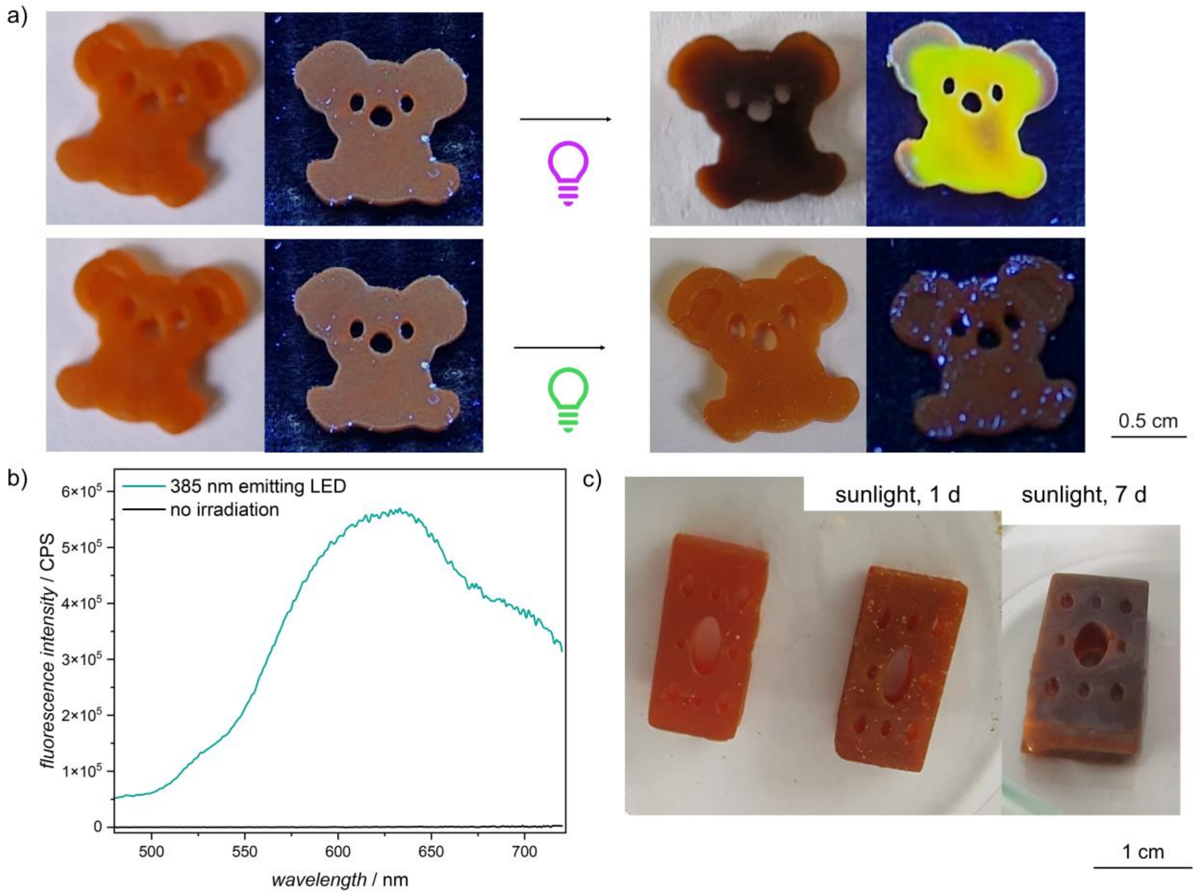

Figure 56. Light-sensitive optical properties of the composite materials: **a)** UV light and green light irradiation (385, 535 nm) of a composite-material koala with luminescence images before and after irradiation. **b)** Fluorescence spectra recorded for the composite material, which was irradiated using a 385 nm-emitting LED and an excitation wavelength of 444 nm. **c)** Colorimetric change of the composite material upon exposure to the sun for a total of seven days.

8.4 Conclusion

In the current chapter, the successful preparation of $Ag^{+}_{4}[PTC]^{4-}$ IOH-NPs is reported, and the composition of the IOH-NPs was validated using FT-IR spectroscopy, TGA, PXRD, and EDXS. The prepared IOH-NPs exhibit ACQ, as well as π-stacking, which results in complete luminescence quenching. By using the IOH-NPs for DLP to fabricate composites, materials exhibiting multi-responsiveness to external stimuli are prepared. The responsiveness of the composite materials originates from reactions targeting Ag^+ and leading to the release of $[PTC]^{4-}$, which exhibits intense green fluorescence emission. Examples for these reactions, demonstrated in the current chapter, are the complexation of the Ag^+ by histamine and the reduction of Ag^+ using UV light irradiation. Histamine is released by the human body in response to an allergic reaction. Initial tests of the histamine sensing using the composite material resulted in the release $[PTC]^{4-}$. However, the released $[PTC]^{4-}$ did not bind to the composite material surface. Hence, the composite-material surface was adjusted using small quantities of DMAPAm, leading to a positively charged surface able to bind some of the released $[PTC]^{4-}$. As a result, the composite material showed intense luminescence after being immersed in a 100 µmol L^{-1} histamine solution. Subsequently, the histamine sensing in blood serum using the composite material was investigated, which showed intense green emission in the absence of histamine. The chloride and reducing agents contained in the blood serum were identified to cause the luminescence turn-on. Attempts to remove all these components were unsuccessful. Therefore, a new promising avenue of UV light sensing was explored.

Finally, the composite material exhibits responsiveness to UV light causing the reduction of Ag^+. This reduction is accompanied by a colorimetric change from bright orange to dark brown/black, as well as an intense luminescence turn-on, leading to a green/yellow fluorescence emission. Furthermore, the composite material did not show any changes of the optical properties after irradiation with visible light. In a proof-of-concept test, the composite material was placed into direct sunlight for the duration of seven days, which resulted in a color change. Depending on the exposure time, the brown/black color intensified. Consequently, the herein prepared composite material shows great potential for use as a UV sensor.

CHAPTER 9: INORGANIC-ORGANIC HYBRID NANOPARTICLES FOR RECYCLABLE PHOTO-SENSITIVE COMPOSITES

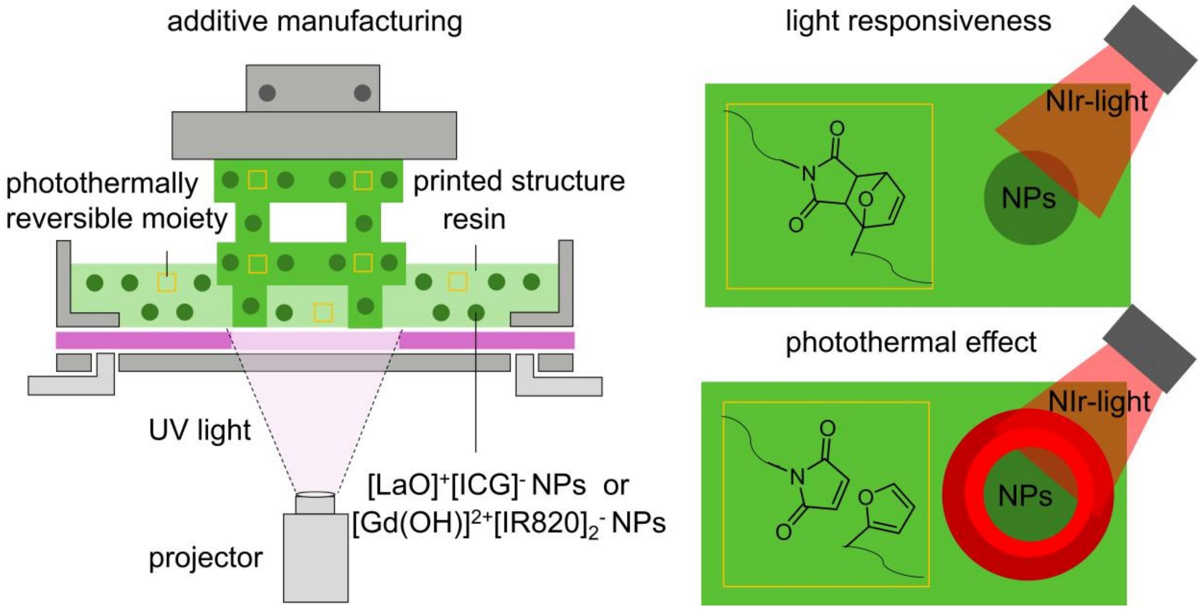

Photo-responsive materials change their chemical, mechanical, or physical properties upon light exposure. Light as a trigger is precise and offers excellent spatiotemporal control to induce swelling/deswelling, deformation, and degradation.[111,224] Photo-responsiveness is achieved by modifying commonly used monomers/oligomers with, for instance, spiropyrans[225] or azobenzene moieties[226,227] that undergo reversible photodissociation or cis-trans isomerization when exposed to light, respectively. Photo-responsive materials are utilized in applications ranging from controlled drug release[228,229] to shape memory.[230,231] In particular, photo-induced degradation of a polymer network is attractive, opening new avenues to recyclable, self-healing structures. One approach for the fabrication of such materials is to fuse functional NPs such as Au NPs with polymers that exhibit reversible crosslinks.[228,232] Au NPs can be used to convert light into heat, which is subsequently used to open the crosslinks, leading to degradation. The reversible crosslinks can for instance be formed by using furan and maleimide derivatives to form DA adducts, which undergo retro-DA at elevated temperatures (80-120 °C).[233] However, using Au NPs to trigger the retro-DA can be challenging. First, Au NPs exhibit surface plasmon resonance in the visible region, which can overlap with the printer's cure wavelength. In addition, the Au NPs can scatter the light used for polymer solidification, which can reduce the cure depth and resolution. Thus, in the current chapter, the synthesis and characterization of IOH-NPs showing light-to-heat conversion are introduced. Besides utilizing the IOH-NPs as a trigger to induce retro-DA, they show potential for bioimaging and tumor treatment due to sensitivity to their near-infrared light (NIR).

9.1 Indocyanine Green-Based Inorganic-Organic Hybrid Nanoparticles

Indocyanine green (ICG) is a NIR-emitting cyanine dye often used in biomedical imaging, and in photothermal or photodynamic therapy.[234] The application of ICG in medicine originates from the fact that NIR light penetrates biological tissue more effectively than visible light.[235] Thus, ICG can be used for visualization and cancer treatment due to high laser penetration of NIR lasers deep in the tissue. In addition, irradiation of ICG with NIR light leads to heat and ROS generation, which is exploited to kill tumor cells.[234] However, the application of free ICG is limited by aggregation, photobleaching, and dye degradation. ICG can be incorporated into NPs to mitigate the limitations and improve chemical and photostability. In addition, NPs or IOH-NPs can be used as a platform to incorporate drugs or antibodies for enhanced tumor treatment and targeting. For instance, $[GdO]^+[ICG]^-$ IOH-NPs were prepared and their utilization as a multimodal contrast agent for *in-vitro* and *in-vivo* experiments was demonstrated.[18] In these studies, the ICG anion provided fluorescence and photoacoustic contrast in the NIR range. Fluorescence imaging is characterized by precise molecular tracking, whereas photoacoustic imaging offers deep-tissue resolution.

Synthesis

9.8 mg ICG (ICG, 0.01 mmol) were dissolved in 25 mL water and stirred for 15 minutes. 4.3 mg (0.02 mmol) of $LaCl_3 \cdot 7H_2O$ were dissolved in 0.5 mL water and rapidly injected into the dye solution with vigorous stirring. Upon injection the dark green solution became cloudy. The suspension was stirred for two minutes and subsequently centrifuged three times (25.000 rpm, 15 min, 20 °C). The final $[LaO]^+[ICG]^-$ IOH-NP suspension (Figure 57) was obtained after redispersing the IOH-NPs in water using an ultrasonic bath, followed by the addition of 0.5 mL of 0.1 M NaOH to adjust the pH to 7.

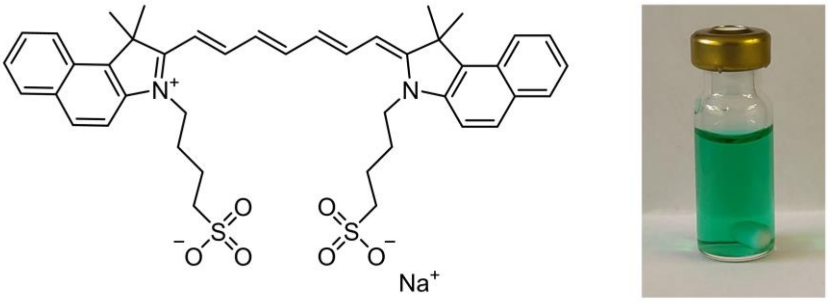

Figure 57. Structure of ICG and image of the final prepared $[LaO]^+[ICG]^-$ IOH-NP suspension.

Characterization

DLS measurements (Figure 58a) exhibit a broad size distribution for the IOH-NPs in water with a mean hydrodynamic diameter of 70±31 nm. SEM analysis (Figure 58a and b) of 100 particles shows spherical IOH-NPs with a mean size of 46±9 nm, indicating the successful synthesis of a nanomaterial. The difference in particle size determined by DLS and SEM analysis originates from the hydration shell surrounding the IOH-NPs. The hydration shell is only measured in the DLS analysis of the IOH-NP suspension.

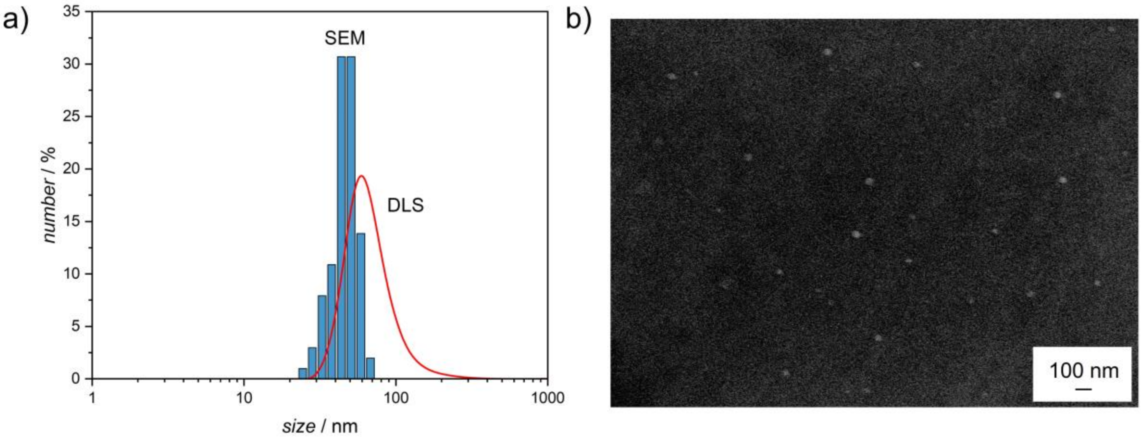

Figure 58. Size and morphology analysis of $[LaO]^+[ICG]^-$ IOH-NPs: **a)** Size distribution by DLS and SEM analysis and **b)** SEM image of spherical $[LaO]^+[ICG]^-$.

The colloidal stability of the $[LaO]^+[ICG]^-$ IOH-NP suspension was determined by measuring the zeta potential at different pH values (Figure 59). According to zeta-potential measurements, the IOH-NPs exhibit colloidal stability for pH 4.5–8 with zeta potentials < -30 mV. At pH 8, higher errors in the zeta-potential measurement were observed due to the beginning of dissolution of the IOH-NPs.

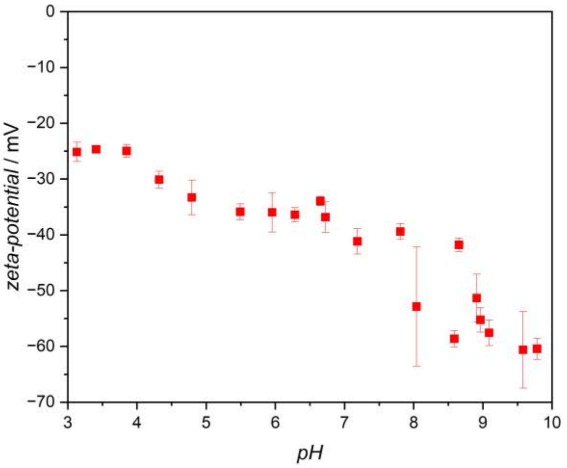

Figure 59. Zeta potential of $[LaO]^+[ICG]^-$ IOH-NPs at different pH values.

The composition of $[LaO]^+[ICG]^-$ IOH-NPs was investigated using different analytical methods (Figure 60). FT-IR spectroscopy was employed to confirm the presence of ICG within the IOH-NPs. The FT-IR spectrum (Figure 60a) of the IOH-NPs exhibits the same characteristic vibrations as the free dye, confirming the presence of ICG. The FT-IR spectra show the stretching vibration $\tilde{\nu}$(O-H) = 3600-2500 cm^{-1} caused by residual water adsorbed on the NP surface. Vibrations $\tilde{\nu}$(C–H): 3000 and 2800 cm^{-1} are attributed to the C_{aryl}-H and $C_{aliphatic}$-H vibrations. In addition, the vibrations at $\tilde{\nu}$(SO_3): 1600-1300 cm^{-1}, $\tilde{\nu}$(SO_3): 1250-950 cm^{-1} and δ(SO_3): 650 cm^{-1} were observed. Subsequently, TGA of the IOH-NPs (Figure 60b) was carried out to investigate the cation-to-anion ratio. Initially, a mass loss of 6.8 wt-% until 190°C was observed, which is attributed to residual water. At temperatures between 190 and 1200°C the organic compounds are converted into CO_2, H_2O, N_2 and SO_2 with a total mass loss of 90.3 wt-% (corrected for residual water). For a 1:1 cation-to-anion ratio, a mass loss of 85.0 wt-% for the organic components is expected. This indicates the 1:1 cation-to-anion ratio within the IOH-NPs. The residue with a total weight of 9.0 wt-% was analyzed by PXRD. The PXRD pattern (Figure 60c) of the residue revealed the presence of La_2O_3 and $(LaO)_2SO_4$. The decomposition of the IOH-NPs can be described with the following equation:

$$6\,[LaO]^+[C_{43}H_{47}N_2O_6S_2]^- + 325\,O_2 \rightarrow$$

$$La_2O_3 + 2\,(LaO)_2SO_4 + 258\,CO_2 + 141\,H_2O + 6\,N_2 + 12\,SO_2$$

The presence of lanthanum, sulfur, carbon and O_2 in the IOH-NPs are further confirmed by EDXS analysis of the IOH-NPs (Figure 60d).

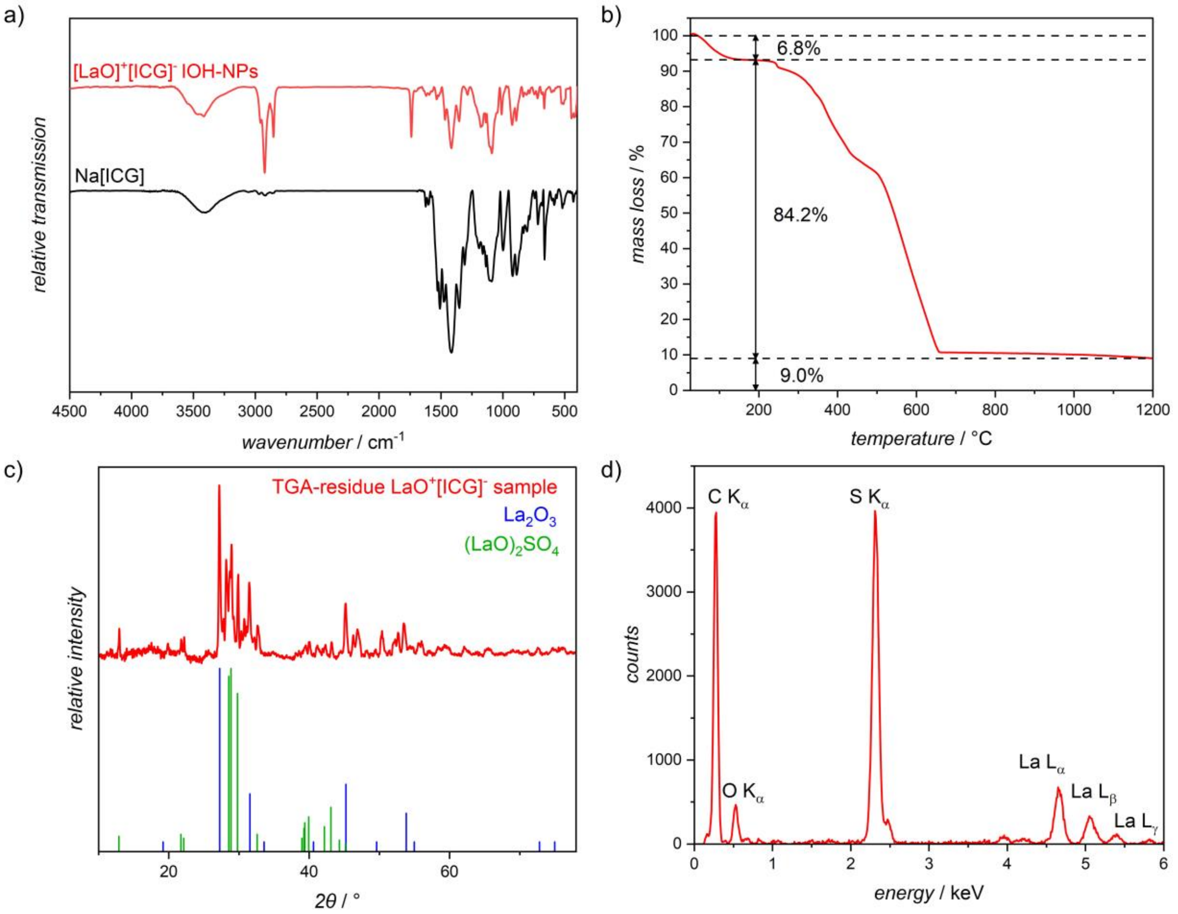

Figure 60. Determination of the composition of $[LaO]^+[ICG]^-$ IOH-NPs. **a)** FT-IR spectra of IOH-NPs (red) and Na(ICG) (black). **b)** TGA spectrum for the IOH-NP combustion. **c)** PXRD of the TGA residue (red) and references (blue and green). **d)** EDXS spectrum of the IOH-NPs.

The obtained amounts of C, H, N and S by EA of the $[LaO]^+[ICG]^-$ IOH NPs (Table 5) are corrected for the content of adsorbed water 6.8 wt-% (corrected: C 58.4 wt-%, H 5.1 wt-%, N 2.0 wt-%, S 7.0 wt-%) and match with a composition $[LaO]^+[ICG]^-$ of 1:1

for the inorganic cation and organic anion in the IOH-NPs (theoretical: C 57.0 wt-%, H 5.2 wt-%, N 3.1 wt-%, S 7.1 wt-%).

Table 5. EA and TGA of $[LaO]^+[ICG]^-$ IOH-NPs compared to the expected calculated values.

	C [wt-%]	H [wt-%]	N [wt-%]	S [wt-%]	Mass loss [wt-%]
Measurement	54.4	5.5	1.8	6.5	91.0
Corrected (-6.8 wt-% water)	58.4	5.1	2.0	7.0	90.3
Calculated	57.0	5.2	3.1	7.1	85.0

The optical properties of the $[LaO]^+[ICG]^-$ IOH-NP suspension were examined using fluorescence spectroscopy. Upon excitation of the IOH-NPs with white light, red emission was observed (Figure 61a). In addition, excitation and emission spectra of the IOH-NPs (Figure 61b) were recorded. According to the excitation spectrum, the absorption maximum was observed at 773 nm. The emission spectrum shows an emission maximum at 824 nm.

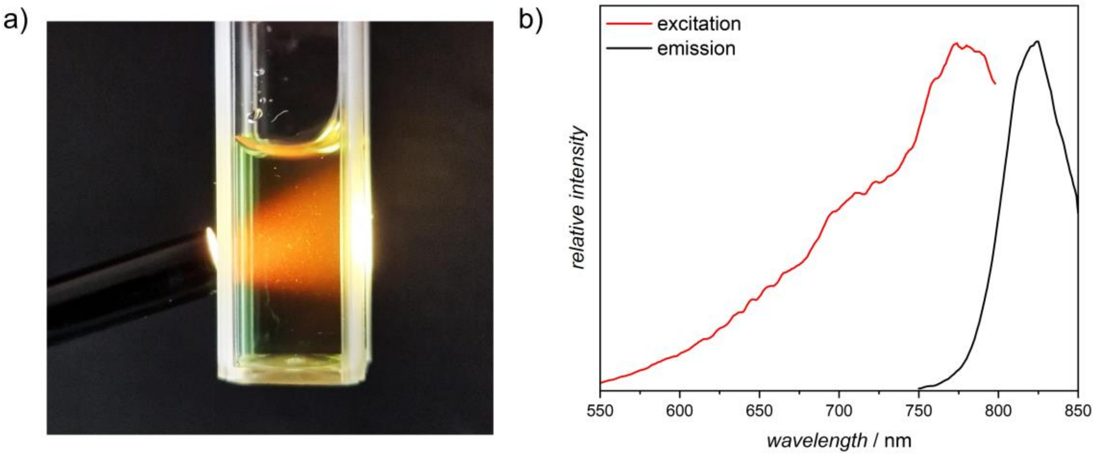

Figure 61. Luminescence properties of the IOH-NPs: **a)** Luminescence of $[LaO]^+[ICG]^-$ IOH-NP suspension upon white light excitation. **b)** Excitation and emission spectra for $[LaO]^+[ICG]^-$ IOH-NPs.

9.2 New Indocyanine Green-Based Inorganic-Organic Hybrid Nanoparticles

New indocyanine green (IR-820, Figure 62) is a cyanine dye with great resemblance to ICG. Like ICG, IR-820 is utilized for tumor visualization and photothermal therapy due to negligible toxicity. Furthermore, IR-820 exhibits enhanced photostability and improved *in-vivo* and *in-vitro* stability in contrast to ICG. As for the optical properties, IR-820 exhibits red-shifted, less pronounced, concentration-dependent absorption and luminescence. The potential use of IR-820 in photothermal therapy has been investigated.[236] A 500 µg mL^{-1} IR-820 solution was irradiated for 10 min with a 1.5 W cm^{-2} 793 nm CW laser. The irradiation was converted into heat with a temperature exceeding 90 °C. As a control, water was irradiated using the same parameters, which led to negligible temperature increase.

Synthesis

9.8 mg (0.01 mmol) of IR-820 were dissolved in 25 mL degassed water. The pH of the solution was adjusted to pH 7 using sodium hydroxide. Subsequently, 3.9 mg (0.01 mmol) of $GdCl_3 \cdot 6H_2O$ were dissolved in 0.5 mL water and rapidly injected into the dye solution while vigorous stirring. The injection caused the green solution to become cloudy. The suspension was stirred for additional 2 minutes. Afterwards the crude IOH-NP suspension was purified in three centrifugation steps (25,000 rpm, 15 min, 25°C) to separate the final IOH-NPs from the starting material. In addition, 0.2 mL of 0.1 M sodium hydroxide were added to the final IOH-NP suspension to adjust for pH 7 (Figure 62).

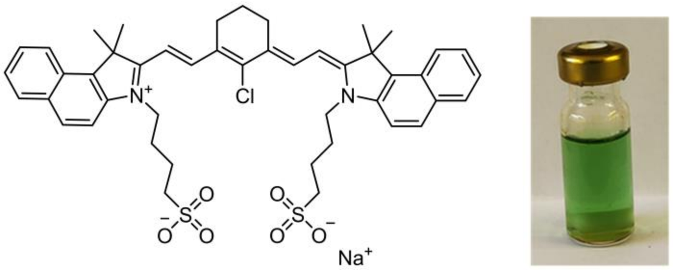

Figure 62. Structure of IR-820 and image of the final prepared $[GdO]^+[IR820]^-$ IOH-NP suspension.

Characterization

After synthesis, the size and morphology of the $[GdO]^+[IR820]^-$ IOH-NPs were examined using DLS and SEM analysis (Figure 63). Both analytical methods show nanosized particles. DLS measurements of the IOH-NPs in water show a broad size distribution with a mean hydrodynamic diameter of 95±32 nm (Figure 63a). In addition, SEM analysis (Figure 63a and b) of 100 particles shows spherical NPs with a mean size of 98±28 nm. The particle size determined by DLS is in good agreement with that from SEM analysis.

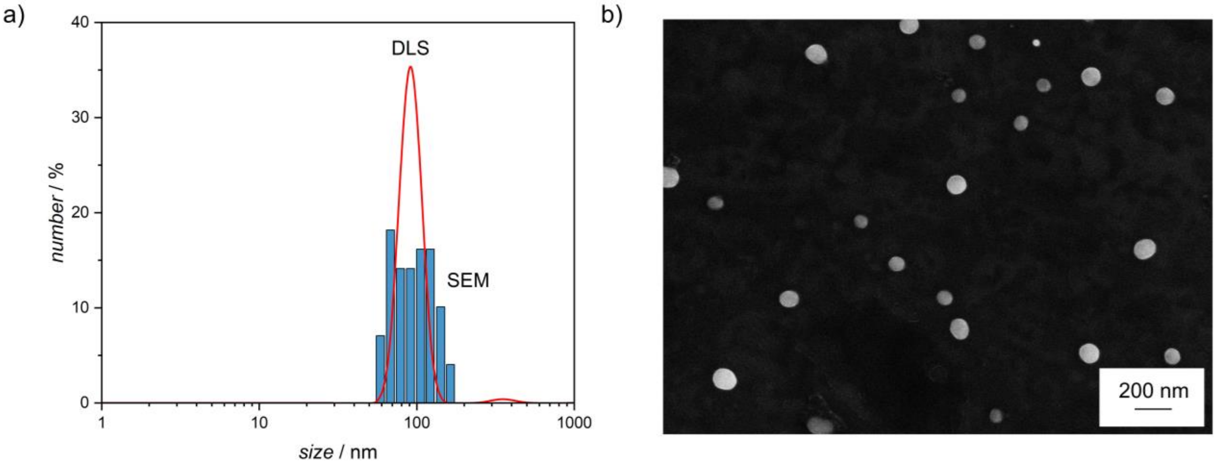

Figure 63. Size and morphology analysis $[GdO]^+[IR820]^-$ IOH-NPs. **a)** Size determined by DLS and SEM analysis and **b)** SEM image of spherical $[GdO]^+[IR820]^-$.

The intrinsic charge stabilization of the $[GdO]^+[IR820]^-$ IOH-NP suspension was determined by measuring the zeta potential at different pH values (Figure 64). The zeta potential quantifies the surface charge of the IOH-NPs, which are stabilized by their intrinsic charge. According to zeta-potential measurements, the IOH-NPs exhibit colloidal stability for pH 4.5–8 with zeta potentials < -30 mV. After pH 8, higher errors for the zeta-potential measurement were observed due to the dissolution of the IOH-NPs.

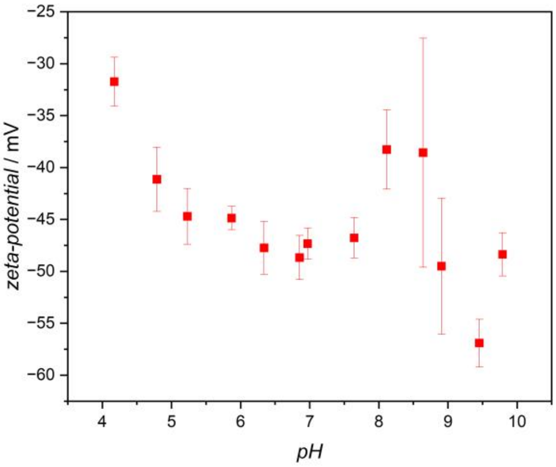

Figure 64. Zeta potential of $[GdO]^+[IR820]^-$ IOH-NPs at different pH values.

The composition of the $[GdO]^+[IR820]^-$ IOH-NPs was examined using FT-IR spectroscopy, TGA, PXRD, and EDXS. First, FT-IR spectroscopy of the IOH-NPs and the free dye (Figure 65) was conducted to examine the presence of dye in the particles. The FT-IR spectrum of the IOH-NPs exhibits the same characteristic vibrations as the free dye, confirming the presence of IR-820. FT-IR spectra show the stretching vibration $\tilde{\nu}$(O-H) = 3600-3100 cm^{-1} caused by residual water adsorbed on the NP surface. Vibrations $\tilde{\nu}$(C–H): 3000 and 2800 cm^{-1} attributed to the C_{aryl}-H and $C_{aliphatic}$-H vibrations were observed. In addition, vibrations at $\tilde{\nu}$ = 1600-1300 cm^{-1}, 1250-950 cm^{-1}, and 650 cm^{-1} can be assigned to the sulfonate moieties.

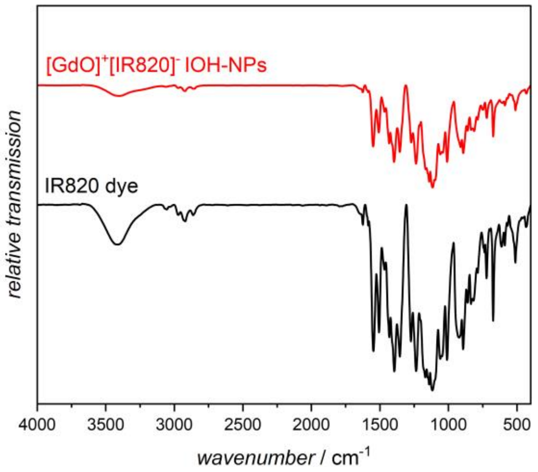

Figure 65. Determination of the composition of $[GdO]^+[IR820]^-$ IOH-NPs by FT-IR spectroscopy. FT-IR spectra of IOH-NPs (red) and IR820 dye (black).

Subsequently, TGA of the IOH-NPs (Figure 66a) was carried out to investigate the cation-to-anion ratio. First, a mass loss of 7.8 wt-% until 190°C was observed. This mass loss is attributed to residual water adsorbed on the IOH-NPs surface due to aqueous synthesis. At temperatures between 190 and 1200°C the organic compounds are converted into CO_2, H_2O, N_2, HCl and SO_2 with a total mass loss of 76.2 wt-% (corrected for the adsorbed water 82.6 wt-%). For a 1:1 cation-to-anion ratio, a mass loss of 81.9 wt-% for the organic components is expected. The mass loss measured corresponding to the organic components matches the expected mass loss. The residue, with a total weight of 16.0 wt-% was analyzed by PXRD (Figure 66b), revealing the presence of Gd_2O_3. The decomposition of the IOH-NPs can be described with the following equation:

$$2\ [GdO]^+[C_{46}H_{50}ClN_2O_6S_2]^- + 118\ O_2 \rightarrow$$

$$Gd_2O_3 + 92\ CO_2 + 49\ H_2O + 2\ N_2 + 4\ SO_2 + 2\ HCl$$

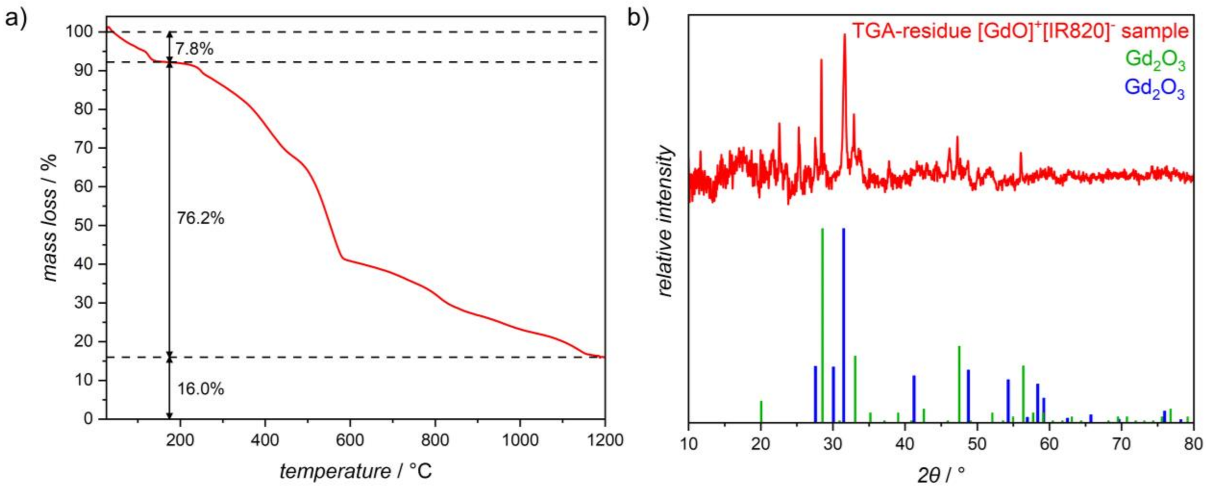

Figure 66. Determination of the composition of $[GdO]^+[IR820]^-$ IOH-NPs. **a)** TGA spectrum for the IOH-NP combustion. **b)** PXRD of the TGA residue (red) and references (blue and green).

The obtained amounts of C, H, N and S by EA of the $[GdO]^+[IR820]^-$ IOH NPs (Table 6) are corrected for the content of adsorbed water of 7.8 wt-% (corrected: C 58.8 wt-%, H 5.3 wt-%, N 1.8 wt-%, S 7.2 wt-%). The corrected values are in good agreement with the theoretically expected values C 55.3 wt-%, H 5.0 wt-%, N 2.8 wt-%, S 6.4 wt-%, which indicates a cation-to-anion ratio of 1:1.

Table 6. EA and TGA of $[GdO]^+[IR820]^-$ IOH-NPs compared to the expected calculated values.

	C [wt-%]	H [wt-%]	N [wt-%]	S [wt-%]	Mass loss [wt-%]
Measurement	54.2	5.8	1.7	6.6	84.0
Corrected (-7.8 wt-% water)	58.8	5.3	1.8	7.2	82.6
Calculated	55.3	5.0	2.8	6.4	81.9

The luminescence properties of the $[GdO]^+[IR820]^-$ IOH-NPs were examined using fluorescence spectroscopy (Figure 67). The IOH-NPs exhibit an excitation maximum at 810 nm and an emission maximum at 935 nm. The $[GdO]^+[IR820]^-$ IOH-NPs show a red-shifted emission of 111 nm compared to $[LaO]^+[ICG]^-$ IOH-NPs.

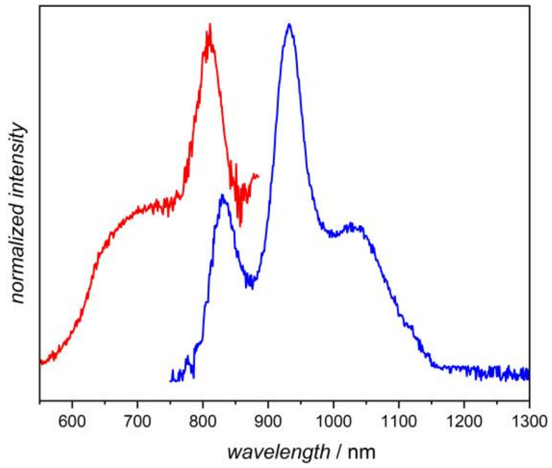

Figure 67. Fluorescence spectra recorded for $[GdO]^+[IR820]^-$ IOH-NPs. Excitation (red) and emission spectra blue collected for emission wavelength of 1100 nm and excitation wavelength of 700 nm.

9.3 Conclusion

In the current chapter, the synthesis and characterization of $[LaO]^+[ICG]^-$ and $[GdO]^+[IR820]^-$ IOH-NPs are presented using SEM, DLS, FT-IR spectroscopy, TGA, PXRD, EDXS. The ICG-based IOH-NPs showed an excitation at 773 nm and exhibited an emission maximum at 824 nm, whereas for the IR-820-based IOH-NPs an excitation maximum at 810 nm and an emission maximum at 935 nm were observed. The $[GdO]^+[IR820]^-$ IOH-NPs are novel IOH-NPs with great potential for photothermal treatment of tumors and photoacoustic imaging. In principle, both IOH-NPs should show adaptivity to light by converting NIR light into heat. The heat could be used, for instance, to trigger the reversion of a DA-adduct crosslinks within a polymer matrix, leading to locally induced degradation. Currently, a suitable polymer system is in development containing a DA adduct showing reversion at 80°C.

CHAPTER 10: PHOTOTHERMAL LASER-PRINTING OF ZINC OXIDE

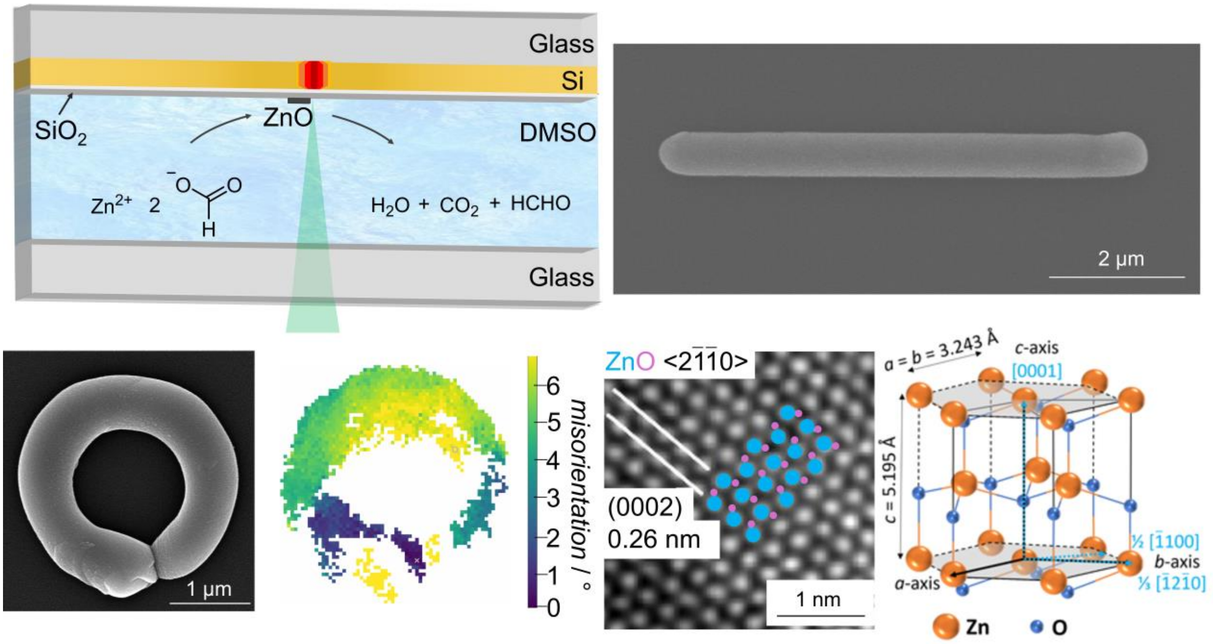

10.1 Introduction

Fabricating sub-micron metal and metal-oxide structures via laser printing is gaining attention due to the fact that these nanomaterials, for instance, have enhanced optical and electrical properties.[25,93–99] Therefore, the challenge of developing simple inks for nano-fabricating (semi-) conductive structures emerged. Generally, sub-micron laser writing can be divided into different approaches.[4] The first approach is based on multi-photon reduction of metal salts using reducing agents, which requires bulky femtosecond lasers.[25,93–99] A second strategy focuses on laser sintering of metal and metal-oxide NPs. However, most of the thermally-driven approaches lack spatial localization and still require post-processing steps. A common post-processing step involves sintering of the printed structures at elevated temperatures often above 500 °C to enable greater performance, complicating the fusing of printed inorganic materials with organic materials to fabricate heterogeneous structures. Moreover, these post-processing steps are time-consuming and energy demanding, limiting the incorporation of inorganic printing for medical and industrial applications. Inspecting the availability of inks and their compatibility, we note that there is a lack of metal and metal-oxide inks that ensure orthogonality during the printing process. A third printing approach that overcomes these limitations is photothermal laser printing, which has attracted interest.[25,90,223] Photothermally-driven reactions are applicable to a large variety of metals[86,87] and metal oxides.[25,90]

In the current chapter, the photothermal sub-micrometer laser printing of zinc oxide is introduced, a simple, clean-room free process which does not require post-processing. A detailed description of tailoring substrates to balance optical absorption and thermal transport, as well as the preparation of metal salt inks for photothermal sub-micrometer laser printing is provided. The potential of this approach is highlighted through the deposition of sub-µm ZnO wires exhibiting single-crystalline hexagonal wurtzite structure. The composition of various printed ZnO geometries was investigated in more detail using electron microscopy and diffraction methods. Furthermore, the functionalities, such as second harmonic generation (SHG) of the printed ZnO, are explored, leading to the potential for fabricating piezoelectric devices.

10.2 Substrate and Ink Design

Photothermal laser-induced printing is based on the conversion of incident light into heat to generate a steep temperature gradient, promoting chemical reactions if sufficient heat is produced. Previously, the deposition of transition metals was achieved using a 750 nm CW laser to heat printed Pt wires, which had been fabricated prior to the deposition by two-photon reduction using a femtosecond laser.[24] However, using previously printed metal structures for light-to-heat conversion limits the photothermally printed material to the predefined locations and dimensions. Thus, a substance or a substrate layer that can absorb the incident laser light is required, either by designing an ink that converts light due to the presence of a dye or by printing on absorbing layers, is required. Using a dye for the light-to-heat conversion leads to less sufficient heating compared to the precise steep temperature gradient that can be achieved by an absorbing substrate. In addition, by heating the ink instead of the substrate, less overall temperature is generated due to the long travel distance of the laser before impinging on the interface between ink and substrate. As a result, the heat is more rapidly dissipated due to the Brownian motion of the absorbing molecules or particles. Thus, an absorbing substrate to convert light into heat is prepared by sputter coating a thin metal layer on a glass coverslip. For example, a thin gold layer of close to 10 nm may be sufficient to absorb the 532 nm CW laser. However, the gold layer is electrically conductive and cannot be used for fabrication of microelectronic devices without causing short circuits. Furthermore, gold has a high thermal conductivity and, thus, the generated heat in the focal point would be rapidly dissipated, leading to disrupted printing. A material that provides low thermal conductivity – yet is still able to absorb the laser light – is silicon, which is semiconducting. Therefore, a substrate consisting of thin layers of Si/SiO_2 coated on a 22x22x0.17 mm borosilicate glass coverslip was fabricated. Si exhibits a low thermal conductivity, which helps maintain a steep temperature gradient, whereas a thin SiO_2 layer (18 nm measured by TEM) on top of the Si provides a non-electrically conductive surface to prevent short circuits.

The printing is conducted in sandwich mode, with ink placed in between a pre-cleaned glass coverslip and the substrate, enabling multi-material fabrication (Figure 68a). The light passes through the ink and is focused on the substrate surface, where the amorphous silicon film (265 nm measured by TEM) acts as an absorber, generating sufficient heat to promote decomposition of the metal precursor. The geometry of the structures can be tailored by moving the substrate relative to the incident light in *x* and *y*, leading to the fabrication of ZnO wires and circles exhibiting line widths of approximately 0.5 µm (Figure 68b). Moreover, photothermal laser-induced printing of ZnO is also carried out using a commercially available Si wafer as substrate to minimize the preparation time of the substrate. However, under similar conditions no ZnO formation was observed likely due to reduced absorption and improved thermal conductivity in a 3D space provided by the crystalline Si wafer. Thus, insufficient heat was generated and the activation energy for the chemical reaction to occur could not be overcome.

To date, ink formulations for photothermal laser-induced printing of metal oxides have consisted of metal precursors (i.e., metal salts and complexes) dissolved in water, with the addition of reducing/oxidation agents, as well as the addition of acids or bases, (e.g., ammonia).[25] However, this created incompatibility between individual inks, limiting ink orthogonality, and thus device fabrication. In addition, water has a reduced boiling point compared to some organic solvents, leading to bubble formation when exposed to a steep temperature gradient, disrupting the printing process or leading to microbubble-assisted printing. When targeting thermally-driven reactions, the metal salts or complexes used need to be thermally instable at elevated temperatures and soluble in solvents displaying high boiling points. Therefore, a simple ink concept for printing single-crystalline ZnO is introduced based on a saturated solution of zinc formate in DMSO. In the literature, zinc formate is used as a component to prepare semiconducting films.[238] Moreover, DMSO exhibits a high boiling point of 189 °C and a refractive index matching the objective lens, which widens the window before bubble formation occurs and supports focusing the CW laser. In the literature, the thermal decomposition of zinc formate ZnO, CO_x,[239] H_2O, and HCO_2CH_3[240,241] via the Tishchenko reaction of HCHO is reported to occur under ambient and anoxic conditions.[242] Typically, anhydrous $Zn(HCO_2)_2$ decomposes at temperatures of approximately 270 °C, involving two steps.[234,235] Initially, the anion decomposes into an intermediate hydride anion and carbon dioxide, which is followed by the combination of the hydride anion with the formate anion, leading to $H_2CO_2^{2-}$,[240,241] subsequently decomposing to O^{2-} and HCHO, yielding ZnO. Subsequently, different thicknesses of the prepared Si/SiO_2 substrates and the efficiency of the synthesized zinc formate ink were examined in photothermal laser printing.

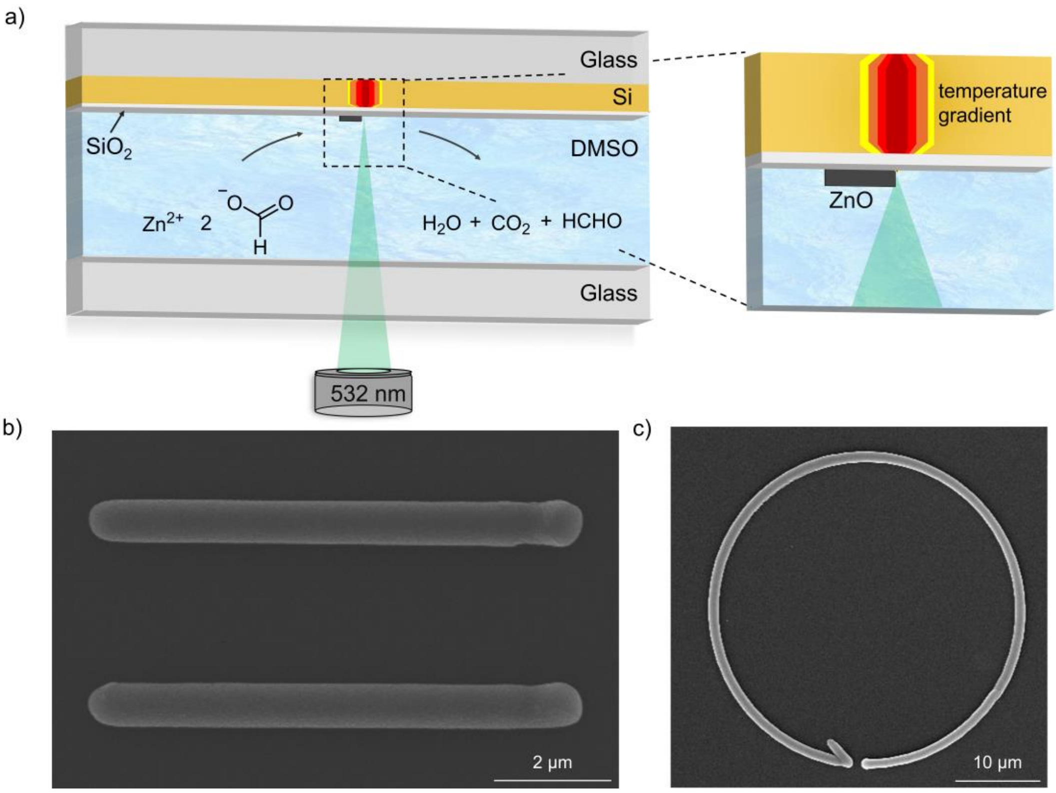

Figure 68. a) Scheme of photothermally laser printing of ZnO using a saturated zinc formate in DMSO solution as precursor. The incident light of a 532 nm CW laser is converted by the Si/SiO_2 into heat, causing thermal decomposition of zinc formate**. b)** SEM image of two sub-µm thick ZnO wires. **c)** SEM image of a ZnO circle. Both structures are fabricated using a laser power of 0.85 mW and a laser-writing speed of 1 µm s^{-1}.

10.3 Photothermal Laser-induced Printing

When comparing the printing on a 50 nm Si coated glass coverslip with printing on a 265 nm coated Si glass coverslip, one key difference was observed. For the ZnO wire printed on the 50 nm Si substrate, a phenomenon referred to as “thermocycling” occurred (Figure 69a), which is not observed for the 265 nm Si substrate (Figure 69b). Thermocycling takes place in cases of insufficient heat conversion. During printing of metals and metal oxides, often inorganic materials with a higher thermal conductivity compared to the SiO_2 layer are deposited. Subsequently, the heat transfer away from the printed seed is enhanced, causing a wire to appear bean-shaped instead of a uniform line. Using a 265 nm Si layer, sufficient heat is generated to compensate for this phenomenon; due to absorbing the laser light slightly in the volume, a heat sink is generated. However, this phenomenon needs to be considered when printing structures close to one another (e.g., solid fields as electrodes). Furthermore, by increasing the thickness of the laser absorbing Si layer, the laser power at 100 % can be reduced from 34 mW using 50 nm Si to 3 mW using 265 nm Si.

Moving forward using these results, Si/SiO_2 substrates of 265 nm Si and 18 nm SiO_2, as measured by TEM, are utilized to further explore the potential of photothermal laser printing.

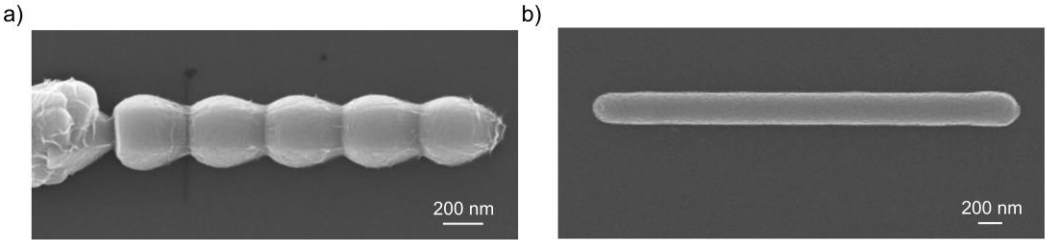

Figure 69. Photothermal laser-induced printed ZnO wires on Si/SiO_2 coated glass coverslips with different Si thickness. **a)** ZnO wires printed at a laser power of 11 mW and laser scanning speed of 1 µm s^{-1} on a 50 nm silicon, 5 nm SiO_2 coated substrate showing thermocycling caused by the different thermal conductivities of SiO_2 and ZnO and a low temperature gradient. **b)** 500 nm wide ZnO line printed at laser power of 0.85 mW and laser-writing speed of 1 µm s^{-1} on 350 nm thick Si, 5 nm SiO_2 coated substrate.

Subsequently, the performance of the zinc formate ink was investigated. Generally, the quality of an ink for printing inorganic materials can be described by three parameters that are strongly correlated. The first parameter that needs to be explored is sensitivity, which defines the laser powers at which precise metal or metal-oxide structures begin to form. In addition, sensitivity also includes addressing the stability of the ink and its storage. The second aspect is the formation rate, which describes the writing speed used to print the desired structure. The last parameter is the crystallization that describes the nature of the fabricated structures, for instance, sintered NPs films, polycrystalline, or single-crystalline structures. Together, these parameters define the optimal printing window at which the ink should be used.

The performance of the zinc formate ink was investigated by conducting dose tests. In a dose test (Figure 70a), the laser scanning speed is kept constant while varying the laser power and the substrate position relative to *z* (corresponding to the direction of the incident light). This allows identification of the best printing parameters to fabricate thin wires (here: laser-writing speed of 1 µm s^{-1} and laser power of 0.85 mW), which are highly desirable for preparation of microelectronic devices. The results (Figure 70b) reveal that on thick Si/SiO_2 layers (265 nm) 500 nm thin uniform ZnO wires can be printed at low laser powers of 0.85-0.9 mW and a laser scanning speed of 1 µm s^{-1}. The low laser powers are attributed to a high sensitivity of the ink and an excellent tailored substrate. In contrast, the fabrication rate of ZnO wires is rather slow compared to conventional polymer printing. During the fabrication of sub-µm single-crystalline ZnO, no bubble formation was observed, indicating that ZnO decomposition is enhanced in DMSO. Furthermore, an increase in the laser power resulted in the printing of several µm thicker ZnO structures due to higher heat generated upon light-to-heat conversion. Based on this finding the structure dimensions can be adjusted by varying the laser power. Higher laser scanning speeds than 1 µm s^{-1} lead to disrupted printing.

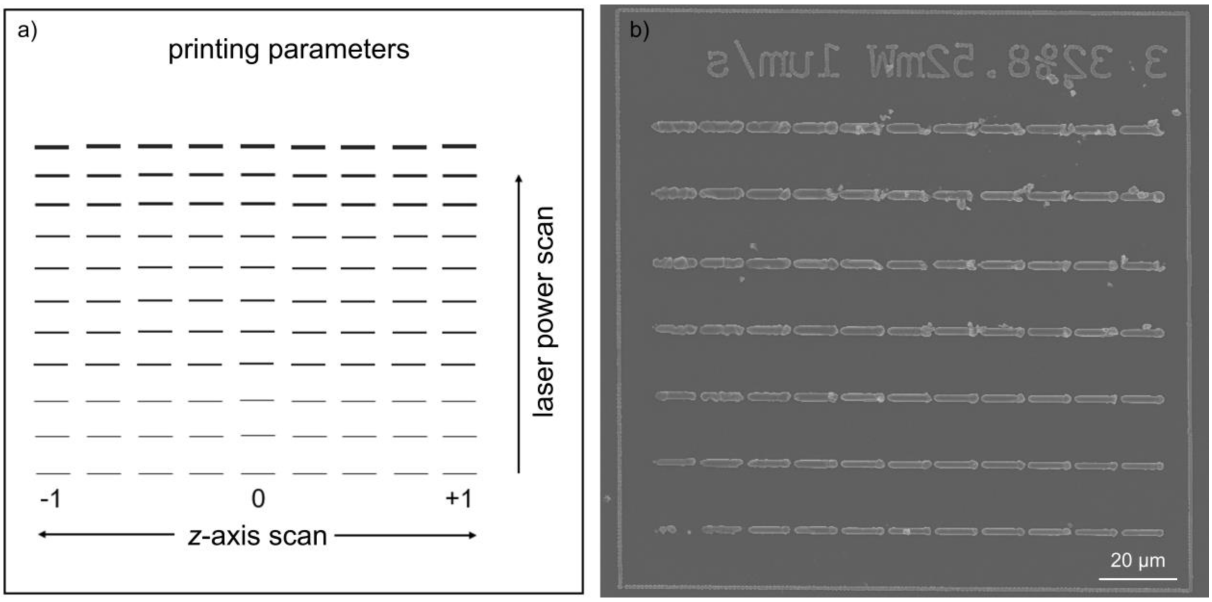

Figure 70. Dose test for photothermal laser printing ZnO: **a)** Schematic representation of a printed dose test. In *x*-direction a scan of the *z*-axis was performed, which changes the laser focus within a row. In *y*-direction the laser power is increased from bottom to top within a column. **b)** Photothermally printed ZnO dose tests from laser powers of 0.85-8.52 mW and a laser scanning speed of 1 µm s^{-1} on a 265 nm Si/SiO_2 coated glass coverslip.

Subsequently, the printing of ZnO pads (Figure 71) was investigated by spacing individual wires closer together. Initially, the individual wires do not influence each other. However, by narrowing the distance between the wires, they begin to fuse together. Finally, by forcing the wires to overlap, a solid ZnO pad is formed, which is attractive for fabrication of electronic devices.

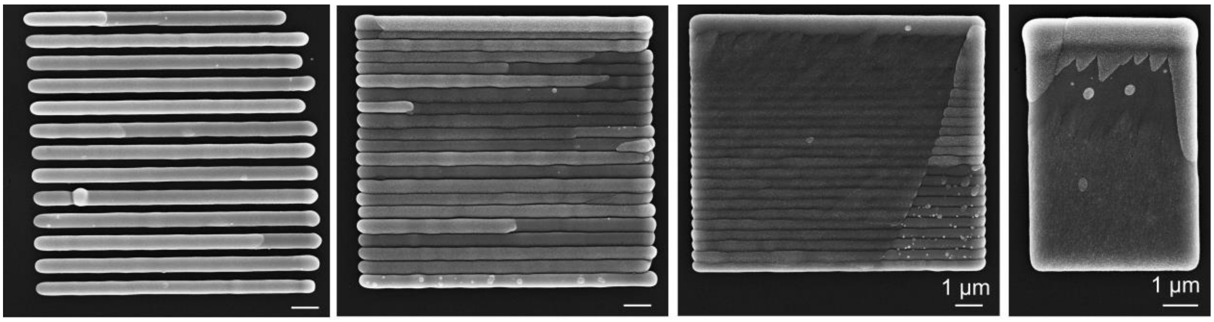

Figure 71. Evolution of narrowing the distance between individual ZnO wires until they overlap to form a pad. The wire spacing is reduced from 0.6 mm left to 0.2 mm right.

Furthermore, the characterization of printed ZnO at higher laser powers by SEM analysis shows that the printed ZnO exhibits crystal facets at elevated laser powers (Figure 72a). In fact, ZnO can crystallize in the wurtzite-type ($P6_3mc$, hexagonal), which has no inversion symmetry and therefore shows SHG, making it suitable for fabricating optoelectronic devices. Point exposure experiments are conducted at an exposure time of 1000 ms. SEM analysis of the point exposure experiments (Figure 72b) exhibits crystals with random orientation. This indicates that the amorphous substrate cannot induce a preferred direction of the crystal growth.

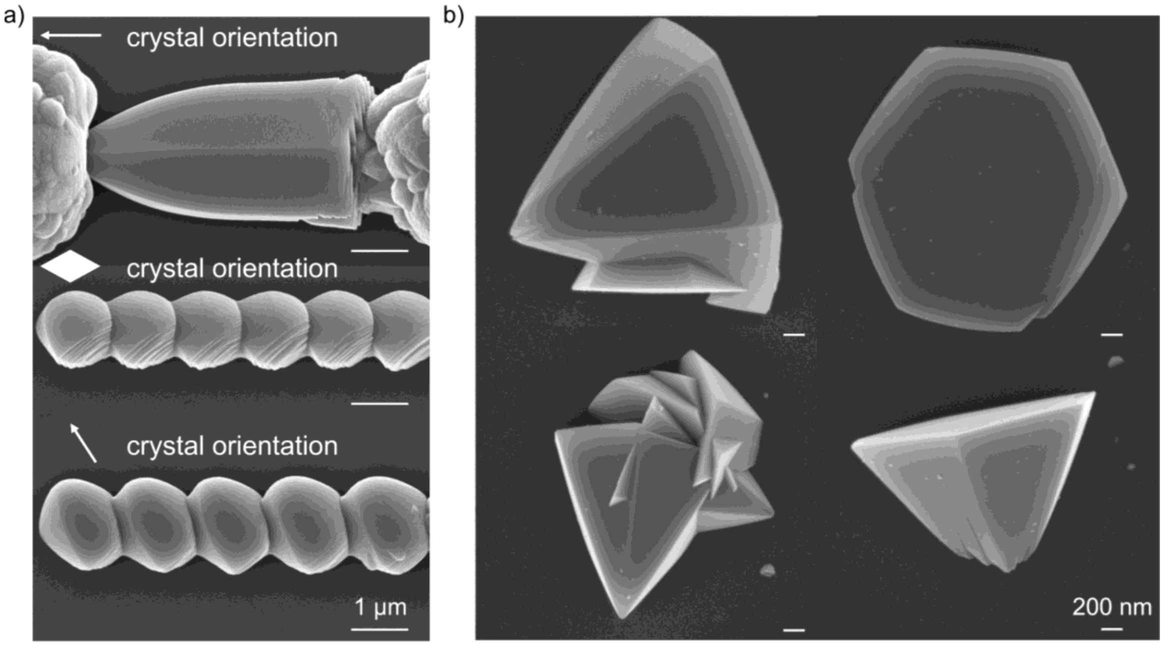

Figure 72. SEM images of potential crystalline ZnO: **a)** Photothermal laser printing at high laser powers (2-5 mW) and fixed laser scanning speed of 1 µm s^{-1} resulting in ZnO lines with a crystalline appearance and different crystal orientations indicated by the white arrows and planes. **b)** SEM images of point exposure at 1000 ms, indicating that initial crystal orientation is random.

The next section focuses on the solid structure of the printed ZnO, the last parameter to describe the quality of the zinc formate ink.

10.4 Solid Structure Studies

The crystallinity of the as-prepared ZnO structures was analyzed in cooperation with the working group of Yolita Eggeler (LEM, KIT). Initially, FIB cutting was performed to polish ZnO structures of various geometries for further surface-sensitive investigations using EBSD to study the crystallinity and crystal orientation. EBSD analysis of a 10 µm long ZnO wire (Figure 73a-c) confirmed that the material is composed of the hexagonal ZnO wurtzite structure ($P6_3mc$, space group 186). For evaluation of the crystallographic orientation, an external coordinate system was selected, with *x* and *y* being in the surface plane and *z* as the surface normal. The inverse pole figures (IPF, Figure 73b) show the formation of a large single ZnO grain, revealing single crystallinity. However, a color change in the IPF maps was observed, which is caused by a steadily increasing lattice rotation along the wire. Quantitative evaluation shows a total misorientation of 16° for the 10 µm long wire, corresponding to an average rotation rate of approximately 1.6° µm^{-1} (Figure 73c). In the literature, lattice rotations were observed, for instance, in laser-heated glasses and spherulitic crystals.

Next, the crystallinity of ZnO circles was investigated using EBSD measurements (Figure 73). The observations indicate that a crystal seed with a random orientation is formed at the beginning of the printing. Subsequently, the crystal growth of the hexagonal ZnO occurs by rotating in the plane (*xy*-plane; $\bar{1}100$). Typically, the ZnO wurtzite structure grows fastest in the [0001] direction, which does not consistently align with the wires. This indicates that the initial crystal seed is formed randomly and dictates the crystal growth. The EBSD analysis of different circles also confirms the single crystallinity of the printed ZnO, as well as continuous lattice rotation with varying rotation rates.

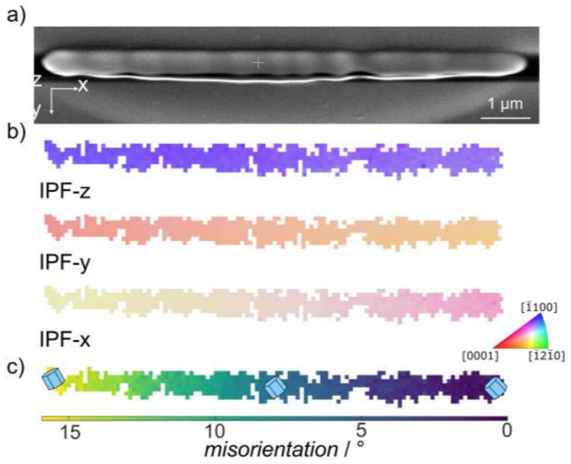

Figure 73. EBSD analysis of a 10 µm long ZnO wire. **a)** SEM image of fabricated ZnO circle **b)** Color-coded IPF-maps for the ZnO wire. Inset shows the stereographic triangle with color legend corresponding to the IPF-maps. **c)** Misorientation maps for the crystal rotation within the ZnO wire.

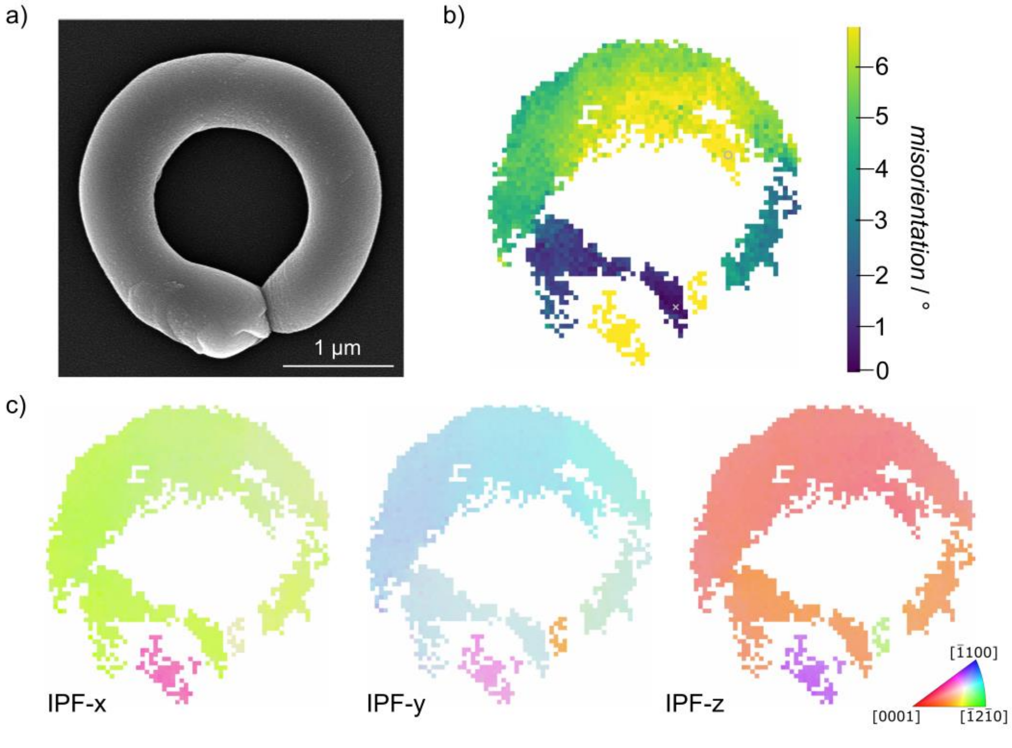

Figure 74. EBSD analysis of a ZnO circle with a 1 µm radius. **a)** SEM image of fabricated ZnO circle **b)** Misorientation maps for the crystal rotation within the ZnO circle. **c)** Color-coded IPF-maps for the ZnO circle. Inset shows the stereographic triangle with color legend corresponding to the IPF-maps.

The solid structure depends on the laser-writing speed and the printing power. To investigate the dependency of the solid-structure formation on the printing parameters, two ZnO wires were polished by FIB, and EBSD analysis was conducted. Initially, EBSD measurements (Figure 73a) on a wire printed at a laser-writing speed of 1 μm s^{-1} and a laser power of 2.98 mW were studied, showing larger grains with different crystal orientations. In addition, similar EBSD analysis (Figure 73b) of a ZnO wire fabricated at a laser-writing speed of 20 μm s^{-1} and a laser power of 2.98 mW exhibits various small grains. By increasing the printing speed and at constant laser power, the solid structure of ZnO changes from single-crystalline to polycrystalline. EBSD analysis for laser-writing speeds higher than 20 μm s^{-1} is complicated due to a large number of pores observed within the structure.

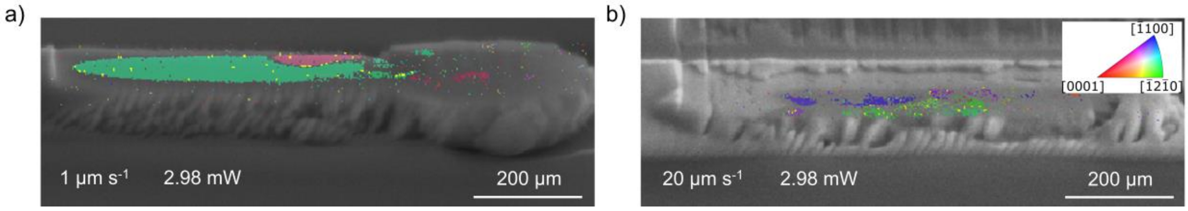

Figure 75. EBSD analysis of ZnO wires fabricated under different printing parameters. **a)** Printed ZnO wire at a laser-writing speed of 1 μm s^{-1} and a laser power of 2.98 mW. EBSD results indicate that the ZnO wire is comprised of different grains. **b)** ZnO wire fabricated at a laser-writing speed of 20 μm s^{-1} and a laser power of 2.98 mW. EBSD analysis exhibits small grains.

As the orientation of the initial seed is random and due to the interaction between the surrounding ink and substrate, no consistent alignment with the [0001] axis was observed for the circles and angles. In summary, these results show that photothermal laser-printing can be used to achieve high functionality regardless of the printed geometry, which is attractive for device fabrication.

Subsequently, STEM and HRTEM analysis (Figure 73) of cross-sections of ZnO wires was performed, which validates the formation of single-crystalline ZnO with $\langle 2\bar{1}\bar{1}0\rangle$ zone-axis orientation, showing a lattice rotation. A thickness of approximately 180 nm is found for the ZnO wires, and nano-sized pores within the ZnO crystal were observed. Their origin is likely due to the rapid cooling induced by moving the laser focal spot and the steep temperature gradient.

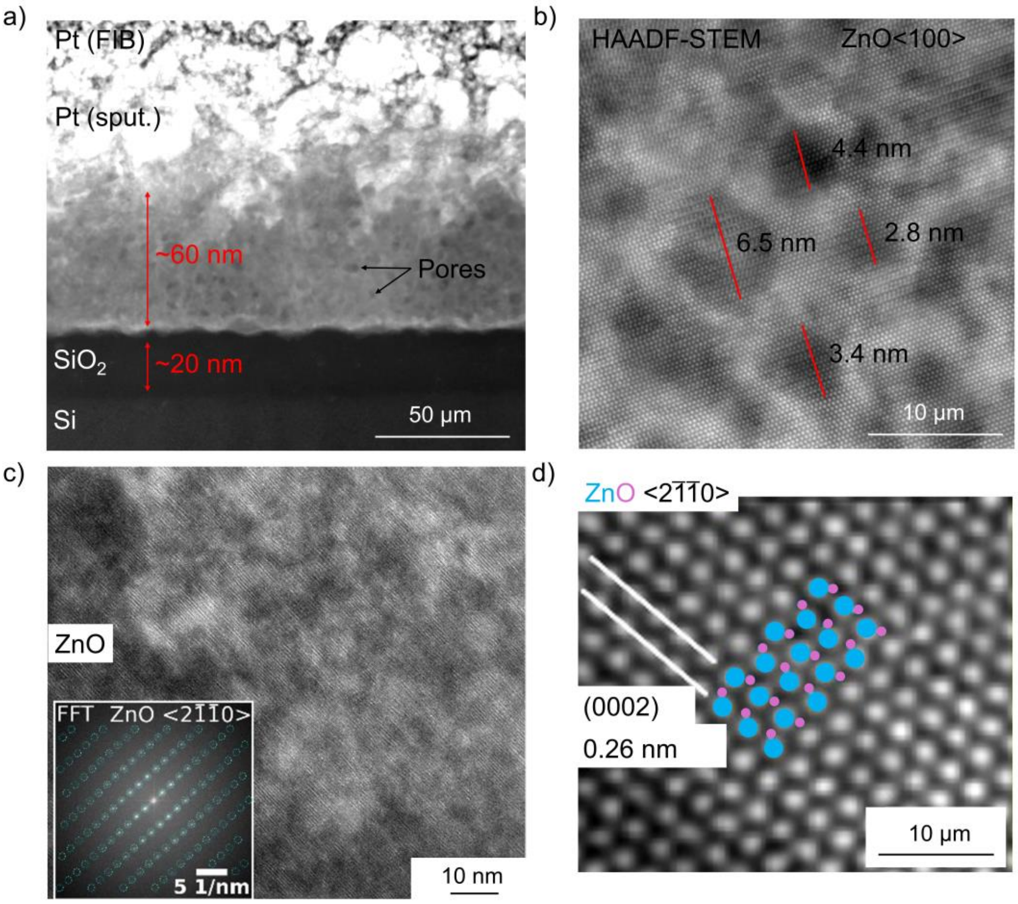

Figure 76. TEM analysis of a ZnO wire cross-section prepared by FIB. **a)** HAADF STEM image providing an overview of the ZnO wire and substrate. The platinum is used for FIB processing. **b)** Close-up HAADF STEM image showing nm-sized pores within the structure. **c)** HRTEM image and FFT pattern of HRTEM image exhibiting lattice periodicities for the ZnO structure. **d)** Magnified region of the HAADF-STEM image, indicating ZnO $(2\ \overline{1}\ \overline{1}\ 0)$ zone-axis orientation.

EDXS measurements were performed to confirm the chemical composition. The evaluation of the EDXS maps (Figure 73) led to a total amount of 53.9:46.1 at-% Zn:O and for the silica layer to 36.1:63.9 at-% Si:O. Both results are in good agreement with the estimated ratios of 50:50 for ZnO and 33:66 for SiO_2. The slightly reduced O_2

concentration can be explained by X-ray self-absorption of the low energy K_α X-rays in the sample. Furthermore, trace amounts of S and C contamination were observed within the ZnO, which may be caused by the decomposition DMSO during printing.

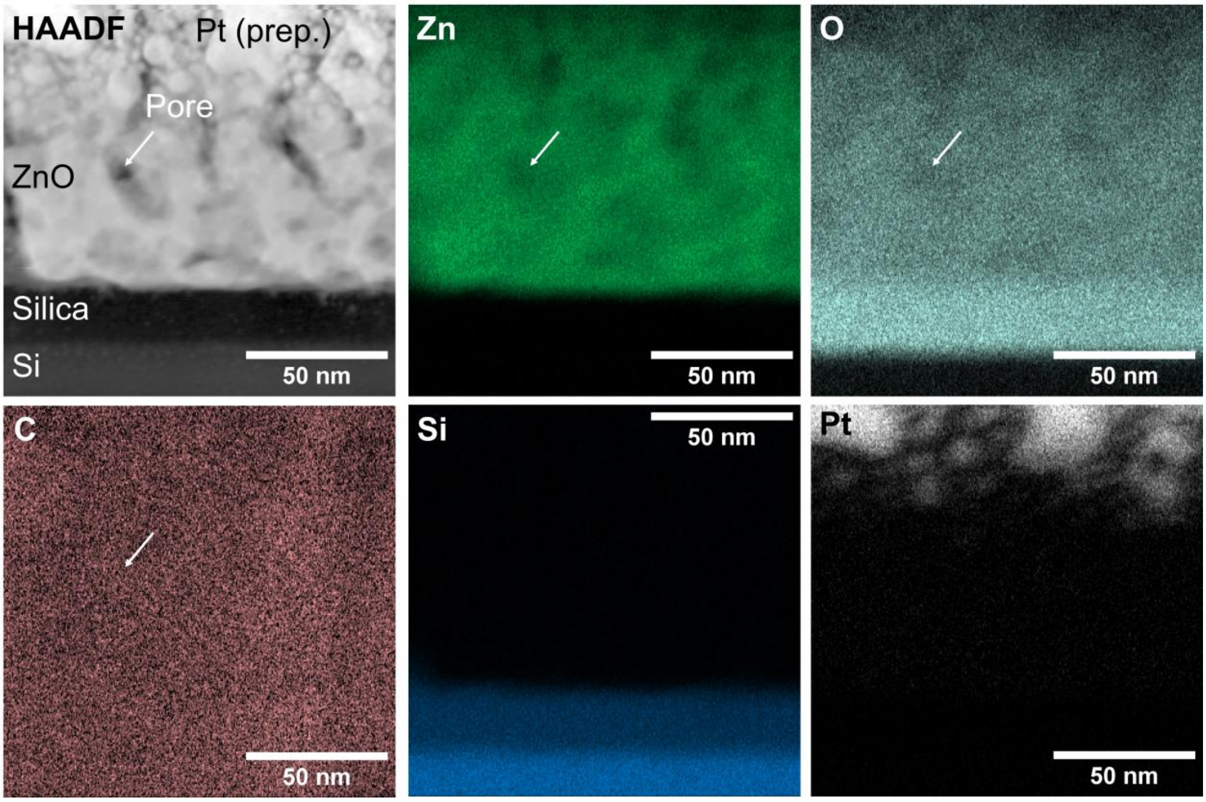

Figure 77. Elemental distribution maps determined by EDXS. The evaluation of the data is in perfect agreement with a 50:50 ratio for Zn:O. Furthermore, the substrate coating fits with the estimations, as well. The first substrate layer consists only of Si and the top layer is composed of around 33 at-% silicon and 66 at-% O_2, which corresponds with SiO_2.

Overall, both TEM and EBSD results show the formation of single-crystalline ZnO containing traces of impurities and exhibiting a random crystal orientation undergoing lattice rotation. After the high structural quality of the printed ZnO was revealed by EBSD, EDXS, and TEM analysis, the next step was to study the optical response of the single-crystalline semiconductor.

10.5 Second Harmonic Generation

SHG was observed in ZnO because the wurtzite structure is non-centrosymmetric and therefore lacks a center of inversion symmetry. The SHG effect was studied by scanning a 780 nm emitting femtosecond-pulsed laser over ZnO wires using a microscope objective and recording the reflected light. The SHG spectrum (Figure 78a) shows a clear frequency-doubled peak at 390 nm and a weak emission at 377 nm, possibly caused by band-edge luminescence. Furthermore, polarization-dependent SHG mapping was performed by rotating the incident laser polarization by 90°, revealing spatial variations in intensity along the wire,[23] which correlate with lattice rotation observed by EBSD and TEM analysis. These observations demonstrate that photothermally laser-printed ZnO exhibits a non-linear optical response corresponding to the crystallographic formation and is attractive for the fabrication of piezoelectric devices.

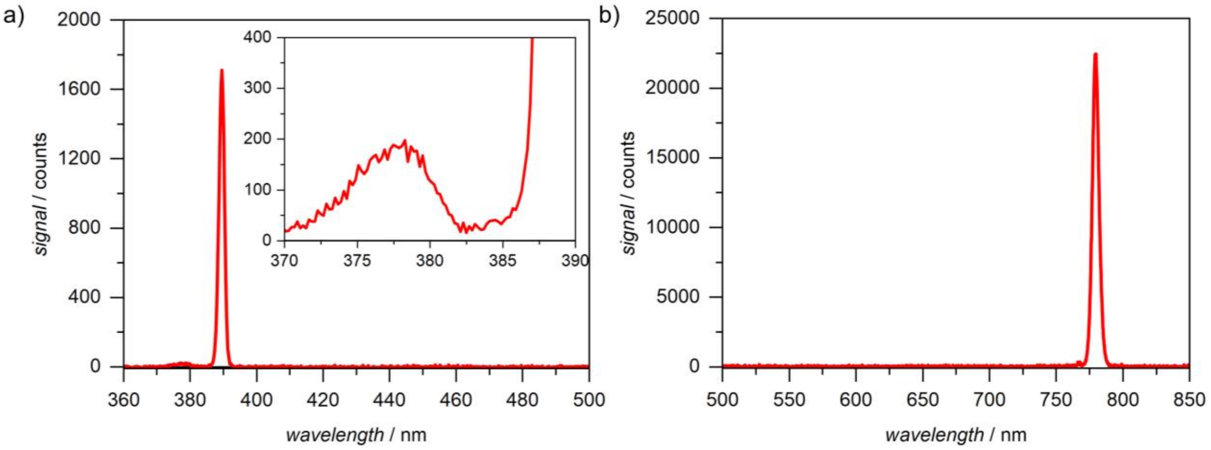

Figure 78. Determination of the SHG effect of ZnO assessed using a femtosecond laser. **a)** SHG spectra recorded for a ZnO wire using a 780 nm fs laser 4.6 mW (0.196 TW cm^{-2}) for exposure with a 500 ms exposure time of the spectrometer CCD. Inset shows a zoomed-in view of the emission peak at 377.4 nm using a 5 s exposure time of the spectrometer CCD camera (5 s). **b)** Recorded spectra of the 780 nm fs laser source used to investigate the SHG effect in the ZnO.

10.6 Conclusion

In the current chapter, the photothermal laser-printing of single-crystalline sub-µm ZnO without the need for post-processing or femtosecond pulsed laser irradiation is introduced. Initially, a brief description of the substrate fabrication and key aspects for designing a metal salt containing ink employed in photothermal laser-printing is provided. The fabrication of various 2D microstructures with complex geometries such as wires and circles is shown. EBSD and TEM analysis reveal that the printed ZnO consists of a single wurtzite-type crystal, which shows lattice rotation along the printed structure. Moreover, the crystal orientation is random and does not follow any pattern. Small traces of S and C impurities were observed within the ZnO single-crystals using EDXS analysis. Finally, a non-linear optical response is found for the ZnO, exhibiting polarization dependence. In summary, these findings show that the photothermal laser printing can be employed to fabricate single-crystalline sub-µm structures relevant for preparation of electronic and piezo electric devices.

CHAPTER 11: PHOTOTHERMAL LASER PRINTING OF METALS AND METAL OXIDES

Electronic and piezoelectric devices can be fabricated in a step-by-step fashion, (e.g., metal – metal oxide – metal). The key is to use orthogonal inks that ensure high material compatibility without disrupting the printing process or dissolving the previously printed patterns. For instance, diodes and memristors have been fabricated by multi-photon printing of platinum and silver with a ZnO coating on top of the platinum wires formed by thermally-driven reaction.[25] New metal inks need to be designed to fabricate electronic devices such as diodes using photothermal laser printing. For the fabrication of a diode using ZnO as the semiconductor, two metals are required that exhibit asymmetry in their electrical contacts — for instance, a high-work-function metal like platinum and a low-work-function metal such as silver. Platinum provides a strong Schottky barrier and silver forms an Ohmic contact due to a similar work-function compared to the electron affinity of ZnO.[244,245] Thus, the photothermal laser printing of platinum is explored in the next section.

11.1 Photothermal Laser-induced Printing of Platinum and Gold

The first task is to identify metal complexes that can be readily decomposed and release Pt^{2+} ions. Subsequently, the cation is reduced with a thermal reducing agent (e.g., sodium citrate or hydroquinone) to form metallic platinum. Thus, initial metal printing tests were carried out with dichloro(1,5-cyclooctadiene)platinum(II) and a reducing agent in dimethyl sulfoxide. The metal cyclooctadiene complex is commercially available and can readily be decomposed into smaller organic compounds by releasing platinum(II), which is reduced by either hydroquinone or sodium citrate to platinum(0). Using this ink formulation precise photothermal laser printing at a laser power of 12.8 mW and a laser scanning speed of 2 μm s^{-1} of platinum on a 125 nm Si, 5 nm SiO_2 coated substrate is enabled (Figure 79a). However, the printed platinum consists of small NPs sintered together in thin film rather than a solid wire. Such a thin film can be easily disrupted, breaking the contact between the NPs, thus, solid wires are preferable. The results led to the discontinuation of the photothermal laser printing of platinum. Photothermal laser printing of silver is not carried out since silver(I) salts are reduced by light to metallic silver. Thus, silver laser writing always shows intrinsic photochemical activity, complicating photothermal laser-induced printing. Moreover, the decomposition of three different gold(I) complexes is explored. These complexes are selected because in theory the Au^{+} cation should not be stable and is expected to disproportionate into Au^{3+} and metallic Au. The results for thermal decomposition upon heating show that chloro(triphenylphosphine)gold(I) decomposes the slowest. In the second place is chloro(tetrahydrothiophene)gold(I), which is used as starting material for the gold phosphate complex and chloro(dimethyl sulfide)gold(I) decomposes the fastest. Based on these results, it is evident that the gold tetrahydrothiophene complex is more suitable for photothermal laser-induced printing than the others. The first gold complex took too long to decompose, requiring lower laser scanning speeds, leading to a low quality of the printed wires. The dimethyl sulfide gold complex decomposes too rapidly, which generates NPs everywhere on the substrate surface and can result in short circuits. Using chloro(tetrahydrothiophene)gold(I) dissolved in N-methyl-2-pyrrolidone, which can act as solvent and reducing agent, gold wires are printed at a laser power of 0.26 mW and a laser scanning speed of 1 µm s^{-1} on a 250 nm Si, 5 nm SiO_2 substrate (Figure 79b). However, the formation of NPs next to the wires was observed during photothermal laser printing of gold by SEM analysis. EDXS analysis (Figure 79c) was carried out to investigate the composition of the gold wires. The presence of gold within the wires is validated, but sulfur contamination is detected, which can lower the electrical conductivity.

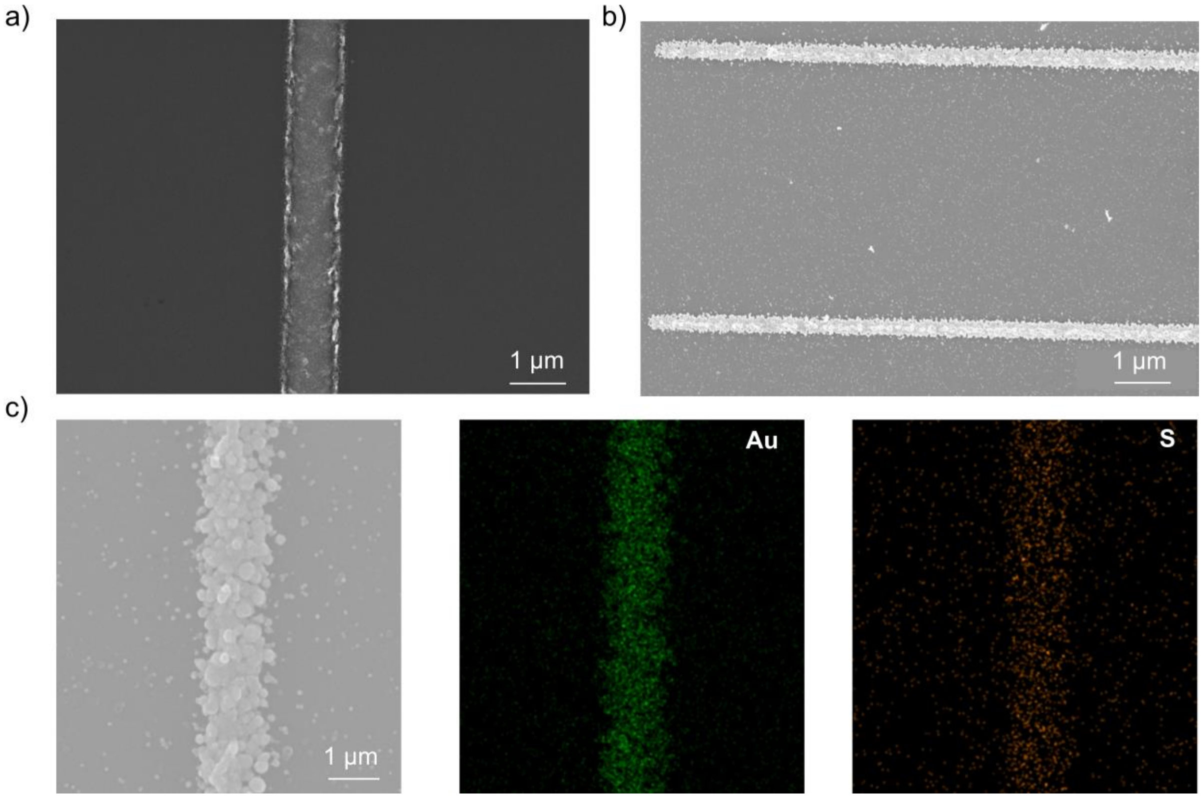

Figure 79. Photothermal laser printing of two different metals: **a)** Photothermally laser printed platinum on a 125 nm Si, 5 nm SiO_2 coated glass coverslip by using a dichloro(1,5-cyclooctadiene)platinum(**II**) ink: 0.11 mol L^{-1} in dimethyl sulfoxide, power: 12.8 mW, speed: 2 µm s^{-1}**b)** Photothermally laser printed gold on a 250 nm Si, 5 nm SiO_2 coated glass coverslip by using a chloro(tetrahydrothiophene)gold(**I**) ink: 0.19 mol L^{-1} in N-Methyl-2-pyrrolidone, power: 0.26 mW, speed: 1 µm s^{-1}. **c)** SEM image and EDXS maps for the photothermally laser printed gold wire.

11.2 Conclusion

In summary, the photothermal laser printing of metallic platinum and gold has been investigated. Using dichloro(1,5-cyclooctadiene)platinum(II), thin films of sintered NPs were printed. However, thin films are less desirable for the fabrication of electronic devices due to reduced performance compared to solid wires. Subsequently, different gold(I) complexes were explored as an alternative. Based on the metal complex, varying sensitivities for the thermal decomposition were observed. During photothermal printing the formation of NPs next to the printed Au wires was observed. Furthermore, EDXS analysis confirmed the presence of sulfur contamination in the wires. Ultimately, further metal salts and metal complexes need to be identified and explored using photothermal laser printing.

CHAPTER 12: CONCLUSION

The present work demonstrates the use of photo-induced printing techniques for the fabrication of responsive, adaptive composite materials and sub-μm metals and metal oxides. These printing techniques include DLP, SLA and photothermal laser printing to prepare a variety of different materials with complex geometries and sizes, due to their excellent spatiotemporal resolution.

To date, the application of IOH-NPs has been restricted to drug delivery and bioimaging. For the first time, responsive IOH-NPs were incorporated into polymer matrices, and their potential for the fabrication of externally stimuli-responsive materials was demonstrated. Initially, various saline IOH-NPs, composed of inorganic cations and functional dye anions, were synthesized and characterized in-depth. This work shows that the unique composition of the IOH-NPs can be exploited to introduce and to adjust their responsiveness to external stimuli, such as pH, O_2 and light, by careful selection of the inorganic cations and dye anions.

ARS, a pH-indicator, was used to prepare pH-sensitive $[La(OH)]^+[ARS]^-$ IOH-NPs with a size of 42±7 nm, exhibiting a visual colorimetric change from yellow to violet and a luminescence shift from green to red emission. Subsequently, a robust composite-material ink was carefully designed and optimized, composed of high IOH-NP loadings of up to $3.7\ g\ L^{-1}$, PEGDA700, and DEABP, while taking autofluorescence, light scattering, and IOH-NP aggregation into account. By employing DLP and SLA, various 2D and 3D pH-sensitive composite-material structures, as well as multi-materials, were fabricated to monitor and control pH changes. The presence of the IOH-NPs within the polymer matrix was confirmed using SEM, EDXS, XPS, and ToF-SIMS. Moreover, the pH responsiveness of the composite materials was studied in detail, and the results were compared to the IOH-NP suspension and the free ARS dye. An IOH-NP concentration-dependent pH sensitivity was observed for the composite materials, which otherwise exhibited similar pH-dependent optical properties to those determined for the IOH-NP suspension. The main difference between the IOH-NP suspension and the composite materials was that the latter exhibit hyperchromic luminescence intensities due to the surrounding polymer matrix, which mitigates ACQ. In addition, high photostability of the composite material upon irradiation with UV light was observed. These findings confirm the successful incorporation of the IOH-NPs into the polymer matrix, which enhances their optical properties. The demonstrated fabrication of the multi-materials highlights the potential basis for the incorporation of additional functionalities.

Based on FMN, O_2-responsive $[ZrO]^{2+}[FMN]^{2-}$ IOH-NPs with a size of 41±10 nm were prepared, and their optical properties, depending on the redox state of FMN, were fully evaluated. The luminescence of the reduced form of FMN is quenched and exhibits a transparent color, whereas the oxidized form exhibits intense luminescence combined with a yellow color. Subsequently, the IOH-NPs were employed for the fabrication of various O_2-responsive composite materials using DLP. The O_2 responsiveness and sensitivity could be adjusted by varying the IOH-NP concentration and material thickness. The optical properties and durability of the O_2-responsive composite material were tailored to monitor O_2 levels for a wide range of applications, for instance, packaging, battery assembly, and pharmaceutical production. A simple read-out of the O_2 level in the corresponding environments was performed by using a UV- or blue-light-emitting flashlight to determine the luminescence turn-on.

Perylene dyes exhibit π-stacking and ACQ, leading to complete luminescence quenching. This behavior was exploited to prepare multi-responsive composite materials, enabling sensing based on luminescence turn-on behavior. Initially, PTCDA was used for preparation of $[Ag]_4^+[PTC]^{4-}$ IOH-NPs with a size of 122±22 nm, which are multi-responsive to external stimuli, such as light and small molecules. The adaptivity of these IOH-NPs originates from the silver cation, which can be readily reduced to metallic silver, undergo complexation, and form more stable salts, such as silver chloride. Various complex composite-material structures, such as 2D koalas and porous cubes, were fabricated by DLP. Next, the utilization of the composite material for histamine sensing in blood serum, crucial for the determination of an anaphylactic shock, was explored. However, blood serum contains chloride and cysteine, both of which resulted in intense luminescence of the composite-material in the absence of histamine. Attempts to remove chloride and cysteine from the blood serum were unsuccessful. Consequently, the focus of the sensing application was redirected. A promising sensing application for the composite material is the detection of UV light, which is based on the reduction of Ag^+ to Ag^0 upon light radiation. A proof-of-concept for the monitoring of UV radiation is provided and demonstrates that only upon UV radiation, the reduction of Ag^+ to Ag^0 occurs, which leads to the release of fluorescent $[PTC]^{4-}$ and a color change of the composite material.

Apart from composite materials for luminescence-based sensing applications, IOH-NPs based on ICG and its derivative IR-820 were prepared to convert light into heat, with sizes of 46±9 and 98±28 nm, respectively. The synthesized $[LaO]^+[ICG]^-$ and $[GdO]^+[IR820]^-$ IOH-NPs exhibit great potential for photothermal treatment of tumors and photoacoustic imaging.

The conversion of light into heat was also exploited in photothermal laser printing of sub-µm metal and metal-oxide structures. A substrate consisting of silicon and silica was prepared to absorb the laser light of a 532 nm emitting CW laser and convert the light into a steep temperature gradient, allowing fabrication of metals and metal oxides directly from solution. The simple ink concept consists of metal salts or metal complexes that are thermally unstable at temperatures exceeding 100 °C, and dimethyl sulfoxide as a high boiling solvent to prevent microbubble formation. Photothermal laser printing conducted using this substrate and an ink containing zinc formate led to the formation of sub-µm single-crystalline zinc oxide wires and circles. The single-crystalline zinc oxide exhibits a wurtzite-type structure, which shows SHG. This work provides the basis to fabricate metals and further initial experiments to print platinum and gold wires are described.

The present thesis introduces a versatile platform to adjust commonly used photoresins, typically leading to the formation of static structures with limited property profiles, towards dynamic composite structures and inorganic materials with improved and adaptable chemical, physical and mechanical properties. This opens new avenues to employ photo-induced printing for emerging applications, for instance in smart sensors and optoelectronic components.

CHAPTER 13: OUTLOOK

The current thesis lays the foundation for future developments in the fabrication of responsive composite materials and microelectronic devices using diverse photo-induced printing techniques.

The presented work establishes a way to integrate functional IOH-NPs into a polymer matrix to introduce responsiveness and adaptivity. Promising next steps include the integration of different functional IOH-NPs into polymer networks to gain access to new applications. Achieving responsiveness and adaptivity to a diversity of external stimuli, such as temperature or moisture, represent exciting avenues for future innovations. Looking forward, the fabrication of multi-responsive composite materials remains an important task. This includes expanding the library of functional IOH-NPs with additional stimuli-responsive components. For the composite materials presented herein, optimization of the NP loading, material thickness, and the investigation of the long-term stability are of particular importance.

In addition, for the completion of the UV light sensor, additional controlled radiation experiments with UV and visible light are required. The next steps for the fabrication of a locally degradable 3D printed polymers using light-to-heat conversion of ICG and IR-820-based IOH-NPs require further synthetic work, which includes the preparation of an oligomer precursor containing dynamic bonds that cleave at temperatures of approximately 80 °C. Currently, a DA adduct containing oligomer is being developed. Furthermore, the IR-820-based IOH-NPs represents a novel compound, which is promising to test for photothermal treatment of tumors and photoacoustic imaging.

A possible future direction is the design and fabrication of composite materials for orthogonal multi-analyte detection. For instance, a composite material, responsive to both temperature and pH could undergo a temperature-sensitive color change alongside a pH-dependent fluorescence emission shift. To achieve this, the identification and development of additional responsive composite materials is required. Finally, integrating the prepared composite materials into devices, such as wearable sensors or food/pharmaceutical packaging, represents an exciting avenue for future research.

Despite the advances presented in the present thesis for the photothermal laser printing of sub-µm metal-oxide structures, several challenges for the fabrication of conductive metal wires remain. Looking forward, models for understanding the formation of the steep temperature gradient are required to assist with selecting suitable ink components. For the current fabrication of single-crystalline ZnO, gaining comprehension of the crystal formation on a rapid timescale and the investigation of the interactions between the substrate and printed material are exciting. Moreover, achieving morphological control of the printed material (e.g., the addition of dyes into the ink) is a fascinating avenue to adjust the electrical and optical properties. Currently, the photothermal laser printing of inorganic materials is restricted mainly to ZnO, and thus exploring other metal-precursor-solvent systems applicable to a wide variety of metals and metal oxides is required. For example, promising metal precursors are metal acetylacetonates, which are available for a wide variety of transition metals. In addition, orthogonality can be achieved by using the same metal precursors while simply exchanging the metal. Finally, a major opportunity lies in the fabrication of fully photothermal printed microelectronic and piezoelectric devices. The fabrication of such devices by step-by-step printing of metals and metal oxides, such as the sub-µm single-crystalline ZnO, is highly desirable. In addition, *p*-type semiconductors, such as

NiO, and insulators, for instance TiO_2 and Al_2O_3, need to be identified and photothermally printed to fabricate electronic devices, such as transistors.

CHAPTER 14: REFERENCES

[1] L. Zhou, J. Miller, J. Vezza, M. Mayster, M. Raffay, Q. Justice, Z. Al Tamimi, G. Hansotte, L. D. Sunkara, J. Bernat, *Sensors* **2024**, *24*, 2668.

[2] T. D. Ngo, A. Kashani, G. Imbalzano, K. T. Q. Nguyen, D. Hui, *Compos. Part B Eng.* **2018**, *143*, 172–196.

[3] S. Tabrizi, Y. Y. Cao, H. Lin, B. H. Jia, *Sci. China Phys. Mech. Astron.* **2017**, *60*, 1–17.

[4] N. Armon, E. Greenberg, E. Edri, O. Nagler-Avramovitz, Y. Elias, H. Shpaisman, *Adv. Funct. Mater.* **2021**, *31*, 2008547.

[5] X. Wu, K. Ehrmann, C. T. Gan, B. Leuschel, F. Pashley-Johnson, C. Barner-Kowollik, *Adv. Mater.* **2025**, *37*, 2419639.

[6] A. Al Rashid, W. Ahmed, M. Y. Khalid, M. Koç, *Addit. Manuf.* **2021**, *47*, 102279.

[7] I. Cazin, M. O. Gleirscher, M. Fleisch, M. Berer, M. Sangermano, S. Schlögl, *Addit. Manuf.* **2022**, *57*, 102977.

[8] S. Zhan, A. X. Y. Guo, S. C. Cao, N. Liu, *Int. J. Mol. Sci.* **2022**, *23*, 3790.

[9] M. Pagac, J. Hajnys, Q.-P. Ma, L. Jancar, J. Jansa, P. Stefek, J. Mesicek, *Polymers (Basel).* **2021**, *13*, 0598.

[10] M. Maturi, E. Locatelli, A. S. De Leon, M. C. Franchini, S. I. Molina, *Adv. Mater.* **2025**, *37*, 8710–8754.

[11] S. H. Kang, *MRS Bull.* **2024**, *49*, 1121–1126.

[12] A. J. Boydston, B. Cao, A. Nelson, R. J. Ono, A. Saha, J. J. Schwartz, C. J. Thrasher, *J. Mater. Chem. A* **2018**, *6*, 20621–20645.

[13] A. Walther, *Adv. Mater.* **2020**, *32*, 1905111.

[14] N. Arora, S. Dua, V. K. Singh, S. K. Singh, T. Senthilkumar, *Mater. Today*

Commun. **2024**, *40*, 109617.

[15] H. Goesmann, C. Feldmann, *Angew. Chem. Int. Ed.* **2010**, *49*, 1362–1395.

[16] M. Steurer, X. Wu, A. C. Morrissey, K. Faershteyn, M. Fladung, P. Somers, F. Feist, M. Bastmeyer, M. Wegener, C. Feldmann, C. Barner-Kowollik, *Mater. Horiz.* **2025**, *12*, 9139.

[17] B. L. Neumeier, M. Khorenko, F. Alves, O. Goldmann, J. Napp, U. Schepers, H. M. Reichardt, C. Feldmann, *ChemNanoMat* **2019**, *5*, 24–45.

[18] M. Poß, R. J. Tower, J. Napp, L. C. Appold, T. Lammers, F. Alves, C. C. Glüer, S. Boretius, C. Feldmann, *Chem. Mater.* **2017**, *29*, 3547–3554.

[19] K. Sabljo, J. Napp, F. Alves, C. Feldmann, *Chem. Commun.* **2022**, *58*, 9417–9420.

[20] M. Shamsipur, A. Barati, Z. Nematifar, *J. Photochem. Photobiol. C Photochem. Rev.* **2019**, *39*, 76–141.

[21] A. P. Demchenko, *Methods Appl. Fluoresc.* **2020**, *8*, 22001.

[22] J. Maillard, K. Klehs, C. Rumble, E. Vauthey, M. Heilemann, A. Fürstenberg, *Chem. Sci.* **2021**, *12*, 1352–1362.

[23] M. Steurer, P. Somers, K. Kraft, L. Grünewald, S. Kraus, F. Feist, B. Weinert, E. Müller, S. Dehnen, C. Feldmann, Y. M. Eggeler, C. Barner-Kowollik, M. Wegener, *Adv. Sci.* **2024**, *11*, 2410771.

[24] L. D. Zarzar, B. S. Swartzentruber, B. F. Donovan, P. E. Hopkins, B. Kaehr, *ACS Appl. Mater. Interfaces* **2016**, *8*, 21134–21139.

[25] L. Yang, H. Hu, A. Scholz, F. Feist, G. Cadilha Marques, S. Kraus, N. M. Bojanowski, E. Blasco, C. Barner-Kowollik, J. Aghassi-Hagmann, M. Wegener, *Nat. Commun.* **2023**, *14*, 1–10.

[26] Z. Ma, Y. Zhang, B. Han, Q. Chen, H. Sun, *Small Methods* **2018**, *2*, 1700413.

[27] J. C. Scaiano, *Chem. Soc. Rev.* **2023**, *52*, 6330–6343.

[28] J. Scaiano, *ACS Focus* **2022**, *12*, 12–13.

[29] A. Goulet-Hanssens, F. Eisenreich, S. Hecht, *Adv. Mater.* **2020**, *32*, 1905966.

[30] M. J. Hansen, W. A. Velema, M. M. Lerch, W. Szymanski, B. L. Feringa, *Chem. Soc. Rev.* **2015**, *44*, 3358–3377.

[31] J. W. Draper, *London, Edinburgh, Dublin Philos. Mag. J. Sci.* **1841**, *19*, 195–210.

[32] M. Kasha, *Acta Phys. Pol. A* **1987**, *71*, 661–670.

[33] H. H. Jaffé, A. L. Miller, *J. Chem. Educ.* **1966**, *43*, 469–473.

[34] J. R. Lakowicz, *Principles of Fluorescence Spectroscopy*, Springer, New York, **2006**.

[35] R. Š. and M. Amaro, *Fluorescence Spectroscopy and Microscopy*, **2014**.

[36] J. Z. Manapat, Q. Chen, P. Ye, R. C. Advincula, *Macromol. Mater. Eng.* **2017**, *302*, 1–13.

[37] R. Chaudhary, P. Fabbri, E. Leoni, F. Mazzanti, R. Akbari, C. Antonini, *Prog. Addit. Manuf.* **2023**, *8*, 331–351.

[38] S. O'Halloran, A. Pandit, A. Heise, A. Kellett, *Adv. Sci.* **2023**, *10*, 1–18.

[39] A. Bagheri, J. Jin, *ACS Appl. Polym. Mater.* **2019**, *1*, 593–611.

[40] J. Lalevée, S. Telitel, P. Xiao, M. Lepeltier, F. Dumur, F. Morlet-Savary, D. Gigmes, J. P. Fouassier, *Beilstein J. Org. Chem.* **2014**, *10*, 863–876.

[41] K. Gziut, A. Kowalczyk, B. Schmidt, *Polymers (Basel).* **2020**, *12*, 1–16.

[42] M. R. Azani, A. Hassanpour, *J. Compos. Sci.* **2024**, *8*, 441.

[43] J.-J. Tzeng, T.-S. Yang, W.-F. Lee, H. Chen, H.-M. Chang, *Polymers (Basel).* **2021**, *13*, 822.

[44] Y. Yagci, S. Jockusch, N. Turro, *Macromolecules* **2010**, *43*, 6245–6260.

[45] L. U. Kim, J. W. Kim, C. K. Kim, *Biomacromolecules* **2006**, *7*, 2680–2687.

[46] S. C. Ligon, R. Liska, J. Stampfl, M. Gurr, R. Mülhaupt, *Chem. Rev.* **2017**, *117*, 10212–10290.

[47] P. Somers, A. Münchinger, S. Maruo, C. Moser, X. Xu, M. Wegener, *Nat. Rev. Phys.* **2024**, *6*, 99–113.

[48] T. Wholers, T. Gornet, N. Mostow, *Wholers Rep.* **2016**, 1–38.

[49] A. Bhargav, V. Sanjairaj, V. Rosa, L. W. Feng, J. Fuh YH, *J. Biomed. Mater. Res. - Part B Appl. Biomater.* **2018**, *106*, 2058–2064.

[50] T. Zhao, R. Yu, S. Li, X. Li, Y. Zhang, X. Yang, X. Zhao, C. Wang, Z. Liu, R. Dou, W. Huang, *ACS Appl. Mater. Interfaces* **2019**, *11*, 14391–14398.

[51] X. Zhou, K. Parida, O. Halevi, S. Magdassi, P. S. Lee, *Sensors* **2020**, *20*, 1–9.

[52] G. Zhu, Y. Hou, J. Xiang, J. Xu, N. Zhao, *ACS Appl. Mater. Interfaces* **2021**, *13*, 34954–34961.

[53] F. Alam, M. Elsherif, A. E. Salih, H. Butt, *Addit. Manuf.* **2022**, *58*, 102996.

[54] A. Oesterreicher, J. Wiener, M. Roth, A. Moser, R. Gmeiner, M. Edler, G. Pinter, T. Griesser, *Polym. Chem.* **2016**, *7*, 5169–5180.

[55] H. Ding, M. Dong, Q. Zheng, Z. L. Wu, *Mol. Syst. Des. Eng.* **2022**, *7*, 1017–1029.

[56] R. Felzmann, S. Gruber, G. Mitteramskogler, P. Tesavibul, A. R. Boccaccini, R. Liska, J. Stampfl, *Adv. Eng. Mater.* **2012**, *14*, 1052–1058.

[57] L. Messe, C.; Chapelat, *Curable Composition*, **2013**.

[58] *C. W. Hull, Appar. Prod. three-dimensional objects by stereolithography, U.S. Pat. 4 575 330, 1986.* **n.d.**

[59] X. Wang, M. Jiang, Z. Zhou, J. Gou, D. Hui, *Compos. Part B Eng.* **2017**, *110*, 442–458.

[60] Z.-X. Low, Y. T. Chua, B. M. Ray, D. Mattia, I. S. Metcalfe, D. A. Patterson, *J. Memb. Sci.* **2017**, *523*, 596–613.

[61] S. C. Gauci, A. Vranic, E. Blasco, S. Bräse, M. Wegener, C. Barner-Kowollik, *Adv. Mater.* **2024**, *36*, 2306468.

[62] N. B. Palaganas, J. D. Mangadlao, A. C. C. de Leon, J. O. Palaganas, K. D.

Pangilinan, Y. J. Lee, R. C. Advincula, *ACS Appl. Mater. Interfaces* **2017**, *9*, 34314–34324.

[63] J. Warner, P. Soman, W. Zhu, M. Tom, S. Chen, *ACS Biomater. Sci. Eng.* **2016**, *2*, 1763–1770.

[64] R. Janusziewicz, J. R. Tumbleston, A. L. Quintanilla, S. J. Mecham, J. M. DeSimone, *Proc. Natl. Acad. Sci.* **2016**, *113*, 11703–11708.

[65] J. R. Tumbleston, D. Shirvanyants, N. Ermoshkin, R. Janusziewicz, A. R. Johnson, D. Kelly, K. Chen, R. Pinschmidt, J. P. Rolland, A. Ermoshkin, E. T. Samulski, J. M. DeSimone, *Science (80-.).* **2015**, *347*, 1349–1352.

[66] Z. Ji, C. Yan, B. Yu, X. Zhang, M. Cai, X. Jia, X. Wang, F. Zhou, *Adv. Mater. Technol.* **2019**, *4*, 1800713.

[67] J. V Crivello, **1996**, *34*, 3231–3253.

[68] X. Allonas, E. Goldbach, X. Allonas, **2025**, *16*, 126.

[69] M. S. Malik, S. Schlögl, M. Wolfahrt, M. Sangermano, *Polymers (Basel).* **2020**, *12*, 2146.

[70] D. G. Sycks, T. Wu, H. S. Park, K. Gall, *J. APPL. POLYM. SCI.* **2018**, *135*, 46259.

[71] C. E. Hoyle, T. A. I. Y. Lee, T. Roper, **2004**, *42*, 5301–5338.

[72] D. Procedures, S. De Flor, *Materials (Basel).* **2021**, *14*, 107.

[73] S. R. Trenor, T. E. Long, B. J. Love, **2004**, *205*, 715–723.

[74] N. Jarach, H. Dodiuk, S. Kenig, S. Magdassi, *Adv. Mater.* **2024**, *36*, 2307297.

[75] S. C. Gauci, M. Gernhardt, H. Frisch, H. A. Houck, J. P. Blinco, E. Blasco, B. T. Tuten, C. Barner-Kowollik, *Adv. Funct. Mater.* **2023**, *33*, 1–7.

[76] M. Dzwonkowska-Zarzycka, A. Sionkowska, *Molecules* **2024**, *29*, 3898.

[77] B. Jiang, H. Jiao, X. Guo, G. Chen, J. Guo, W. Wu, Y. Jin, **2023**, *10*, 2206055.

[78] C. Vazquez-Martel, P. Mainik, E. Blasco, *Org. Mater.* **2022**, *4*, 281–291.

[79] F. Petko, M. Jankowska, M. Galek, M. Noworyta, R. Popielarz, J. Ortyl,

Macromolecules **2024**, *57*, 11639−11657.

[80] F. Petko, A. Świeży, M. Jankowska, P. Stalmach, J. Ortyl, *Polym. Chem.* **2023**, *14*, 3018.

[81] L. Zhao, R. Yu, Y. He, M. Zhang, F. Tian, L. Wang, *Addit. Manuf.* **2024**, *79*, 103904.

[82] S. Gaca, K. Dietliker, E. Rossegger, S. Schl, *React. Funct. Polym.* **2024**, *205*, 106085.

[83] J. J. Schwartz, A. J. Boydston, *Nat. Commun.* **2019**, *10*, 791.

[84] T. Kaneko, J. Kim, J. M. Kronenfeld, K. S. Mason, *RSCAppl. Polym.* **2025**, *3*, 574–591.

[85] S. J. Bailey, E. Hopkins, N. J. Baxter, I. Whitehead, J. R. de Alaniz, M. Z. Wilson, *Adv. Mater.* **2023**, *35*, 2303453.

[86] J. A. Tomko, D. H. Olson, J. L. Braun, P. Kelliher, B. Kaehr, P. E. Hopkins, *Appl. Phys. Lett.* **2018**, *112*, 1–6.

[87] X. Zhou, W. Guo, Y. Zhu, P. Peng, *Nanoscale* **2020**, *12*, 563–571.

[88] C. Kindle, A. Castonguay, S. McGee, J. A. Tomko, P. E. Hopkins, L. D. Zarzar, *ACS Appl. Nano Mater.* **2019**, *2*, 2581–2586.

[89] D. Savytskii, H. Jain, N. Tamura, V. Dierolf, *Sci. Rep.* **2016**, *6*, 36449.

[90] H. J. D.Savytskii, C. Au-Yeung, V. Dierolf, N. Tamura, *Cryst. Growth Des.* **2017**, *17*, 1735−1746.

[91] L. D. Zarzar, B. S. Swartzentruber, B. F. Donovan, P. E. Hopkins, B. Kaehr, *ACS Appl. Mater. Interfaces* **2016**, *8*, 21134–21139.

[92] W. Lu, Y. Zhang, M. Zheng, Y. Jia, J. Liu, Z. Zhao, C. Li, Y. Xia, T. Ye, *Opt. Mater. Express* **2013**, *3*, 543–546.

[93] Y. H. Lee, I. Y. Phang, X. Y. Ling, *ACS Appl. Mater. Interfaces* **2017**, *9*, 39584–39593.

[94] L. D. Zarzar, B. S. Swartzentruber, J. C. Harper, D. R. Dunphy, C. J. Brinker, J. Aizenberg, B. Kaehr, *J. Am. Chem. Soc.* **2012**, *134*, 4007–4010.

[95] Y. Cao, N. Takeyasu, T. Tanaka, X. Duan, S. Kawata, *small* **2009**, *5*, 1144–1148.

[96] Y. Cao, M. Gu, *Appl. Phys. Lett.* **2013**, *103*, 213104.

[97] S. Kang, K. Vora, E. Mazur, *Nanotechnology* **2015**, *26*, 121001.

[98] A. Ishikawa, T. Tanaka, S. Kawata, *Appl. Phys. Lett.* **2006**, *89*, 113102.

[99] B. G. Streetman, • Sanjay, K. Banerjee, *Solid State Electronic Devices*, Global Edition, Pearson, **2015**.

[100] S. Tibbits, in *TED Conf.*, **2013**.

[101] F. Momeni, S. M.Mehdi Hassani.N, X. Liu, J. Ni, *Mater. Des.* **2017**, *122*, 42–79.

[102] C. A. Spiegel, M. Hippler, A. Münchinger, M. Bastmeyer, C. Barner-Kowollik, M. Wegener, E. Blasco, *Adv. Funct. Mater.* **2020**, *30*, 1907615.

[103] F. K. Aldawood, *Actuators* **2023**, *12*, 101.

[104] C. Barner-Kowollik, M. Bastmeyer, E. Blasco, G. Delaittre, P. Müller, B. Richter, M. Wegener, *Angew. Chem. Int. Ed.* **2017**, *56*, 15828–15845.

[105] E. Blasco, J. Müller, P. Müller, V. Trouillet, M. Schön, T. Scherer, C. Barner-Kowollik, M. Wegener, *Adv. Mater.* **2016**, *28*, 3592–3595.

[106] L. C. du Toit, Y. E. Choonara, P. Kumar, V. Pillay, in *Adv. 3D-Printed Syst. Nanosyst. Drug Deliv. Tissue Eng.* (Eds.: L.C. du Toit, P. Kumar, Y.E. Choonara, V. Pillay), Elsevier, **2020**, pp. 139–157.

[107] R. Singh, *4D Imaging to 4D Printing Biomedical Applications*, CRC Press, **2022**.

[108] L. Wu, J. Huang, M. Zhai, B. Sun, H. Chang, S. Huang, H. Liu, *Electronics* **2021**, *10*, 1–9.

[109] S. W. Ula, N. A. Traugutt, R. H. Volpe, R. R. Patel, K. Yu, C. M. Yakacki, *Liq. Cryst. Rev.* **2018**, *6*, 78–107.

[110] Z. Ji, C. Yan, B. Yu, X. Wang, F. Zhou, *Adv. Mater. Interfaces* **2017**, *4*, 1–6.

[111] A. Bhandari, R. N. Ghosh, M. Namboothiri, Pramod K. Peter, *Mater. Adv.* **2025**, Advance Article.

[112] M. Gernhardt, V. X. Truong, C. Barner-Kowollik, *Adv. Mater.* **2022**, *34*, 2203474.

[113] R. Batchelor, T. Messer, M. Hippler, M. Wegener, C. Barner-Kowollik, E. Blasco, *Adv. Mater.* **2019**, *31*, 1904085.

[114] I. Kammakakam, *Mater. Adv.* **2021**, *2*, 1821.

[115] M. Trofa, G. D. Avino, B. Fabiano, M. Vocciante, *Materials (Basel).* **2020**, *13*, 4281.

[116] M. Y. Dabney, C. P. Loranz, *South. Med. J.* **1922**, *15*, 242.

[117] Y. Liu, K. Kathan, W. Saad, R. K. Prud, *Phys. Rev. Lett.* **2007**, *98*, 036102.

[118] J. G. Heck, J. Napp, S. Simonato, J. Möllmer, M. Lange, H. M. Reichardt, R. Staudt, F. Alves, C. Feldmann, *J. Am. Chem. Soc.* **2015**, *137*, 7329–7336.

[119] B. L. Neumeier, J. G. Heck, C. Feldmann, *J. Mater. Chem. C* **2019**, *7*, 3543–3552.

[120] C. Cremer, U. Birk, *Front. Phys.* **2016**, *4*, 1–9.

[121] E. Abbe, *Arch. für Mikroskopische Anat.* **1873**, *9*, 413–468.

[122] V. V. Nemoshkalenko, V. G. Aleshin, V. V. Nemoshkalenko, V. G. Aleshin, *Physical Principles of Electron Spectroscopy*, Springer, **2016**.

[123] G. H. Michler, *Kompakte Einführung in Die Elektronen- Mikroskopie*, Springer Spektrum, **2019**.

[124] J. I. Goldstein, D. E. Newbury, J. R. Michael, N. W. M. Ritchie, J. H. J. Scott, D. C. Joy, *Scanning Electron Microscopy and X-Ray Microanalysis*, Springer New York, **2018**.

[125] J. Ackermann, in *Handb. Für Die Rasterelektronenmikroskopie SUPRA(VP) Und ULTRA*, Carl Zeiss SMT Ltd, Oberkochen, **2004**.

[126] P. F. Schmidt, *Praxis Der Rasterelektronenmikroskopie Und*

Mikrobereichsanalyse, Fachverlag Für Wirtschaft Und Technik, Renningen, **2011**.

[127] B. J. Berne, R. Pecora, *Dynamic Light Scattering: With Applications to Chemistry, Biology, and Physics*, Courier Corporation, **2000**.

[128] M. I. Ltd., *Zetasizer Nano User Manual,* Malvern Instruments Ltd., Malvern, **2007**.

[129] H.-D. Dörfler, *Grenzflächen Und Kolloid-Disperse Systeme*, Springer, Berlin, **2002**.

[130] J. Jonkman, C. M. Brown, G. D. Wright, K. I. Anderson, A. J. North, *Nat. Protoc.* **2020**, *15*, 1585–1611.

[131] C. M. St Croix, S. H. Shand, S. C. Watkins, *Biotechniques* **2005**, *39*, 2–5.

[132] W. G. Jerome, R. L. Price, *Fluorescence Microscopy*, **2018**.

[133] J.-A. Conchello, J. W. Lichtman, *Nat. Methods* **2005**, *2*, 920–931.

[134] H.-H. Perkampus, *UV-VIS Spectroscopy and Its Applications*, Springer Science, **2013**.

[135] H. Günzler, H.-U. Gremlich, *IR-Spektroskopie: Eine Einführung*, John Wiley & Sons, Ltd, **2012**.

[136] L. J. Poppe, V. F. Paskevich, J. C. Hathaway, D. S. Blackwood, *US Geol. Surv. Open-File Rep.* **2001**, *1.041*, 1–88.

[137] H. Li, G. Go, S. Y. Ko, J. O. Park, S. Park, *Smart Mater. Struct.* **2016**, *25*, 027001.

[138] M. E. Villanueva, M. L. Cuestas, C. J. Pérez, V. Campo Dall′ Orto, G. J. Copello, *J. Colloid Interface Sci.* **2019**, *536*, 372–380.

[139] L. Larush, I. Kaner, A. Fluksman, A. Tamsut, A. A. Pawar, P. Lesnovski, O. Benny, S. Magdassi, *J. 3D Print. Med.* **2017**, *1*, 219–229.

[140] C. Chen, M. Zhang, A. S. Mujumdar, P. Phuhongsung, *Food Res. Int.* **2021**, *148*, 110630.

[141] S. Shanthamma, R. Preethi, J. A. Moses, C. Anandharamakrishnan, *ACS Food Sci. Technol.* **2021**, *1*, 669–679.

[142] M. Nadgorny, Z. Xiao, C. Chen, L. A. Connal, *ACS Appl. Mater. Interfaces* **2016**, *8*, 28946–28954.

[143] X. L. Gong, Y. Y. Xiao, M. Pan, Y. Kang, B. J. Li, S. Zhang, *ACS Appl. Mater. Interfaces* **2016**, *8*, 27432–27437.

[144] Y. Hu, Z. Wang, D. Jin, C. Zhang, R. Sun, Z. Li, K. Hu, J. Ni, Z. Cai, D. Pan, X. Wang, W. Zhu, J. Li, D. Wu, L. Zhang, J. Chu, *Adv. Funct. Mater.* **2020**, *30*, 1907377.

[145] K. Sabljo, Anorganisch-Organische Hybridnanopartikel Mit Theranostischen Eigenschaften, Cuvillier Verlag, **2022**.

[146] L. D. Zarzar, P. Kim, M. Kolle, C. J. Brinker, J. Aizenberg, B. Kaehr, *Angew. Chem. Int. Ed.* **2011**, *50*, 9356–9360.

[147] X. Li, W. Z. Zheng, P. Y. Xu, Z. Y. Zhang, B. Lu, D. Huang, Z. C. Zhen, J. H. Ji, G. X. Wang, *Sci. Total Environ.* **2024**, *951*, 175729.

[148] J. Singh, P. Nayak, *J. Polym. Sci.* **2023**, *61*, 2828–2850.

[149] Q. Wang, Y. Y. Zhang, X. Y. Dai, X. H. Shi, W. G. Liu, *Sci. China Technol. Sci.* **2017**, *60*, 78–83.

[150] I. Cooperstein, E. Sachyani-Keneth, E. Shukrun-Farrell, T. Rosental, X. Wang, A. Kamyshny, S. Magdassi, *Adv. Mater. Interfaces* **2018**, *5*, 1800996.

[151] P. Ezati, H. Tajik, M. Moradi, R. Molaei, *Int. J. Biol. Macromol.* **2019**, *132*, 157–165.

[152] M. Lievremont, J. Potus, B. Guillou, *Acta Anat. (Basel).* **1982**, *114*, 268–280.

[153] R. Ohgaki, Y. Teramura, D. Hayashi, L. Quan, S. Okuda, S. Nagamori, M. Takai, Y. Kanai, *Sci. Rep.* **2017**, *7*, 17484.

[154] M. M. El-Nahass, H. M. Zeyada, N. A. El-Ghamaz, A. S. Awed, *Optik* **2018**, *170*,

304–313.

[155] N. A. Manshor, Q. Wali, K. Wong, K. Muzakir, *Phys.Chem.Chem.Phys.* **2016**, *18*, 21629–21639.

[156] E. Yousif, G. A. El-hiti, R. Haddad, A. A. Balakit, *Polymers (Basel).* **2015**, *7*, 1005–1019.

[157] W. F. Schroeder, S. L. Asmussen, W. D. Cook, C. I. Vallo, *Polym. Int.* **2011**, *60*, 1362–1369.

[158] P. Höschele, S. F. Heindl, B. Schneider, W. Sinz, C. Ellersdorfer, *Batteries* **2022**, *8*, 35.

[159] H. Zhang, H. Liu, L. F. J. Piper, M. S. Whittingham, G. Zhou, *Chem. Rev.* **2022**, *122*, 5641–5681.

[160] X. Yao, Q. Dong, Q. Cheng, D. Wang, *Angew. Chem. Int. Ed.* **2016**, *55*, 11344–11353.

[161] H. Shimizu, T. Naganuma, A. Kanai, N. Umemura, *Jpn. J. Appl. Phys.* **1993**, *32*, 758–759.

[162] J. H. Harris, R. A. Youngman, R. G. Teller, *J. Mater. Res.* **1990**, *5*, 1763–1773.

[163] J. Li, X. Ran, M. Zhou, K. Wang, H. Wang, Y. Wang, *Sci. Total Environ.* **2022**, *838*, 156454.

[164] M. Khademian, J. A. Imlay, *Mol. Microbiol.* **2020**, *114*, 333–347.

[165] C. Mooiman, J. Bouwknegt, W. J. C. Dekker, S. J. Wiersma, R. A. Ortiz-Merino, E. De Hulster, J. T. Pronk, *FEMS Yeast Res.* **2021**, *21*, 1–13.

[166] R. Mahajan, A. Templeton, A. Harman, R. A. Reed, R. T. Chern, *Pharm. Res.* **2005**, *22*, 128–140.

[167] K. C. Waterman, R. C. Adami, K. M. Alsante, J. Hong, M. S. Landis, F. Lombardo, C. J. Roberts, *Pharm. Dev. Technol.* **2002**, *7*, 1–32.

[168] D. H. Won, H. Park, E. S. Ha, Y. M. Kim, H. D. Hwang, S. W. Jang, M. S. Kim,

Pharmaceutics **2020**, *12*, 46.

[169] J. T. Mouhovski, *Prog. Cryst. Growth Charact. Mater.* **2007**, *53*, 79–116.

[170] D. Ahn, L. M. Stevens, K. Zhou, Z. A. Page, *Adv. Mater* **2021**, *33*, 2104906.

[171] Y. Li, X. Zhang, X. Zhang, Y. Zhang, D. Hou, *Polymers* **2023**, *15*, 3940.

[172] D. B. Papkovsky, R. I. Dmitriev, *Chem. Soc. Rev.* **2013**, *42*, 8700–8732.

[173] M. Quaranta, S. M. Borisov, I. Klimant, *Bioanal. Rev.* **2012**, *4*, 115–157.

[174] D. B. Papkovsky, T. C. O'Riordan, *J. Fluoresc.* **2005**, *15*, 569–584.

[175] K. Leitonas, A. Tomkeviciene, G. Baratte, A. Dabuliene, S. M. Punniyakoti, D. Volyniuk, J. V. Grazulevicius, *Sens. Actuators B* **2021**, *345*, 130369.

[176] Y. Wu, G. D. Sutton, M. D. S. Halamicek, X. Xing, J. Bao, T. S. Teets, *Chem. Sci.* **2022**, *13*, 8804–8812.

[177] J. N. Demas, B. A. DeGraff, *J. Chem. Educ.* **1997**, *74*, 690-695.

[178] D. B. Papkovsky, G. V. Ponomarev, W. Trettnak, P. O'Leary, *Anal. Chem.* **1995**, *67*, 4112–4117.

[179] R. Paolesse, S. Nardis, D. Monti, M. Stefanelli, C. Di Natale, *Chem. Rev.* **2017**, *117*, 2517–2583.

[180] B. Zhang, H. Wu, S. Li, Y. Liu, P. Du, Z. Wang, *ACS Catal.* **2023**, *13*, 6763−6772.

[181] M. Spexard, D. Immeln, C. Thöing, T. Kottke, *Vib. Spectrosc.* **2011**, *57*, 282–287.

[182] P. Macheroux, *Flavoprotein Protocols*, Humana Press, Totowa, **1999**, *131,* 1–7.

[183] M. Roming, H. Lünsdorf, K. E. J. Dittmar, C. Feldmann, *Angew. Chem. Int. Ed.* **2010**, *49*, 632–637.

[184] E. Montes-Cobos, S. Ring, H. J. Fischer, J. Heck, J. Strauß, M. Schwaninger, S. D. Reichardt, C. Feldmann, F. Lühder, H. M. Reichardt, *J. Control. Release* **2017**, *245*, 157–169.

[185] R. M. Berne, *Biochem. J.* **1962**, *83*, 368–377.

[186] R. A. McBride, D. T. Barnard, K. Jacoby-Morris, M. Harun-Or-Rashid, R. J. Stanley, *Biochemistry* **2023**, *62*, 759–769.

[187] S. L. J. Tan, J. M. Kan, R. D. Webster, *J. Phys. Chem. B* **2013**, *117*, 13755–13766.

[188] M. A. Martini, O. Ru, N. Breuer, N. Birgit, S. Debeer, P. Rodr, J. A. Birrell, *J. Am. Chem. Soc.* **2021**, *143*, 18159−18171.

[189] W. Ł. Grześkowiak, I. Ratajczak, M. Zborowska, M. Przybylska, M. Patora, *Materials* **2024**, *17*, 5283.

[190] A. Cayla, F. Rault, S. Giraud, F. Salaün, R. Sonnier, L. Dumazert, *Materials* **2019**, *12*, 1146.

[191] Y. H. Wu, H. B. Park, T. Kai, B. D. Freeman, D. S. Kalika, *J. Memb. Sci.* **2010**, *347*, 197–208.

[192] C. Warr, J. C. Valdoz, B. P. Bickham, C. J. Knight, N. A. Franks, N. Chartrand, P. M. Van Ry, K. A. Christensen, G. P. Nordin, A. D. Cook, *ACS Appl. Bio Mater.* **2020**, *3*, 2239–2244.

[193] N. De Alwis Watuthanthrige, M. L. Allegrezza, M. T. Dolan, A. J. Kloster, M. Kovaliov, S. Averick, D. Konkolewicz, *Angew. Chem. Int. Ed.* **2019**, *58*, 11826–11829.

[194] R. Miura, *Chem. Rec.* **2001**, *1*, 183–194.

[195] M. Bose, J. Hagerty, J. Boes, C. Kim, S. Member, W. V Stoecker, P. Nam, *IEEE Sens. J.* **2021**, *21*, 21494–21502.

[196] D. Yusufu, R. Han, A. Mills, *Analyst* **2020**, *145*, 4124–4129.

[197] A. M. Brouwer, **2011**, *83*, 2213–2228.

[198] M. J. Talite, H. Huang, Z. Chen, W. Li, K. Cai, R. C. Sevilla, R. J. Soebroto, S. Lin, W. Chou, C. Yuan, *Sol. RRL* **2022**, *6*, 2100955.

[199] C. Gu, J. L. Zhang, S. Sun, X. Lian, Z. Ma, H. Mao, L. Guo, Y. Wang, W. Chen,

ACS Appl. Mater. Interfaces 2020, **2020**, *12*, 22327−22334.

[200] Y. Kang, S. H. Jeon, Y. Cho, S. Han, *Phys. Rev. B* **2016**, *93*, 035131.

[201] I. G. Hill, A. Kahn, *Chem. Phys. Lett. 327* **2000**, *327*, 181–188.

[202] S. R. Forrest, *J. Phys. Condens. Matter* **2003**, *15*, S2599–S2610.

[203] Y. Han, W. Ning, H. Du, J. Yang, N. Wang, L. Cao, F. Li, F. Zhang, F. Xu, M. Tian, *Nanoscale* **2015**, *7*, 17116–17121.

[204] C. Ritschel, L. J. Daumann, C. Feldmann, *Dalt. Trans.* **2025**, *54*, 1348–1353.

[205] S. Anand, A. Kumar, K. Rajendra, P. Sunajadevi, *Appl. Organomet. Chem.* **2025**, *39*, e70084.

[206] C. Ritschel, J. Napp, F. Alves, C. Feldmann, *Nanoscale* **2022**, *14*, 16249–16255.

[207] W. M. Haynes, Ed. , *CRC Handbook of Chemistry and Physics*, CRC Press (Taylor & Francis Group), Boca Raton, **2012**.

[208] C. J. Murphy, L. B. Thompson, D. J. Chernak, J. A. Yang, S. T. Sivapalan, S. P. Boulos, J. Huang, A. M. Alkilany, P. N. Sisco, *Curr. Opin. Colloid Interface Sci.* **2011**, *16*, 128–134.

[209] W. Lorenz, E. Neugebauer, A. Schmal, *Ann. Fr. Anesth. Reanim.* **1982**, *1*, 271–276.

[210] Y. Makabe-Kobayashi, Y. Hori, T. Adachi, S. Ishigaki-Suzuki, Y. Kikuchi, Y. Kagaya, K. Shirato, A. Nagy, A. Ujike, T. Takai, T. Watanabe, H. Ohtsu, *J. Allergy Clin. Immunol.* **2002**, *110*, 298–303.

[211] Z. Shahrbabaki, F. Oveissi, S. Farajikhah, M. B. Ghasemian, R. D. J. Vuuren, P. G. Jessop, J. Yun, F. Dehghani, S. Na, *ACS Omega* **2022**, *7*, 22232–22243.

[212] P. J. Price, E. A. Gregory, *In Vitro Cell.Dev.Biol.-Plant* **1982,** *18,* 576–584*.*

[213] I. Roppolo, A. D. Bozzo, M. Castellino, A. Chiappone, D. Perrone, K. Bejtka, S. Bocchini, M. Sangermano, A. Chiolerio, *RSC Adv* **2016**, *6*, 14832–14843.

[214] A. Singh, W. Hou, T. Lin, R. G. Zepp, *Environ. Sci. Technol.* **2019**, *53*,

11162−11169.

[215] T. Al-Sadek, N. Yusuf, *Curr. Issues Mol. Biol.* **2024**, *46*, 1924–1942.

[216] D. Suh, S. Hockett Sherlock, K. C. Dukes, E. N. Perencevich, A. R. Marra, *Antimicrob. Steward. Healthc. Epidemiol.* **2025**, *5*, e199.

[217] E. Yousif, R. Haddad, *Springerplus* **2013**, *2*, 398.

[218] M. Wei, X. He, N. Liu, H. Deng, *Cell Div.* **2024**, *19*, 1.

[219] Y. L. Vechtomova, T. A. Telegina, A. A. Buglak, *Biomedicines* **2021**, *9*, 1564.

[220] R. Bosch, N. Philips, J. A. Suárez-Pérez, A. Juarranz, A. Devmurari, J. Chalensouk-Khaosaat, S. González, *Antioxidants* **2015**, *4*, 248–268.

[221] M. Linetsky, C. T. Raghavan, K. Johar, X. Fan, V. M. Monnier, A. R. Vasavada, R. H. Nagaraj, *J. Biol. Chem.* **2014**, *289*, 17111–17123.

[222] E. R. MacFarlane, P. J. Donaldson, A. C. Grey, *Front. Ophthalmol.* **2024**, *4*, 1414483.

[223] J. Smoleń, P. Olesik, B. Nowacki, M. Godzierz, K. Kurtyka, P. Chaber, J. Czakiert, M. Kozioł, *Sci. Rep.* **2024**, *14*, 7446.

[224] N. Singh, P. Sinha, D. K. Sinha, S. Banerjee, *Polym. Chem.* **2025**, *16*, 4479–4523.

[225] J. Zhang, M. Lu, X. Cai, Q. Zhong, *ACS Appl. Mater. Interfaces 2025,* **2025**, *17*, 8445−8455.

[226] S. I. Sagor, A. Khecho, E. B. Joyee, *ACS Appl. Eng. Mater.* **2025**, *3*, 3751−3763.

[227] V. Pruthi, Y. Chen, J. Chen, P. Th, *ACS Appl. Polym. Mater. 2025,* **2025**, *7*, 15809−15820.

[228] S. Yamashita, H. Fukushima, Y. Niidome, T. Mori, Y. Katayama, *Langmuir* **2011**, *27*, 14621–14626.

[229] J. Mackay, L. R. Hart, A. Z. Tareq, S. Wang, V. G. Abrego, I. Maskery, D. Irvine, D. Wildman, W. Hayes, *Mater. Adv.* **2025**, *6*, 6174–6182.

[230] X. Li, R. Yu, Y. He, Y. Zhang, X. Yang, X. Zhao, W. Huang, *Polymer* **2020**, *200*, 122532.

[231] M. Gastaldi, C. A. Spiegel, C. Vazquez-martel, C. Barolo, E. Blasco, *Mol. Syst. Des. Eng.* **2023**, *8*, 323–329.

[232] A. L. Widstrom, B. J. Lear, *Appl. Nanosci.* **2020**, *10*, 819–825.

[233] V. Froidevaux, M. Borne, E. Laborbe, R. Auvergne, A. Gandini, B. Boutevin, *RSC Adv.* **2015**, *5*, 37742–37754.

[234] C. Sottani, P. Saccomandi, L. Bianchi, M. Sevieri, R. Allevi, E. Grignani, S. Mazzucchelli, F. Corsi, *Int. J. Nanomedicine* **2024**, *19*, 4263–4278.

[235] A. M. Smith, M. C. Mancini, S. Nie, *Nat. Nanotechnol.* **2009**, *4*, 710–711.

[236] Z. Feng, X. Yu, M. Jiang, L. Zhu, Y. Zhang, W. Yang, W. Xi, G. Li, *Theranostics* **2019**, *9*, 5706–5719.

[237] J. Yeo, S. Hong, G. Kim, H. Lee, Y. D. Suh, I. Park, C. P. Grigoropoulos, S. H. Ko, M. Engineering, U. States, A. Nano, M. Engineering, M. Engineering, J. Yeo, S. Hong, *ACS Nano* **2015**, *9*, 6059–6068.

[238] R. M. Pasquarelli, C. J. Curtis, A. Miedaner, M. F. A. M. van Hest, R. P. O'Hayre, D. S. Ginley, *Inorg. Chem.* **2010**, *49*, 5424–5431.

[239] J. Zhang, Y. Y. Liu, J. L. Zeng, F. Xu, L. X. Sun, W. S. You, Y. Sawada, *J. Therm. Anal. Calorim.* **2008**, *91*, 861–866.

[240] A. Gorski, A. D. Krasnicka, *J. Therm. Anal.* **1987**, *32*, 1345–1354.

[241] A. Górski, A. Kraśnicka, *J. Therm. Anal.* **1987**, *32*, 1243–1251.

[242] K. A. Buzdov, B. D. Antonov, *Russ. J. Inorg. Chem.* **2012**, *57*, 1599–1605.

[243] R. M. Pasquarelli, C. J. Curtis, A. Miedaner, M. F. A. M. Van Hest, R. P. OHayre, D. S. Ginley, *Inorg. Chem.* **2010**, *49*, 5424–5431.

[244] Z. L. Wang, J. Song, *Science* **2006**, *312*, 242–246.

[245] F. Yan, Y. Wang, J. Zhang, Z. Lin, J. Zheng, F. Huang, *ChemSusChem* **2014**, *7*,

101–104.

[246] P. H. Maag, F. Feist, H. Frisch, P. W. Roesky, C. Barner-Kowollik, *Macromol.,* **2022**, *55*, 9918–9924.